ABSTRACT

Title of Dissertation: AN ANALYTICAL AND EXPERIMENTAL INVESTIGATION OF FILAMENT FORMATION IN GLASS/EPOXY COMPOSITES.

Keith Leslie Rogers, Doctor of Philosophy, 2005

Dissertation Directed By: Professor, Michael Pecht, Department of Mechanical Engineering

The drive to increase circuit density with smaller PWB geometries and higher layer counts in multi-layer boards along with the increasing use of electronics in harsh environments for high reliability and safety critical applications (automotive, avionics, medical, military) have made short circuiting of PWBs due to growth of conductive filaments between biased conductors a major concern. In addition, the impending implementation of lead-free soldering processing, which may affect laminate stability and materials choices, can increase the potential for conductive filament formation (CFF) failures. To mitigate these catastrophic failures, it is necessary to understand the roles and synergistic effects of environmental conditions, material properties and manufacturing quality in accelerating or deterring CFF.

In this dissertation, four laminate types (including a halogen free) and three conductor spacings are tested at different voltages in accordance with IPC TM-650, allowing a ranking of these laminate types based on resistance to CFF. Demonstrated is the use

of an innovative technique, the superconducting quantum interference device (SQUID), to verify and locate the internal short circuits due to CFF. The SQUID which detects magnetic fields generated by the current paths, displays images of the current density enabling identification of the shorted locations. With this technique, a new variant of filament formation in glass/epoxy composites: vertical filament formation (VFF) was identified. The conductive filaments found at the failure sites were observed during cross-sectioning techniques, verifying that the failures were due to CFF. A test standard to identify and quantify hollow glass fibers, potential paths for filament formation in laminated PWBs, was created. It was observed that board types, which show the longest time to failure due to CFF in PTH-PTH configuration, might not offer the best protection for PTH-plane geometry. Based on insulation resistance measurements, it was seen that the IPC-TM-650 test specification of monitoring every 24 hours could allow intermittent failures to go undetected. It was demonstrated that PTH-PTH dielectric breakdown voltage values followed the same trend as the time to failure observed for the PTH-PTH CFF failure data, suggesting that dielectric breakdown voltage can be an indicator of CFF susceptibility, saving considerable time and cost.

AN ANALYTICAL AND EXPERIMENTAL INVESTIGATION OF FILAMENT FORMATION IN GLASS/EPOXY COMPOSITES

By

Keith Leslie Rogers

Dissertation submitted to the Faculty of the Graduate School of the University of Maryland, College Park, in partial fulfillment of the requirements for the degree of Doctor of Philosophy
2005

Advisory Committee:
Professor Michael Pecht, Chair
Professor David Barbe
Professor Donald Barker
Professor Patrick McCluskey
Professor Omar Rahami

© Copyright by
Keith Leslie Rogers
2004

ACKNOWLEDGEMENTS

I first want to give thanks and praise to the Almighty God for His blessings in my life, especially during my college years. I also want to doubly thank my parents for exemplifying what perfect role models should be, and for their unwavering support and encouragement.

I want to thank my dear wife - Dilcia Rogers and my two wonderful sons - Keith Rogers Jr. and Kurtis Rogers for allowing me to take time away from them to complete this dissertation.

I would like to thank my advisor Professor Michael Pecht for his assistance, guidance and constructive criticism during my graduate studies. I am also indebted to him for opening many doors that would have other wise been barred to me. My acknowledgements to the other members of my advisory committee, Professors Patrick McCluskey, Omar Rahami, David Barbe and Donald Barker. I especially thank Dr. Craig Hillman for his assistance with the overall project.

Lastly, I want to thanks all the wonderful people at CALCE for their help, support, and for making our laboratories enjoyable places to work.

TABLE OF CONTENTS

Acknowledgements ii
Table of Contents iii
List of Figures v
Chapter 1: Introduction 1
1.1 Electrically Induced Failures in Printed Wiring Boards 1
1.2 Electrochemical Migration 2
1.3 Motivation 6
Chapter 2: Background 8
2.1 Previous Studies 8
2.1.1 Bell Laboratories, 1955 8
2.1.2 Lathi, 1979 9
2.1.3 Lando, 1979 10
2.1.4 Welsher, 1980 12
2.1.5 Mitchel, 1981 12
2.1.6 Augis, 1989 13
2.1.7 Rudra, 1994 15
2.1.8 Ready, 1996 15
2.1.9 Turbini, 2000 16
2.1.10 Sauter, 2002 17
2.1.11 National Physical Laboratory, 2004 18
2.2 Numerical Models to Predict CAF Formation 20
2.2.1 Welsher CAF Models 20
2.2.2 Mitchell CAF Model 21
2.2.3 Augis CAF Model 22
2.2.4 Rudra CALCE CFF Model 22
2.2.5 Li Modified CALCE CFF Model 23
2.2.6 Sun Microsystem’s Model (Based on CALCE) 24
Chapter 3: PWB Manufacturing 25
3.1 Glass Fibers 25
3.2 Production of Fiber Weaves 27
3.3 Lamination 28
3.4 Hole Drilling 29
3.5 Surface Finishes 30
3.6 Defects that may Initiate and Accelerate CFF Failures 33
3.7 Summary 38
Chapter 4: Hollow Fiber Detection 39
4.1 Introduction 39
4.2 Measurement Techniques for Hollow Fibers in Common Laminates 39
4.3 Discussion of the Hollow Glass Fiber Problem 45
4.4 Failure Opportunities due to Hollow Fibers 47
Chapter 5: Analyzing CAF Failures 52
5.1 Electrical Testing 52
5.2 Thermal Imaging 53

5.3 Superconducting Quantum Interference Device 55
Chapter 6: CFF Experiments 58
6.1 Test Board Design 58
6.2 Test Procedure 61
6.3 Experimental Testing 68
6.3.1 Insulation Resistance Monitoring 69
6.4 Failure Analysis 78
6.5 Dielectric Breakdown 83
Chapter 7: Path Formation 87
7.1 Modes of Path Formation 88
7.1.1 Mechanical Degradation 88
7.1.2 Chemical Degradation 89
7.1.3 Hollow Fibers 89
7.1.4 Vertical Filament Formation 90
7.2 Use of SQUID Microscopy in Detecting VFF 96
Chapter 8: Glass-Silane-Epoxy Bonding and Debonding 97
8.1 Voltage Dependency of Glass-Epoxy Interfacial Adhesion 97
8.2 Chemistry of Glass-Silane-Epoxy Interfacial Bonding 100
Chapter 9: Observations and Contributions 108
9.1 Observations 108
9.2 Contributions 110
Chapter 10: Summary 112
Chapter 11: Future Work 116
References 118

LIST OF FIGURES

Figure 1. Dendritic growth is shown branching from an anodic finger of a comb structure on the surface of a PWB. 3
Figure 2. Optical image of a conductive filament bridging two plated through holes in a PWB (see arrow) 4
Figure 3. E-SEM micrograph of tin whisker growth, due to mechanical stress 5
Figure 4. Fiber/resin interface delamination can occur as a result of stresses generated under thermal cycling due to a large CTE mismatch between the glass fiber and the epoxy resin (approximately 5.5 ppm/^{o}C and 65 ppm/^{o}C respectively) and poor bonding at the fiber/resin interface. Delamination can be prevented/resisted by selecting resin with lower CTE's and optimizing the glass surface finish. Studies have shown that the bond between fiber and resin is strongly dependent upon the fiber finish. 34
Figure 5. Moisture can condense in the copper/resin separated areas, allowing the copper to ionize, and migrate towards adjacent conductors. 34
Figure 6. A separation can be seen at the copper plating to fiber epoxy resin board interface. These gaps provide areas for moisture to condense and CFF to initiate. These voids which can be adjacent to inner-layer copper foils or PTH barrels, normally result from contraction of the epoxy (resin recession). 35
Figure 7. This optical image shows misregistration between a solder filled PTH and a power plane. Misregistration can decrease conductor spacing, effectively increasing the PWB's electric field strength in the closer conductor spacings. . 35
Figure 8. Copper wicking can be serious if it extends sufficiently to increase the electric field strength or decrease the internal resistance breakdown between PTHs. Furthermore it provides a convenient starting point for CAF as it effectively decreases the conductor spacing. 36
Figure 9. The anomalies seen around the PTH are known as 'micro-cracking" and are primarily caused by excessive heat or mechanical loads due to non-optimized drilling parameters. Drilling has become a very complex process with regard to the selection of optimum drill parameters for high performance materials. New drill bit compositions and geometries are most important among these factors. 36
Figure 10. Since the difference in the coefficient of thermal expansion (CTE) of the copper plating and the resin system in the PWBs is at least a factor of 13, stress exerted on the plated copper in the plated-through holes in the z-axis during thermal excursions can cause cracking. These cracks provide areas for moisture to condense and for CFF to initiate. 37
Figure 11: Hollow fibers are vacuous glass filaments in E-glass laminates which can provide paths for CAF. Generally the CAF is a two-step process, dependent upon temperature-cycling or high temperature/humidity induced debonding between the glass fibers and epoxy resin matrix in providing a path for copper migration. With the appearance of hollow fibers inside the laminates, CAF can happen as a one step process. 37

Figure 12. This photo shows the diagonal sections (black dot in middle) that are used for the hollow fiber assessments. By using only the sections on the diagonal, ensues that each hollow fiber is not accounted for more than once................... 40
Figure 13. Placing the copper cladded laminates in a chemical solution of concentrated hydrochloric and nitric acid (aqua regia), for about 10 to 15 minutes, effectively removes all exposed copper from the surfaces. This is done in a fume hood, using the appropriate protection necessary for working with hazardous chemicals. 40
Figure 14. Photo showing before and after resin removal 41
Figure 15. Light travels freely until it hits a hollow fiber (air). The change in refractive index at the fiber/air boundary partially reflects it. 43
Figure 16. A change in the refractive properties is evident through an optical microscope by a bright white line. In some cases, a hollow fiber could be detected without using a microscope. The light source is positioned so that light enters the edge of the fabric perpendicular to the fibers being observed........... 43
Figure 17. Although hollow fibers are visible to the naked eye (see arrows), a microscope attachment is best to view them.. 44
Figure 18. The edges of this sample were not dipped in wax. As the sample was submerged in oil, the oil started to flow into one of the hollow fibers. A mark was set at one point of the hollow fiber so that the movement of the oil could be more easily visualized. Only the hollow fiber is visible, due to the exact match between the refractive index of the oil and the fiber glass. 44
Figure 19. Hollow fibers can be seen as white lines traveling along the fiber bundle weave in these pictures. The refractive index of E-glass is 1.550, while that of the oil used here is 1.553. This difference of 0.003, allows the fabric weave to also be seen. 45
Figure 20. Hollow fibers are vacuous glass filaments in E-glass laminates which can provide paths for conductive filament formation (CFF). Generally the CFF is a two-step process, dependent upon temperature-cycling and humidity-cycling induced debonding between the glass fibers and epoxy resin matrix to provide a path for copper migration. With the appearance of hollow fibers inside the laminates, CFF can happen as a one step process.. 46
Figure 21. This drawing shows the PTH grid, PTH diameter (d) and the planar surface dimensions of each cell (G x G) in the PTH grid. 48
Figure 22. This E-SEM photo shows a cross-section of a printed circuit board containing two PTHs, resin and woven fiber glass.. 48
Figure 23. For a 37 x 69 grid of PTHs, where x = 37 PTH rows and y = 69 columns in the grid, the number of possible adjacent PTH failure sites can be calculated by: (37+68)(69+36) = 5,000 possible failure sites. In a square grid, where x = y, this simplifies to 2[x(x-1)] or ~$2x^2$ for x > 100. 50
Figure 24. This PWB section (half of board used by AVICI Systems) contains close to 7,000 PTHs. On the Fujitsu M-780 large-scale general purpose computer, there are more than 80,000 PTHs per circuit card. 51
Figure 25. Conductor geometry of shorted adjacent PTHs where electrical testing could verify an internal short in a PWB, after isolation from the rest of the circuitry (removal of the surface traces) is removed is shown. 53

Figure 26. The photo at the top shows the thermal imaging equipment, while the photo at the bottom shows a sequential series of snapshots (clockwise starting at top left) as the power is turned on, identifying the shorted area........................ 54
Figure 27. After locating the area by thermal imaging, cross-sectional techniques verified that there was an internal short between a PTH and ground plane. 54
Figure 28. Photo of the superconducting quantum interference device equipment.... 55
Figure 29. SQUID current mapping technique used to locate short circuit between planes in a PWB 56
Figure 30. An optical image shows the shorted site located between two planes, after cross-sectioning based on the SQUID results... 56
Figure 31. Design of the CFF test board used in this study 58
Figure 32. The photos in A and B give examples of the PTH-PTH and PTH-plane conductor geometry features respectively. 59
Figure 33. Optical dark field photo showing a cross-section of the test board's internal layer stack up 60
Figure 34. Photo shows the test board with the PTH-PTH grid and the PTH-internal plane test patterns.. 61
Figure 35. Photo of the boards hanging in the environmental chamber, parallel to the air flow and spaced approximately 2 inches apart.. 62
Figure 36. Monitoring and plotting system used to check variations in temperature and humidity settings... 63
Figure 37. Block diagram of equipment setup to monitor insulation resistance 63
Figure 38. Schematic of the electrical circuitry used for monitoring the insulation resistance.. 64
Figure 39. The normal current path is shown in red, going through a shorting box... 65
Figure 40. The current path, shown in red, obtained by "opening" the shorting box, was used when a device was being tested.. 65
Figure 41. Light colored wires were used for the positive connections (yellow and white) while the darker colored wires (purple and blue) were used for the negative connections. This nomenclature helped to avoid polarity mix-ups...... 67
Figure 42. Moisture absorption characteristics for the four board types exposed to 85°C/85% RH for 700 hours is shown.. 68
Figure 43. Plot of the PTH-PTH insulation resistance for the 20 samples exposed to 85°C/85% RH at a 10-volt bias.. 69
Figure 44. Plot showing PTH-PTH intermittent nature of the failures....................... 70
Figure 45. Intermitent failures can last for less than 6 minutes. Monitoring every 24 hours according to IPC-TM-650 specifications may not catch these short duration failures. 70
Figure 46. Plot showing internal resistance of the PTH-plane in the powered samples. Isola samples, IS 70A and IS 70C, failed between 30 and 130 hours. The missing data section was due to a power outage... 73
Figure 47. Plots of the resistance in the PTH-plane show intermittent behavior. 73
Figure 48. Close to the end of the 50-volt testing of the PTH-plane circuitry, 8 surviving samples can be seen above the lines above 1E8 ohms. 74
Figure 49. This plot shows the insulation resistance monitored at 100 volts for the duration of 500 hours. Some of the samples did not fail. 76

Figure 50. This plot shows the insulation resistance for the PTH-PTH XG samples up to 40 hours, at which time all had failed. 76
Figure 51. The SQUID output shows the current mapping images, verifying that there were short circuits and determining their locations respective to the board conductors. 78
Figure 52. SQUID mapping and respective conductor locations for cross-sectioning. 79
Figure 53. Prior to reaching the failure site, circular black blue areas, possibly $Cu(OH)_2$ due to reaction with water were observed. 79
Figure 54. A filament was observed bridging two PTH, at the same location predicted by the SQUID (see red arrow). 80
Figure 55. This optical micrograph shows an enlargement of the shorted site. 81
Figure 56. This current mapping of one of the failed XG samples at the PTH-PTH grid show that the current follows the grid pattern, and contains many leakage paths; not one as in the CFF validated failures. It is possible that these were the same type of early failures in the AF samples as well. 81
Figure 57. This optical photo shows a copper filament bridging a PTH and ground plane at the precise location predicted by the SQUID. 82
Figure 58. An EDS analysis of a cross-sectioned site perpendicular to the filament showed copper in the shorted location. 82
Figure 59. E-SEM inspection revealed delamination at the fiber-epoxy interfaces in areas immediately surrounding the failure site. 83
Figure 60. Photos show the damage to the PTH as a result of the dielectric breakdown testing. 85
Figure 61. Three common CFF pathway configurations 87
Figure 62. Optical micrograph, under brightfield lighting, of a void observed during cross sectioning of a board. 91
Figure 63. Optical micrograph, using differential interference contrast, of a vertical cross-section of the board. The filler agglomerate has maximum dimension of 3.5 mil (87 microns). A yellow arrow marks what appear to be nodules of copper emanating from layer 10 (power). 92
Figure 64. Optical micrograph of a vertical cross-section showing what appears to be a nodule in the PWB. 93
Figure 65. Particle observed in the center of a “mound” 94
Figure 66. Area containing a particle bridging two copper planes shown. 95
Figure 67. Particle seen in material bridging two copper planes. 96
Figure 68. Schematic of reaction between organosilane and glass surface 99

CHAPTER 1: INTRODUCTION

1.1 Electrically Induced Failures in Printed Wiring Boards

Conductive filament formation (CFF) also known as metallic electromigration and conductive anodic filamentation (CAF), is a failure observed within the bulk of glass-reinforced epoxy printed wiring board (PWB) laminates. This phenomenon is an electrochemical process involving the transport, usually ionically, of a metal through or across a nonmetallic medium under the influence of an applied electric field. The growth of the metallic filament is a function of temperature, humidity, voltage, laminate materials, manufacturing processes and the geometry and spacing of the conductors. The growth of these filaments can cause an abrupt, unpredictable loss of insulation resistance between the conductors under a DC voltage bias.

This failure mode was first observed at Bell Laboratories located in Whippany, New Jersey, in 1976 [1]. However, more recently there has been an increase in reliability concerns due to CAF failures. Three of the driving forces behind these reliability concerns are:

1. The trend toward more compact and lighter electronic devices using smaller PWBs geometries and multi-layered boards
2. The increase in use of electronic products for high reliability and safety critical applications (avionics, automotive, medical and military) in harsh environments

3. The higher board processing temperatures, due to the implementation of lead-free electronics, can affect laminate stability and limit material choices

These factors have increased the focus on conductive filament formation and resulted in testing standards such as IPC-TM-650-2.6.25 (Conductive Anodic Filament Resistance Test), the fabrication of CAF resistant laminates and companies annually spending millions of dollars on research to gain a more in-depth understanding of CAF failures.

1.2 Electrochemical Migration

Electrochemical migration may be defined as the growth of conductive metal filaments in a printed wiring board (PWB) under the influence of a direct current voltage bias. This may occur on an external surface, or through the bulk of a composite material (e.g., glass fiber/epoxy resin laminate) [2]. Growth occurs by electro-deposition from a solution containing metal ions. These ions are dissolved at one conductor, transported by the electric field and re-deposited at the other (oppositely biased) conductor.

Two distinct electrochemical migration phenomena can occur in PWBs. In the first case, surface dendrites have been observed to form from the cathode to the anode under an applied voltage when surface contaminants and moisture are present (see Figure 1). If the voltage bias is sufficiently high, the dendrites bridging the gap between the anode and the cathode may “blow-out” (similar to a fuse), leaving

sludge-like debris on the surface. These filaments are fragile and may be destroyed by oxidation, changes in surface tension during moisture absorption, drying, cooling or heating, or blown-out if the current is sufficient. Short circuits therefore tend to be intermittent, but filaments can reform.

Figure 1. Dendritic growth is shown branching from a cathodic finger of a comb structure on the surface of a PWB.

The second form of electrochemical migration and the focus of this dissertation is conductive filament formation (CFF), also referred to as conductive anodic filament (CAF) formation (see Figure 2). CFF differs from the surface dendritic growth in a number of ways:

- In CFF, the migrating metal is usually copper, as opposed to tin or lead in dentritic growth.

- In CFF, the direction of the filament growth (in the case of copper conductors) is from the anode to the cathode, not from the cathode to the anode as observed in dendritic growth.
- In CFF, the filament is composed of a metallic salt, not neutral metal atoms as in dendritic growth.
- In CFF, the phenomenon occurs internally, not on the surface or superficially as in dendritic growth.

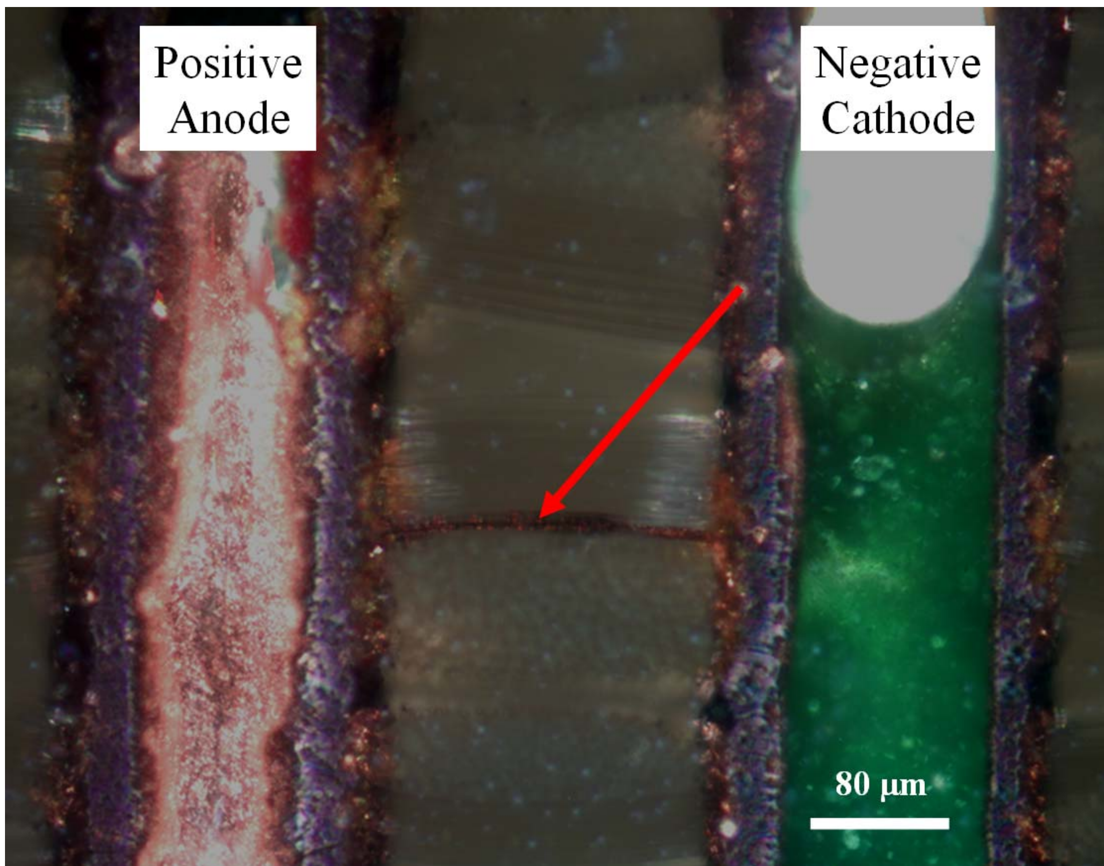

Figure 2. Optical image of a conductive filament bridging two plated through holes in a PWB (see arrow)

Electrochemical migration should not be confused with whisker growth, which is induced by mechanical stress, and not electrically driven (see Figure 3).

CFF failures have three distinct signatures:

1 Intermittent short circuiting - in this case, the conductive filament bridging the two shorted conductors blows out due to the high current in the filament (similar to a fuse), but can reform again. These tend to be diagnosed as no fault detected (NFD) or cannot duplicate (CND) failures.

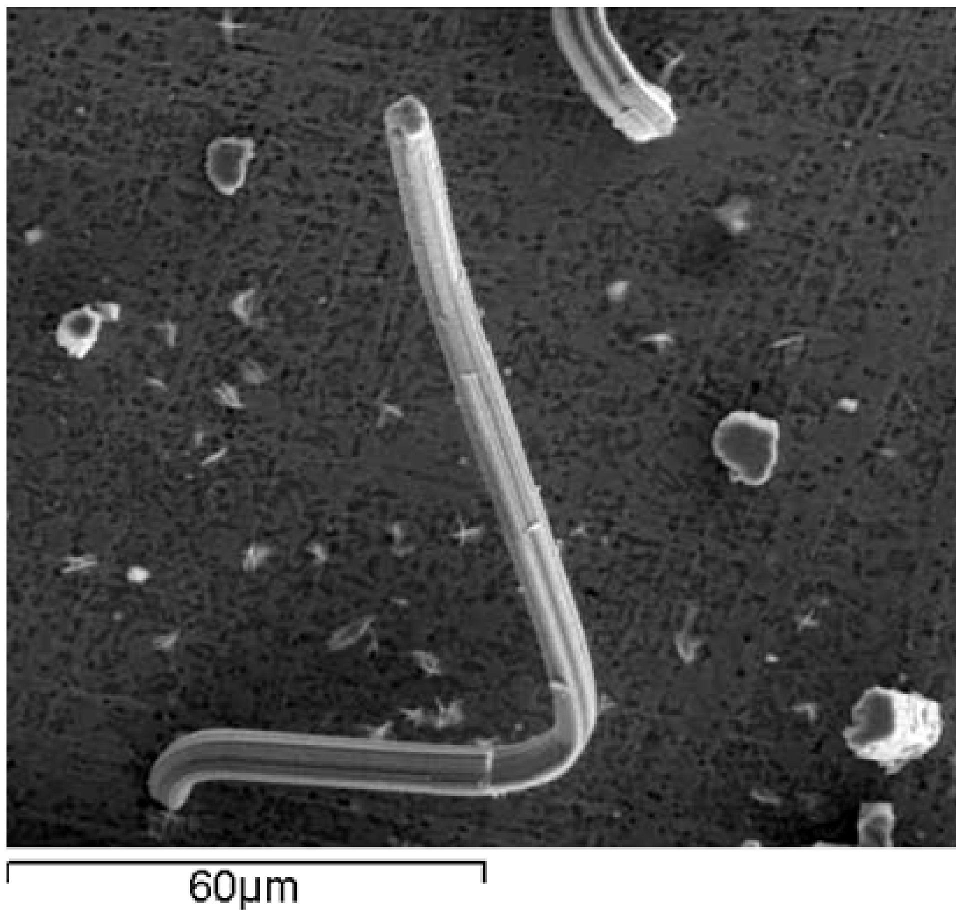

Figure 3. E-SEM micrograph of tin whisker growth, due to mechanical stress

2 Conductive filaments fully or partially bridging conductors – these typically occur in current limiting accelerated tests where once a short circuit is formed, the

current is limited by a resistor in series with the applied voltage, preventing burnout and preserving the conductive filament.

3 Burnt or charred areas between shorted conductors - most of the field failures display this failure signature; internal shorting characterized by a dark charred epoxy resin/glass fiber area, between and often connecting the conductors involved.

1.3 Motivation

Laminates are found in almost all electronics products (organic printed boards make up over 90% - standard FR-4 represents 85% of the resin systems of the present types of interconnecting substrates). If an electrical short occurs in a printed wiring board (PWB), there is a potential for the entire system to fail.

A comparison of the failures investigated by the CALCE Failure Analysis Laboratory shows that 26% of the failures were PWB related. From this population, failure analyses to determine a root-cause showed that a significant number of the failures were due to CFF.

As PWBs continue to increase in density by using tighter pitches as well as thinner, single-ply dielectrics coupled with higher voltages and higher processing temperatures (resulting from the use of lead-free solder), the potential for CFF-caused failures will also continue to increase. Hence to prevent these types of catastrophic failures, it is necessary to understand the roles and synergistic effects of environ-

mental conditions, material properties and manufacturing quality in accelerating or deterring CFF.

CHAPTER 2: BACKGROUND

2.1 Previous Studies

2.1.1 Bell Laboratories, 1955

Researchers from Bell Laboratories in 1955 observed that silver in contact with insulating materials under an applied electrical bias can be ionically removed from its initial location at an anode and be re-deposited as metal at a different location at a cathode [3]. A major requirement for the process is the adsorption of water on the insulating surface to act as the electrolyte. Examination of the metal re-deposited at the cathode revealed a dendritic structure, while the deposits at the anode appeared brownish and colloidal. Since silver was the only metal at that time to cause a potential hazard, the process was called silver migration. Parameters which were identified as affecting the silver migration rate were; the properties of the insulating material, the DC voltage, time of the voltage application and the percent relative humidity. Phenol fabric, the insulating material between the metals was found to be susceptible to silver migration. The rate of the migration was observed to increase with voltage and relative humidity. Mitigation techniques suggested included resin impregnation to more effectively isolate fibers, pretreatments of fibrous surfaces with water repellant agents and the use of silver precipitating agents to capture free silver ions.

2.1.2 Lathi, 1979

In 1979, Lahti et al. [4] conducted experiments on configurations of single sided, double sided and multilayered rigid PWBs with and without plated-through-holes (PTHs) with conductor spacings ranging from 5 mils to 50 mils, temperatures from 23° C to 95° C, relative humidities from 2% to 95% and test voltages ranging from 10V to 600V. They observed that while monitoring CAF failures, there is little or no degradation in insulation resistance up to the point of failure. Hence, prior to failure, is it difficult to anticipate or predict failure by examining or monitoring insulation resistance. Also seen was that the mechanism responsible for CAF failures involves the penetration of the glass/epoxy interface by a conductive copper compound generated by electrochemical activity at the anodically biased conductors. The first indication that the mechanism has initiated is the visual enhancement of the glass reinforcement around the anodes due to the physical separation at the glass/epoxy interface. Dark copper-bearing material then begins to fill the articulated regions, growing away from the anodes. The growth of the copper-bearing material follows the reinforcement in many directions, but ultimately preferentially towards the cathodically biased conductors. The researchers observed that at spacings less than 5 mils, failure times dropped drastically. Lot to lot variability in the CAF resistance of the epoxy-glass printed wiring boards was also noted; one lot may perform better at 400V than another set at 45V. No substantial differences were noted in testing materials manufactured five years ago, compared to, at that time, currently manufactured laminates. Among the variables observed to affect the susceptibility of a PWB to CAF, the most important appeared to be raw materials. Processing factors

such as process chemistry and lamination parameters in addition to assembly parameters such as fluxing, soldering, cleaning and baking were shown to influence the propensity of a PWB to CAF failure. From the tests, it was concluded that the CAF failure mechanism is voltage sensitive, but not highly so; the dependence was not found to be greater than 1/V. In this study, failures occurred first on the most deeply buried layers and later in the layers closer to the board surface.

2.1.3 Lando, 1979

Lando et al. [5] in 1979 proposed a two-step model to explain the growth of the conductive filaments occurring at the resin-glass interface in PWBs. The first step is the degradation of the resin-glass interfacial bond followed by a second step, the electrochemical reaction. According to Lando's hypothesis, the path required for the transportation of metal ions, formed by the degradation of the resin-glass interfacial bond, may result from mechanical release of stresses, poor glass treatment, hydrolysis of the silane glass finish or stresses resulting from moisture induced swelling of the epoxy resin. The path formation was reported to be bias independent, but possibly humidity sensitive, in the case of chemical degradation. After path formation, the PWB may be viewed as an electrochemical cell. In this cell, the copper conductors are the electrodes, the sorbed water is the electrolyte and the driving potential for the electrochemistry is the operating or test potential of the circuit. The electrode reactions proposed for the metal migration were:

At the anode

$$Cu \rightarrow Cu^{n+} + ne^{-} \tag{1}$$

$$H_2O \rightarrow \frac{1}{2}O_2 \uparrow + 2H^+ + 2e^- \qquad (2)$$

At the cathode

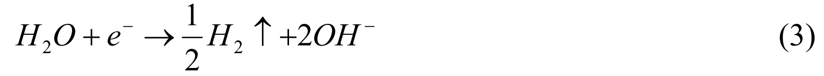

$$H_2O + e^- \rightarrow \frac{1}{2}H_2 \uparrow + 2OH^- \qquad (3)$$

The electrolysis of water creates a pH gradient between the electrodes since hydronium ions are produced at the anode while hydroxide ions are produced at the cathode. Using a simplified Pourbaix diagram for copper, a drop in pH at the anode allows Cu corrosion products to be soluble until reaching a neutral region where they will be insoluble and thus deposit along the epoxy-glass interface was explained. The materials tested included standard FR-4 material from six suppliers using barrier coatings of resin (1 – 4 mils thick) in addition to various glass treatments. G-10, polyimide and triazine, all with woven glass, along with polyester (woven and chopped glass) and epoxy with woven Kevlar were tested. The parameters of the tests were a continuous DC bias: ranging from 200 – 400 V, 80% RH, 85°C, line-line, hole-hole and hole-line conductor test patterns with and without surface coating. Lando concluded that susceptibility to CAF growth may depend on conductor configuration in decreasing order of susceptibility: hole-hole > hole-line > line-line. Mitigation strategies proposed included separating the resin/glass from the conductors by resin rich areas, using traizine laminates and improving the glass finish to allow stronger interfacial bonding at the glass fiber-epoxy resin interface.

2.1.4 Welsher, 1980

In 1980, Welsher and other researchers at Bell Laboratories [6] conducted extensive tests on triazine-glass, a CAF resistant material. The test boards were fabricated with a hole-hole grid test pattern with 42 mil diameter PTHs on 75 mil centers, with a minimum conductor spacing of 35 mils. Welsher proposed a two-step model consistent with that proposed by Lando in 1979 [5]. The tests showed that exposure of a PWB to thermal transients, such as thermal shock or during multiple soldering steps, could significantly reduce its CAF resistance. The application of an intense thermal transient accelerates debonding of the fiber-epoxy matrix interface due to the coefficient of thermal expansion (CTE) mismatch between the fiber and epoxy. A delayed application of DC bias test showed that delaying the application of the DC bias does not significantly affect the time to CAF failure of boards. This confirmed the two-step sequential rather than parallel process proposed for the CAF formation. It was also shown that the mean time to failure due to CAF may not be sensitive to whether the applied DC bias is continuous or intermittent. Accelerated tests comparing the resistance of FR-4 and triazine to CAF failures, demonstrated that boards manufactured with triazine can exhibit a life at least 20 to 30 times that of the FR-4s tested.

2.1.5 Mitchel, 1981

Mitchel and Welsher in 1981 [7], observed that failures due to filament formation showed an Arrhenius temperature dependence over the temperature range of 50°C to 100°C. Analysis of the delayed bias tests, from the previous study [6], showed that

the growth takes place in two sequential steps, where MTF is equal to the time for step 1 (path formation) plus the time for step 2 (electrochemical reaction), and that during the first stage of the failure process, an applied voltage is not necessary. In another pair of experiments, the reversibility of the two sequential steps was studied. In the first experiment, two sets of FR-4 samples were exposed to 85°C/80% RH; the first set for 240 hours, the second set for 168 hours. The second set was dried at 85°C for 72 hours. Both sets were then tested at 85°C/80% RH/200V. All samples in the first set failed within four hours, while the MTF of the second set of samples was 122 hours. From this study, it was concluded that step 1, the interfacial degradation, is essentially reversible, in agreement with studies on hydrolysis of glass-polymer coupling agents. To test the reversibility of the second step, the electrochemical migration, several samples, after failing at 70°C/85% RH/200V were dried at 70°C for 330 hours and then retested again at 70°C/85% RH/200V. The MTF before the drying was 292 hours while the MTF after the drying was 54 hours. It was thus concluded that once the filament has formed, it is permanent. In addition, several printed circuit materials were studied to determine their susceptibility to CAF growth. From this study, woven glass laminates with resins of triazine, bismaleimide triazine and polyimide were observed to offer the best hole-hole CAF resistance.

2.1.6 Augis, 1989

Augis et al. [8] in 1989 indicated that there appears to be a threshold in relative humidity below which CAF would not occur. It was important to identify this threshold since linear acceleration factor models used for extrapolating reliability

broke down (i.e. a material that performed poorly under highly accelerated conditions could have acceptable characteristics under normal operating conditions). Tests showed that newly manufactured boards compared to aged boards showed no difference in CAF resistance during accelerated tests. Step stress tests run over a long period of time showed that above certain humidity levels the percentage of CAF failures increased rapidly. Hence, it was concluded that in humidity-controlled environments, CAF failures may not be a threat. Elemental analysis of the conductive filaments in the study always showed copper and sometimes either chlorine or sulfur associated with the filament. The chlorine and sulfur were believed to be from the fabrication processes.

It was speculated that the filament grows from the anode to the cathode, and the degradation mechanism most likely involves these four steps:

1. Diffusion of water into the epoxy
2. Migration of ions (Cu^{++}, Cl^-),
3. Corrosion ($Cu \rightarrow Cu^{++}$)
4. Chemical reactions such as breaking of the silane bonds at the fiber/epoxy interface (may be due to hydrolysis)

A wide variability in median time to failure under same environments using different lots of material was also observed.

2.1.7 Rudra, 1994

Rudra et al. [9] in 1994 conducted experiments using three PWB materials - FR-4, bismaleimide triazine (BT) and cynate ester (CE), two humidity levels – 70% and 85% RH, two temperatures – 70°C and 85°C, and two DC voltages – 300 and 800 volts. Each test boards had six layers, ten different spacings and six conductor geometries. The conductor geometries were PTH-to-plane, line-to-line, line-to-PTH, corner-to-PTH, PTH-to-PTH, and non-plated through hole-to-line. The conductor spacings varied from 5 mils to 65 mils. Six different surface coatings were also tested. From this study, it was concluded that BT and CE PWB materials are more resistant to CAF than FR-4 boards. BT and CE also had lower moisture absorption percentages. The presence of a post coat (a type of conformal coating) increased the time-to-failure due to filament formation, while a solder mask in addition to the post coat offered the highest resistance to filament formation. For the various conductor geometries tested, PTH-to-PTH was the most susceptible failure site, followed by line-to-PTH and then line-to-line. It was observed that geometries on the surface layer tend to fail faster than the geometries on the inner layers. An empirical model, based on the failure data from the FR-4 laminates, was developed to assess the time to failure due to conductive filament formation. In this model temperature and humidity were combined into a threshold moisture content based on Augis' findings.

2.1.8 Ready, 1996

Ready et al. [11] postulated that elevated bromide levels detected by EDX analysis in the area of a CAF failure may not have come from the board itself, but rather from a

processing step. The presence of HBr in the soldering flux used during the problematic period suggests that this may be the source of the bromide. In this case, the bromide is speculated to have diffused through several layers of a 14 layered board during the soldering process at temperatures above 200°C. It was observed that substrates processed with fluxes containing certain polyglycols seem to exhibit an affinity for CAF formation. It appears that these polyglycols can also increase the moisture absorption of the laminate.

2.1.9 Turbini, 2000

Turbini et al. [12] examined the effect of certain water-soluble flux vehicles, both with and without halide activators, at processing temperatures of 201°C and 240°C in enhancing CAF formation. These two temperatures were selected to reflect both the expected peak temperature in wave soldering for traditional eutectic solder and for a typical lead-free solder. Using standard IPC-B-24 test coupons, it was observed that at the higher processing temperature, the occurrences of CAF failures greatly increased. It was speculated that this increase in CAF failures at the higher temperature was due to the enhanced diffusion of polyglycols into the boards during the wave soldering. Since the diffusion process follows an Arrhenius behavior, the length of time during reflow that the board is above its glass transition temperature will have an effect on the amount of polyglycol absorbed into the epoxy. Higher reflow temperatures also lead to greater thermal strains due to the CTE mismatches between the glass fibers and the epoxy resin.

2.1.10 Sauter, 2002

Sauter [10] from Sun Microsystems describes testing parameters and design features that CAF test boards should incorporate to effectively assess CAF vulnerability in today's electronics. Some CAF test boards/coupons have been designed with only twenty PTHs and a few layers, not representative of today's higher layer count boards with thinner dielectrics. Sun Microsystems developed a ten-layer board with 168 potential in-line PTH-PTH failures per spacing/test daisy chain and 312 potential diagonal PTH-PTH failures per spacing/test daisy chain. The data analysis techniques require 25 or more boards to be run per sample lot per bias level, giving 4,200 potential in-line hole-hole failure sites and 7,800 potential diagonal hole-hole failure sites per sample lot. This design has been made available to IPC (Institute for Interconnecting and Packaging Electronic Circuits) for industry use. Telcordia uses a 1,000 hour test while Sun uses a 500 hour duration period. Sauter also recommends that a temperature of 65°C be used instead of 85°C to reduce the risk of sublimation which can artificially reduce the activity of flux residues or other residues that may remain when certain board finishes are used, resulting in an erroneous assessment of CAF reliability risk. Sauter has found that some laminates, which offer significantly more CAF resistance at larger spacings, could perform poorly at smaller spacings. It was shown that although the Bell Labs and CALCE CAF prediction models appear to be quite different, the Bell Labs model and the adjusted CALCE model both predict a similar 8x increase in CAF failure risk for the same decrease in conductor spacing. The modification to the CALCE model was made to include the readily conductive region around the PTHs. From test failure data, Sauter concluded that some high T_g

(glass transition temperature) FR-4 laminate materials for some PWB manufacturers show less resistance to CAF than standard T_g FR-4 materials. Since the combination of the PWB board finish and glass weave direction has a significant impact on CAF testing results, the most vulnerable combination, HASL-finished boards tested in the machine direction, is recommended for evaluating the CAF susceptibility of a PWB.

2.1.11 National Physical Laboratory, 2004

In 2004, research scientists at the National Physical Laboratory [13] conducted two phases of accelerated tests to characterize conductive anodic filamentation. The first phase was aimed at understanding the effects of PTH geometries, voltage levels, and thermal effects such as thermal shock and lead-free reflow, on a typical FR-4 laminate. Phase 2 incorporated improvements of the test board design based on lessons learned from phase 1. Phase 2 also compared different laminate types, glass reinforcements, drill feed speeds and other laminate manufacturing variables.

In phase 1, standard T_g non-CAF resistant FR-4 boards with an electroless nickel immersion gold finish and no solder mask were tested. Each board had ten layers and more than 6,000 PTHs. The test voltages used ranged from 5 volts to 500 volts, while the conductor spacings ranged from 300µm to 800µm (in-line and staggered PTHs), and from 100µm to 200µm (anti-pad annulus). The parameters of the thermal shock were: -15°C to +120°C, cycle time of 14 minutes, with a 5 minute dwell in each bath. Selected samples were exposed to 250 thermal shock cycles. The peak temperature used for the lead-free reflow was 250°C and the boards were put through three times.

The testing was conducted at 85°C/85% RH for a duration of 1000 hours. The findings from phase 1 were that lead-free reflow increased CAF susceptibility while thermal shock had a negligible effect, MTF for in-line PTHs $<$ staggered PTHs $\approx$ anti-pad, CAF occurs faster at higher voltages, CAF occurs faster at smaller spacings, and MTF is not strongly dependent on anti-pad gap spacing. NPL also determined that the relatively fast initial filament growth slows as it moves further away from the anode.

Phase 2 compared the CAF resistance of two manufacturers, both with CAF resistant and non-CAF resistance, and high and low T_g laminates. The effect of different drill feed speeds and surface finishes (electroless nickel immersion gold, silver, hot air solder level and organic solderable preservative) on the time to failure for CAF were also examined. Two reflow peak temperatures were used, 210°C and 250°C.

The test results from phase 2 indicated that a higher reflow temperature promotes faster CAF growth. This, in conjunction with the negligible thermal shock effect, implies that perhaps the mechanism for damage in the laminate is not based on CTE mismatches between the materials, but rather a chemical or physical breakdown above a certain critical temperature. It was observed that in the anti-pads, failure occurs faster if the PTH is positively biased and the plane is negatively biased, and slower if the PTH is negatively biased and the plane is positively biased. Also seen was that PTHs closer together fail faster, even for the same electric field. In all laminates tested, the CAF resistance laminates offered extended life of different percentages compared to their non-CAF resistant counterparts. The CAF resistant

laminates delayed the time to failure due to CAF, but did not prevent it. CAF failures occur faster along the fabric weave in the machine direction. Identically specified laminates from different board manufacturers can have significantly different resistances to CAF. The tendency for failure to occur in a specific fabric glass style within the laminate weave-stack-up, can vary from manufacturer to manufacturer. The parameters that had the most significant impact on CAF resistance are firstly the manufacturer and secondly the materials. Parameters that had negligible effects on the time to failure due to CAF were; surface finishes, high or low T_g designation, and drill feed speed.

2.2 Numerical Models to Predict CAF Formation

2.2.1 Welsher CAF Models

Welsher et al. [7] proposed a two-step model, consistent with the two-step CAF failure process. The first step is voltage dependent, while the second step is temperature-humidity dependent. The voltage dependent model is given in equation 4:

$$MTF = a + b/V \tag{4}$$

where V is the applied voltage and a and b are positive material-dependent constants. The second temperature-humidity dependent model is shown in equation 5:

$$MTF = a(H)^b \exp(E_A / RT) \tag{5}$$

where H is the relative humidity, R is the gas constant, T is temperature in Kelvin, a and b are material dependent constants and E_A is the activation energy for the process.

Welsher then combined equations 4 and 5 and developed the model shown in equation 6:

$$MTF = a(H)^b \exp(E_A / RT) + d(L^2 / V) \tag{6}$$

where a and b are material dependent constants, H is the relative humidity, E_A is the activation energy for the process, R is the gas constant, T is temperature in Kelvin, L is the conductor spacing in mils, V is the applied voltage and d describes the temperature and humidity dependence.

2.2.2 Mitchell CAF Model

Mitchell and Welsher, to accommodate different conductor geometries, further developed the model given in equation 6. If the temperature and humidity dependencies for each step in the CAF process are equal, then they can both be approximated by a single constant:

$$a(H)^b \exp(E_A / RT) \tag{7}$$

The revised CAF model which was proposed is given in equation 8:

$$MTF = \alpha \cdot \left(1 + \frac{\beta \cdot L^n}{V}\right) \cdot H^\gamma \cdot \exp(E_A / RT) \tag{8}$$

where α and β are material dependent constants, L is the conductor spacing in mils, n correlates to the orientation of the conductors, V is the applied voltage, H is the relative humidity, γ is a humidity dependent factor, E_A is the activation energy for the process, R is the gas constant, and T is temperature in Kelvin. For the PTH-PTH

conductor orientation, n is equal to four. This equation is valid for temperatures ranging from 50°C to 100°C and a relative humidity range of 60% to 95%.

2.2.3 Augis CAF Model

Augis et al. [8] identified the existence of a moisture threshold for filament formation and concluded that the linear acceleration factor extrapolations for the high stress testing used earlier by Bell Labs were not valid. Augis observed that for a 50 V circuit operating at 25° C, the critical relative humidity necessary to initiate CAF formation was approximately 80%. A quantitative model to predict this critical threshold value was developed. This model is given in equation 9.

$$RH = \exp\left[\frac{2.3975 + \ln(c) + 10484/T - 1.52 \cdot \ln(V)}{5.47}\right] \tag{9}$$

2.2.4 Rudra CALCE CFF Model

Rudra et al. [9] in conducting research at the CALCE Electronic Packaging and Research Center used a physics of failure approach to determine that several factors were involved in determining the time to failure due to conductive filament formation. These factors were: external operating conditions including temperature, operating voltage and humidity, laminate parameters including material type, surface coating (solder mask, solder plate and post coat) and the geometry and spacing of the conductors. The model that was developed is given in equation 10:

$$t_f = \frac{a \cdot f \cdot (1000 \cdot L_{eff})^n}{V^m \cdot (M - M_t)} \tag{10}$$

where t_f is time to failure in hours, a is the filament formation acceleration factor for different surface conditions and laminate material, f is the multilayer correction factor, n is a geometry acceleration factor (determined to be 1.6), V is the applied voltage, m is a voltage acceleration factor (determined to be 0.9), M is the moisture content, M_t is the threshold moisture content (determined to be 0.35), and L_{eff}, the effective length between conductors, is the product of k - the shape factor (ranged from 0.53 to 1.13) and L - the spacing between the conductors in inches. The threshold moisture content was calculated using the Augis model for different voltages and temperatures. Although it may appear that there is no temperature dependence in the model, the temperature dependence is accounted for in the calculation of the threshold moisture content (function of temperature and relative humidity), thus eliminating the necessity for an explicit temperature term.

2.2.5 Li Modified CALCE CFF Model

The CALCE CFF diffusion controlled reaction model proposed by Li et al. [14] for initiation of the CAF failure mechanism was modified by Sauter [10] to include the extent of readily conductive region (D) around PTHs based on failure data for FR-4 laminates tested at 100 volts DC bias and 10 volts DC bias. The revised model is given in equation 11:

$$t_f = \left[\frac{p \cdot a \cdot R \cdot T \cdot (L - (2 \cdot D))^2}{2 \cdot n \cdot F \cdot M \cdot C' \cdot H \cdot V} \right] \cdot \exp(E / RT) \qquad (11)$$

where t_f is time to failure, p is the density of copper, a is the volume fraction of filament, R is the gas constant, T is temperature in Kelvin, L is the initial electrode

spacing, D is the extent of readily conductive region surrounding the PTH, n is the number of valence electrons (n=2 for Cu^{++}), F is Faraday constant (charge of one mole of electrons), M is the ion mobility constant (for FR-4), C' is the copper ion concentration, H is the relative humidity, V is the applied voltage bias and E is the activation energy.

2.2.6 Sun Microsystems Model (Based on the CALCE Model)

A model to predict time to failure was developed by Sun Microsystems, based on the CALCE model. This model, shown in equation 12, accounts for laminate materials, PTH height (same as board thickness) and the PWB manufacturing process:

$$t_f = K \cdot P \cdot \left[\frac{(L - (2 \cdot D))^2}{H \cdot V \cdot T} \right] \tag{12}$$

where t_f is time to failure, K is the laminate material constant at standard temperature, P is the PWB manufacturing process, L is the initial electrode spacing, D is the extent of readily conductive region surrounding the PTH, H is the relative humidity, a is the volume fraction of filament, V is the applied voltage bias and T the board thickness.

If parameters likely to be constant for a given laminate and test condition are grouped together, this equation can be simplified to equation 13:

$$t_f \propto \left[\frac{(L - (2 \cdot D))^2}{V} \right] \tag{13}$$

where the time to failure is proportional to the square of the effective distance divided by the voltage. The effective distance is $L-2D$.

CHAPTER 3: PWB MANUFACTURING

The printed wiring board manufacturing process can have an effect on the vulnerability of the board to CFF failures. The critical areas during this process where manufacturing defects, that can initiate or accelerate conductive filament failures, can be introduced, are:

1. Glass fiber manufacturing,
2. Lamination,
3. Drilling and
4. Hot air solder leveling (HASL)

Each of these areas is discussed in more detail in the following sections.

3.1 Glass Fibers

Glass fibers are widely used in reinforced plastics because they are inexpensive to produce and have relatively good strength to weight characteristics. In addition, glass fibers also exhibit good chemical and fire resistance. Electrical (E) glass, a low-alkali composition which exhibits an excellent balance of electrical insulation properties and good resistance to water, is the most widely used reinforcement material for cost-effective electronic applications (see Table 3.1 for typical compositions of different glass types).

Manufacturing of glass fiber begins with the dry mixing of silicas, limestone, clay, and boric acid in appropriate proportions. In the direct-melt process, the mixture is melted in a refractory furnace at temperatures between 2600 and 2800 ^{o}F (1427 and

1538 ^{o}C) and fed directly into bushings, which are platinum alloy trays with thousands of precisely drilled tubular openings called bushings. Alternatively, the melt can be formed into marbles, cooled to room temperature and stored for future use.

A homogeneous melt composition with negligible impurities is necessary for the successful manufacture of glass fibers. Solid inclusions of even sub-micron dimensions can act as stress concentrators that reduce the fiber strength. Furthermore, the decomposition of raw materials during glass melting can lead to trapped gases. In the raw materials, water, carbonates (CO_3), and organic materials will decompose with heat to form gases. Depending on the viscosity of the glass mixture and various manufacturing processes, these gases can get trapped as bubbles, called seeds. Seeds are a naturally occurring part of the process and thus methods to remove them are necessary. One approach is fining. Fining removes gases by adding gases (i.e., SO_2), which create nucleation sites for bubbles to coalesce and escape the melt. Fining can also be defined as increasing the temperature and modifying the heat flow pattern so bubbles are moved in positions to readily reach the surface and escape.

Table 3.1. Typical Chemical Weight % Composition of Major Components in Fiberglass [Watt and Perov, 1985]

Composition	E-Glass	A-Glass	C-Glass	S-Glass
SiO_2	54.8	72.0	65.0	65.0
Al_2O_3	11.5	0.6	4.0	25.0
B_2O_3	5.5	-	5.5	0.01
CaO	18.0	10.0	14.0	0.01
MgO	5.0	2.5	3.0	10.2
K_2O	0.8	14.2	8.5	
BaO	-	-	-	0.2
Fe_2O_3	0.1	-	-	0.2

After the molten glass is poured into the bushing, glass fibers are produced by drawing a solidified filament of glass from a molten drop. The diameter of a glass fiber is typically between 5 and 25 microns. During drawing, any seeds present will become attenuated and elongated, forming capillaries several meters long in the glass filaments and effectively creating hollow fibers [Morley 1987]. These hollow fibers can provide a path for conductive filament formation.

3.2 Production of Fiber Weaves

Individual fibers being drawn from the nozzles in the bushing pass through a light water spray and then over an applicator that transfers a protective and lubricating size onto the filaments. Glass fibers are then gathered together to form a strand and wound on a rotating cylinder called a “collet”. When winding glass fibers on collets at high velocity, breakage of the fibers can take place due to the mutual friction of the fibers as well as friction against directing parts. Fiber sizes, also known as coatings, are applied to the surface of fibers to prevent loss of strength and damage to the fibers

during the manufacturing process. Lubricants, fed in the region of formation, can minimize this breakage. Besides solvents, these lubricants contain sticking substances, plasticizers and emulsifiers. Distilled water is commonly used as a solvent, whereas latex, paraffin, starch and gelatin are used for fibers sticking and vegetable and mineral oils as plasticizers. Coupling agents may also be applied when the fibers are going to be embedded in a polymeric matrix, to improve bonding between the fibers and the matrix. Bonding is important if the composite material is required to perform under various temperature and humidity conditions. It has been found that hydroxyls present on the surface of glass fibers can increase moisture affinity to the glass.

The term strand refers to a unidirectional bundle of fibers (102, 204 or 408 fibers/bundle) drawn from a single bushing. The strands are then twisted into yarns. In the electronic substrate industry, the yarns are typically woven into a plain weave fabric, which is impregnated with an epoxy to form a laminate.

3.3 Lamination

During the lamination process the thin-core inner-layers are subjected to heat and pressure and compressed into a laminated panel. Sheets of material consisting of glass fibers impregnated with epoxy resin, known as pre-preg or b-stage, are slipped between the layers and bond the layers together. Pre-preg is available in different styles with varying ratios of resin to glass fibers. This choice of differing epoxy resin to fiber glass ratios allows the manufacturer to control the thickness between layers

and to provide the appropriate amount of resin flow between circuitry. Lamination steps are fairly consistent among manufacturers. All of the materials, including the inner-layers and pre-preg, are tooled to the same registration system and held in place by tooling pins. Several panels can be pressed together in one set of heavy plates, creating what is known as a "book". In lamination, the pressing parameters must closely match what the laminator recommends. If the heat rise of the pressed book is too fast or too slow, the resin will not have enough time to properly wet-out the cores that are being pressed. Laminate voids or other lamination defects may occur, allowing paths for CFF failures.

3.4 Hole Drilling

Holes are drilled through the PWB to interconnect circuitry on different layers and to also allow for the insertion of components. The etched innerlayer pattern will extend to the barrel of the hole and therefore will be interconnected with the other layers when the hole barrel is made conductive in a later step. Most drilling is performed with computer numerical control (CNC) equipment, but as hole sizes less than 0.012 inches have become more common, other methods of making small holes are increasing in popularity. Two alternate methods are punching and laser processing. The drilled hole should be smooth and straight. There should not be any exposed glass fibers in the hole, no extreme gouging, and no fracturing of the resin in the hole. As the boards are processed through the electroless and plating chemistries, the hole wall may be further degraded, and moisture may be allowed to wick into the board. This may also contribute to CFF failures.

3.5 Surface Finishes

For most parts, the functions of the surface finish are to prevent copper oxidation, facilitate solderability, and prevent defects during the assembly process. A number of metallic alternatives exist along with organic solderability preservatives (also known as OSPs or pre-fluxes). A variety of deposition techniques exist, including hot air leveling, electroplating, immersion, and electroless plating. The shelf life of immersion, electroless plated, and OSP coating alternatives are less than that of leveled or tin-lead reflowed boards. Other surface finishes are dictated by the environment in which the part will reside or by specific performance criteria. Solder-mask-over-bare-copper (SMOBC) with hot-air-solder-leveling (HASL) has been the preferred surface finish for over 15 years. Nickel-gold, another popular finish, can be applied electrolytically as an etch resist, replacing tin and tin-lead, or electrolessly as a substitute for HASL. Other electrolytic plating metals include rhodium, palladium, palladium-nickel alloys, and ruthenium. Non-electrolytic deposition processes include tin immersion, tin-lead displacement plating, electroless nickel, electroless gold, immersion gold, immersion silver, immersion bismuth, and the previously mentioned OSPs. The purpose of solder mask is to physically and electrically insulate those portions of the circuit to which no solder or soldering is required. Increasing density and surface mount technology have increased the need for solder mask to the point that, with the exception of "pads only" designs, nearly all parts require it. Manufacturers have had some autonomy in selecting masks. Many specifications do not call out a specific product or product type, allowing the manufacturer to choose masks based on processing as well as performance issues.

Three basic types of masks are commonly applied: thermally cured screen-printed masks, dry film, and liquid photoimageable (LPI). Thermal masks have predominated for decades but are gradually being replaced by LPI, despite being the lowest cost alternative. Dry film has some specific advantages, such as ease of application, but its use seems poised to decline as well in the face of improving LPI formulations.

The HASL process consists of a pre-clean, fluxing, hot air leveling, and a post-clean. Pre-cleaning is usually done with a micro-etch. However, the usual persulfate or peroxide micro-etch is not common in the process. Dilute ferric chloride or a hydrochloric-based chemistry is favored for compatibility with the fluxes that are applied in the next step.

Fluxes provide oxidation protection to the pre-cleaned surface and affect heat transfer during solder immersion. The fluxes also provide protection against oxidation during HASL (hot air solder level). Higher viscosity fluxes provide better oxidation protection and more uniform solder leveling, but reduce overall heat transfer and require a longer dwell time or higher temperature. A balance in flux use must be struck between better protection with high viscosity fluxes and superior heat transfer with lower viscosity fluxes.

All areas of exposed copper are coated with solder while masked areas remain solder-free. Boards are then cleaned in hot water, the only step in the SMOBC process where lead may enter the wastewater stream, in very small quantities. Once cleaned, the

panels may again enter the screening area for optional nomenclature screening, or proceed directly to the routing process.

Copper, flux, and other impurities increase in concentration in the solder pot as panels are continuously processed through the hot air leveler. These impurities can be removed to some degree by performing a procedure known as drossing. The impurities will float to the surface of the solder where they can be scooped out and placed in a dross bucket. This material can be returned to the vendor for reclamation of the metals. Some manufacturers go for years without changing the solder; they dross and make additions. When the time comes to change over the solder, vendors will issue credit on the purchase of new solder as long as the old solder is returned to them for processing. HASL temperatures and certain fluxes can also contribute to CFF failures. The high, temperatures may exceed the T_g of the material, and depending on the type of coating used, moisture uptake may be enhanced. Any residue left on the board may also be an issue.

3.6 Defects that may Initiate and Accelerate CFF Failures

During failure analysis conducted on defective PWBs, some of the manufacturing defects that can initiate and accelerate CFF failures were observed. Following the list of defects, are photos and descriptions representative of most:

- Fiber/resin separation (see Figure 4)
- Conductor/resin separation (see Figure 5)
- PTH/resin separation (see Figure 6)
- Degradation of conformal coating layer
- Mis-registration (see Figure 7)
- Copper wicking (see Figure 8)
- Drilling damage (see Figure 9)
- PTH plating cracks (see Figure 10)
- Hollow fibers (see Figure 11)

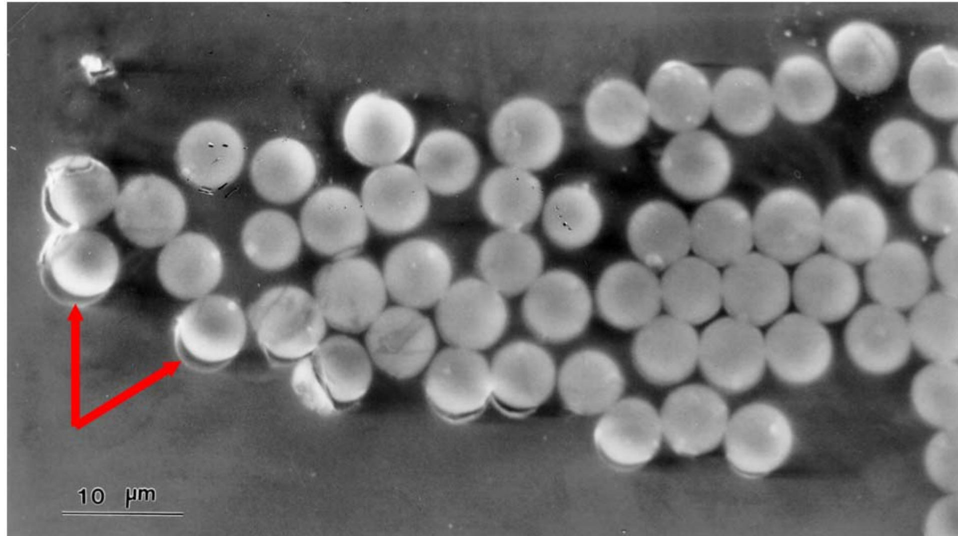

Figure 4. Fiber/resin interface delamination can occur as a result of stresses generated under thermal cycling due to a large CTE mismatch between the glass fiber and the epoxy resin (approximately 5.5 ppm/^{o}C and 65 ppm/^{o}C respectively) and poor bonding at the fiber/resin interface. Delamination can be prevented/resisted by selecting resin with lower CTE's and optimizing the glass surface finish. Studies have shown that the bond between fiber and resin is strongly dependent upon the fiber finish.

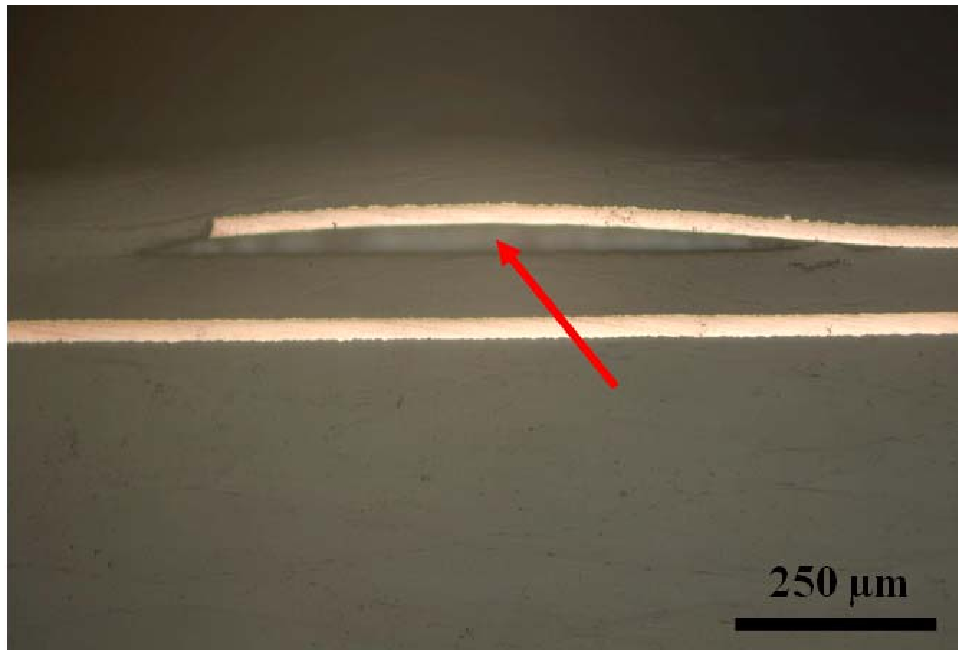

Figure 5. Moisture can condense in the copper/resin separated areas, allowing the copper to ionize, and migrate towards adjacent conductors.

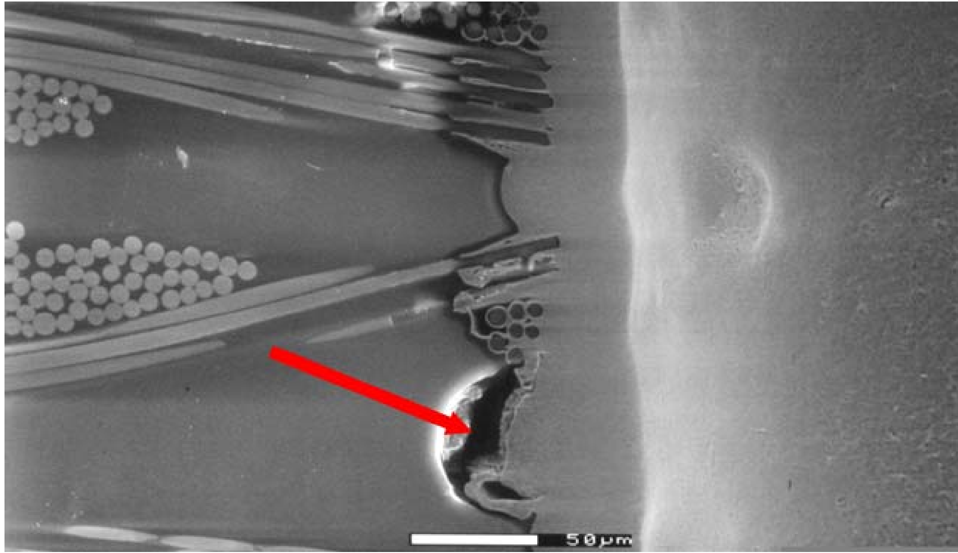

Figure 6. A separation can be seen at the copper plating to fiber epoxy resin board interface. These gaps provide areas for moisture to condense and CFF to initiate. These voids which can be adjacent to inner-layer copper foils or PTH barrels, normally result from contraction of the epoxy (resin recession).

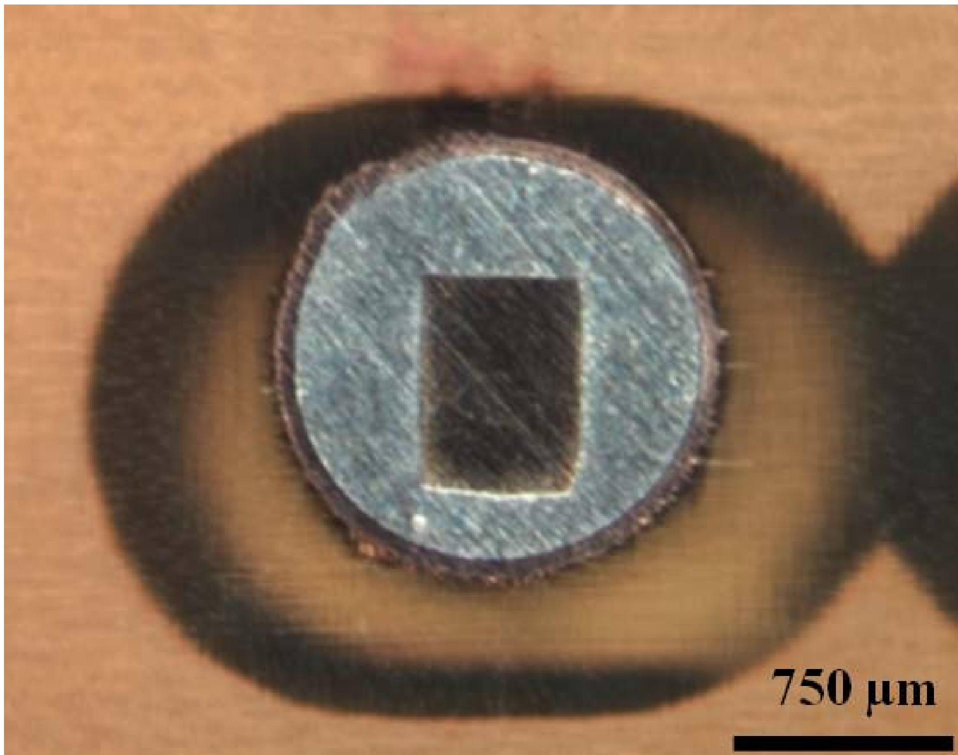

Figure 7. This optical image shows misregistration between a solder filled PTH and a power plane. Misregistration can decrease conductor spacing, effectively increasing the PWB's electric field strength in the closer conductor spacings.

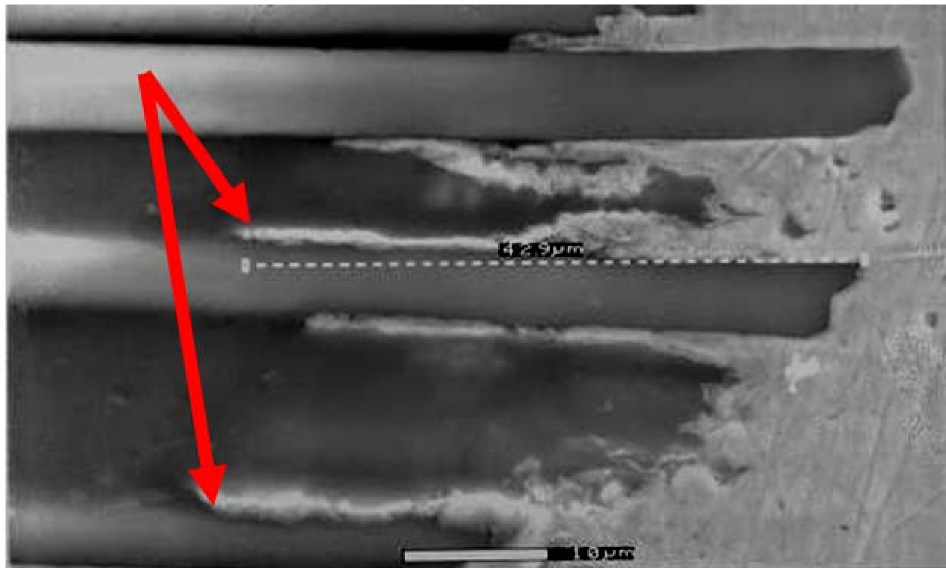

Figure 8. Copper wicking can be serious if it extends sufficiently to increase the electric field strength or decrease the internal resistance breakdown between PTHs. Furthermore, it provides a convenient starting point for CFF as it effectively decreases the conductor spacing.

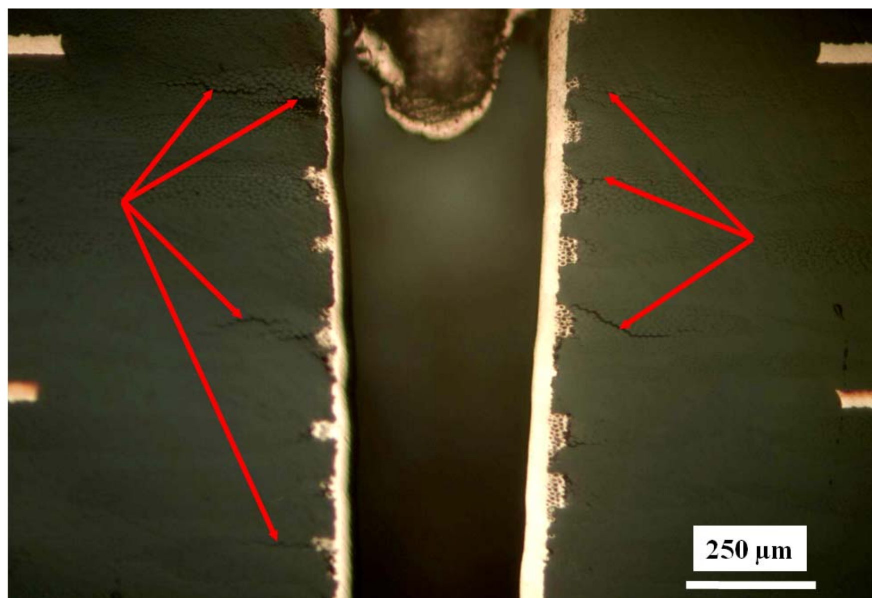

Figure 9. The anomalies seen around the PTH, known as micro-cracking, are primarily caused by excessive heat or mechanical loads due to non-optimized drilling parameters. Drilling has become a very complex process with regard to the selection of optimum drill parameters for high performance materials. New drill bit compositions and geometries are most important among these factors.

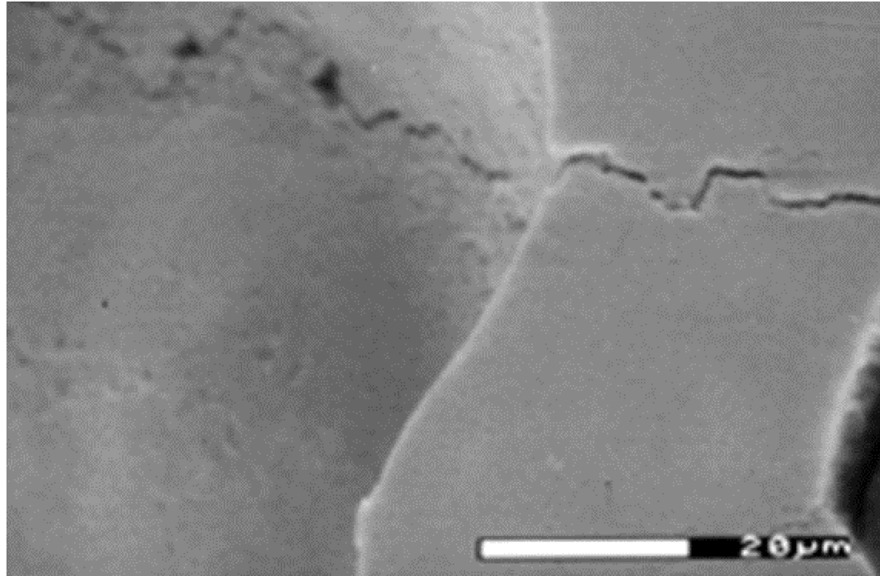

Figure 10. Since the difference in the coefficient of thermal expansion (CTE) of the copper plating and the resin system in the PWBs is at least a factor of 13, stress exerted on the plated copper in the plated-through holes in the z-axis during thermal excursions can cause cracking. These cracks provide areas for moisture to condense and for CFF to initiate.

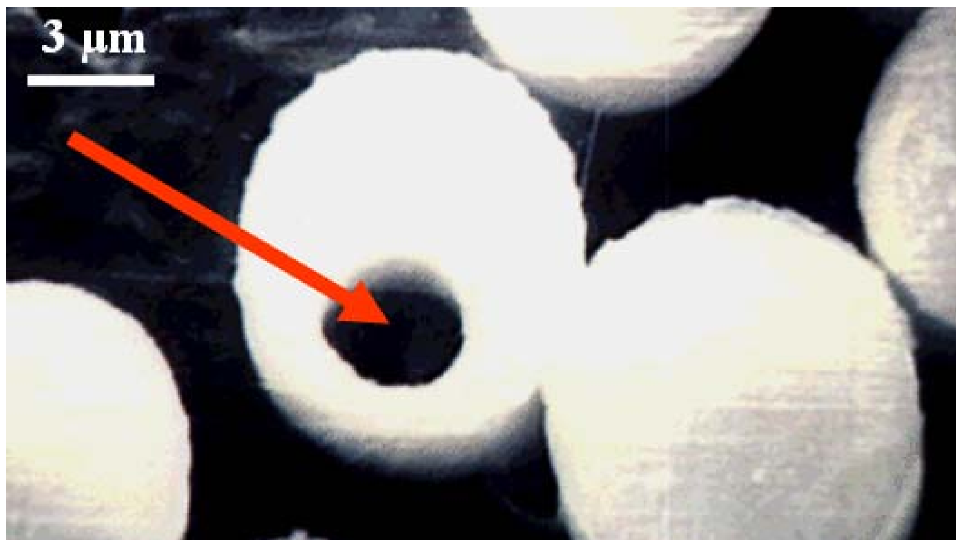

Figure 11: Hollow fibers are vacuous glass filaments in E-glass laminates which can provide paths for CFF. Generally CFF is a two-step process, dependent upon temperature-cycling or high temperature/humidity induced debonding between the glass fibers and epoxy resin matrix in providing a path for copper migration. With the appearance of hollow fibers inside the laminates, CFF can happen as a one step process.

3.7 Summary

This chapter provided a thorough review of the defects that may be introduced into a printed circuit board during the manufacturing process steps. While the presence of these defects is crucial to understanding the occurrence of certain filament driven failure phenomenon, classical theory states that the formation of a path in which the filament grows is the rate limiting step for this mechanism. These paths may be preexisting in the laminate because of the existence of hollow fibers or may develop as a function of applied external stresses on other defects. This dissertation provides the methodologies, specific for electronic products, for detecting hollow fibers and locating CFF related failures. The dissertation also provides experimental and analytical investigations of path formation in glass epoxy composites.

CHAPTER 4: HOLLOW FIBER DETECTION

4.1 Introduction

R.J.B. Hadden and A. Kirk, using a technique developed by the Fermi National Accelerator Laboratory, originally proved the existence of hollow fibers in glass fabrics. This technique has been modified to optimize the hollow fiber assessments. The following sections describe this process in detail. Hollow fiber assessment experiments show how hollow fiber densities can vary between different manufacturers and also within the same manufacturer based on the laminate type (e.g. high T_g versus low T_g). Some of the resin types assessed were polyimide (PI), bismaleimide triazine (BT), cyanate ester (CE), flame retardant (FR-4), a high-temperature FR-4, and Driclad, an IBM high T_g laminate advertised as having low moisture uptake.

4.2 Measurement Techniques for Hollow Fibers in Common Laminates

Laminates are cut along the diagonal into 10 x 10 cm test coupons to allow for ease of handling, sample preparation, and observation through an optical microscope (see Figure 12). Since the hollow fibers usually traverse the entire length of the laminate, cutting samples along the diagonal insures that each hollow fiber is accounted for only once. If the laminates are copper cladded, the copper can be removed by submerging the copper cladded laminates in aqua regia, a chemical solution of concentrated hydrochloric and nitric acid, for about 10 to 15 minutes. This is

performed in a fume hood, using the appropriate protection as necessary for working with hazardous chemicals (see Figure 13).

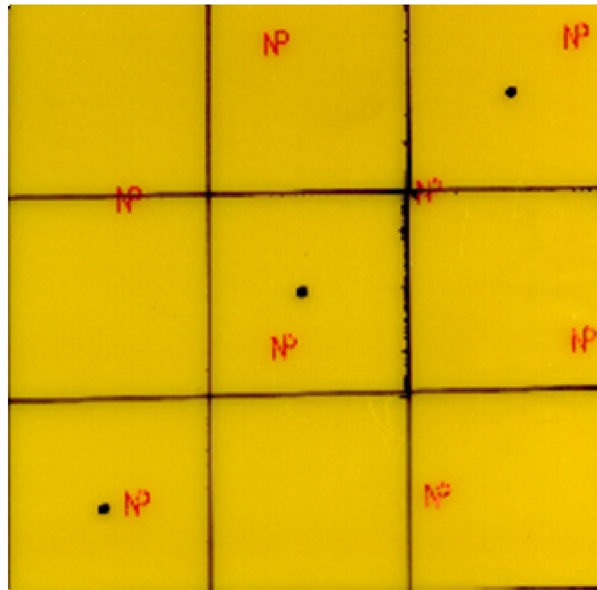

Figure 12. This photo shows the diagonal sections (black dot in middle) that are used for the hollow fiber assessments. By using only the sections on the diagonal, ensues that each hollow fiber is not accounted for more than once.

Figure 13. Placing the copper cladded laminates in a chemical solution of concentrated hydrochloric and nitric acid (aqua regia), for about 10 to 15 minutes, effectively removes all exposed copper from the surfaces. This is done in a fume hood, using the appropriate protection necessary for working with hazardous chemicals.

Samples are then placed in an oven at 538 ^oC (1000 ^oF) for approximately 60 to 90 minutes (depending on the resin type and laminate thickness) to burn off the resin and expose the bare glass bundle matrix (see Figure 14). The initial burn-off temperature of 600 ^oC, as suggested by industry, was found to result in the fracture of glass fibers during handling as they became brittle. By trial and error, a burn-off temperature of 538 ^oC was selected. This optimized the burn-off time while still maintaining the integrity of the glass fabric. After separating the individual fabric layers, each of the four sides for each individual fiber glass fabric layers was subsequently sealed with wax to prevent wicking, the capillary action of a fluid into a hollow fiber.

Figure 14. Photo showing before and after resin removal

The technique used by the Fermi National Accelerator Laboratory to investigate leaks in fiberglass-reinforced pressure vessels was employed to observe hollow glass fibers. Each fabric layer is submerged in oil with an optical refractive index that can be either similar to or slightly different (± 0.002) than that of the glass fibers and allowed to sit overnight (this allows the oil to completely saturate the fiber mat). Light is then directed onto the coupon, now saturated with the refracting oil. The light travels

freely until it hits a hollow fiber, where the change in refractive index at the fiber-air boundary partially reflects it. The unreflected light continues to propagate until it hits the outgoing air-fiber boundary, where again it is partially reflected (see Figure 15). Using a black background can improve the visibility of the hollow fibers. The hollow fiber detection setup is shown in Figure 16. Even though hollow fibers are visible to the naked eye, a low magnification microscope attachment is best to view them (see Figure 17). While each of the methods (oil with an optical refractive index that can be either similar to or slightly different than that of the glass fibers) provides a means to optically view the hollow fibers, using an oil with the same refractive index as the glass fibers allows only the hollow fibers to be seen, whereas, using an oil with a slightly different refractive allows not only the hollow fibers to be seen, but also faintly shows the glass fabric weave. This method can produce an image of the glass fiber fabric and the hollow fibers simultaneously. Both oils, with the equal refractive index, (see Figure 18) and with the slightly different refractive index (see Figure 19) are shown. The oil with the slightly different refractive index is preferred, since both the hollow fibers along with the fabric weave can be viewed simultaneously. The refractive index of E-glass is 1.550, while that of the oil (Tricresyl Phosphate) is 1.553, giving a difference of 0.003.

In one experiment, the number of hollow fibers observed in several 2 x 2 inch coupons ranged from 0 to 158. Six to eight samples were tested for each laminate type. The IBM Driclad laminate, promoted as “hollow-free fabric” to prevent conductive filament formation (CFF), had an average of 16 hollow fibers/1,000 in^2.

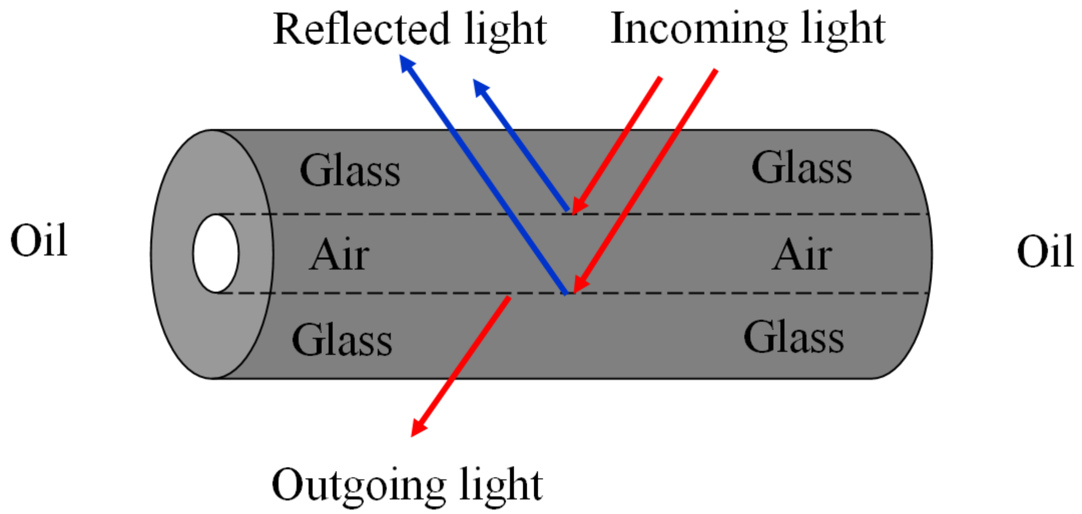

Figure 15. Light travels freely until it hits a hollow fiber. The change in the refractive index at the fiber/air boundary partially reflects the light.

Figure 16. A change in the refractive properties is evident through an optical microscope by a bright white line. In some cases, a hollow fiber could be detected without using a microscope. The light source is positioned so that light enters the edge of the fabric perpendicular to the fibers being observed.

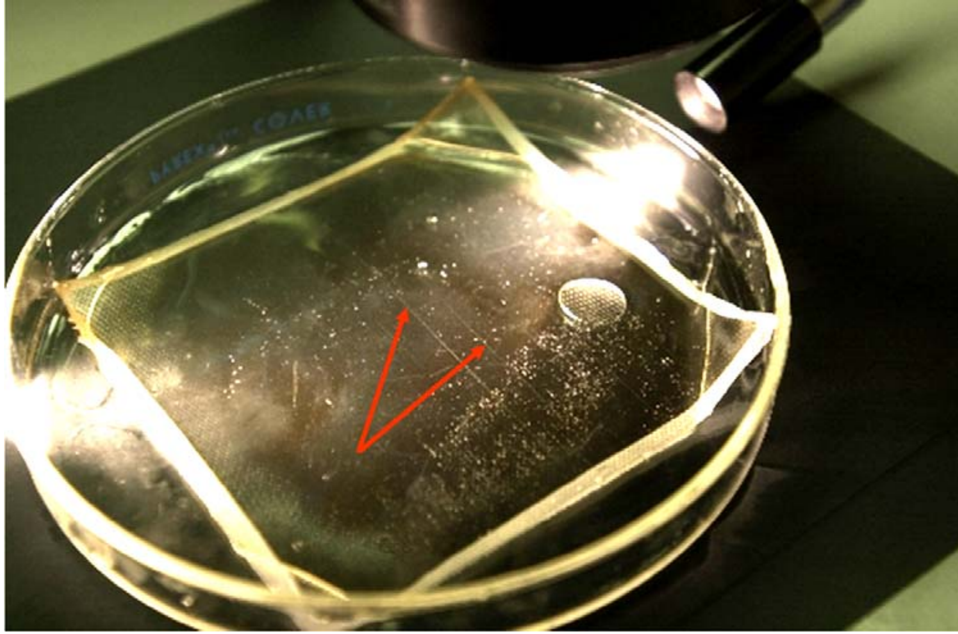

Figure 17. Although hollow fibers are visible to the naked eye (see arrows), a microscope attachment is best to view them.

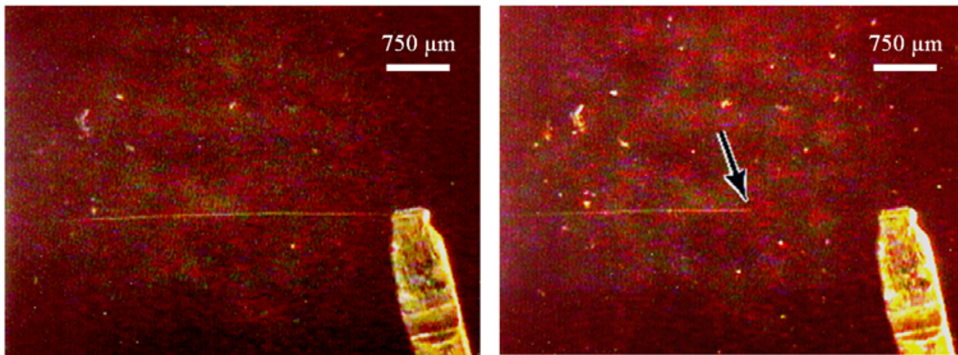

Figure 18. The edges of this sample were not dipped in wax. As the sample was submerged in oil, the oil started to flow into one of the hollow fibers. A mark was set at one point of the hollow fiber so that the movement of the oil could be more easily visualized. Only the hollow fiber is visible, due to the exact match between the refractive index of the oil and the fiber glass.

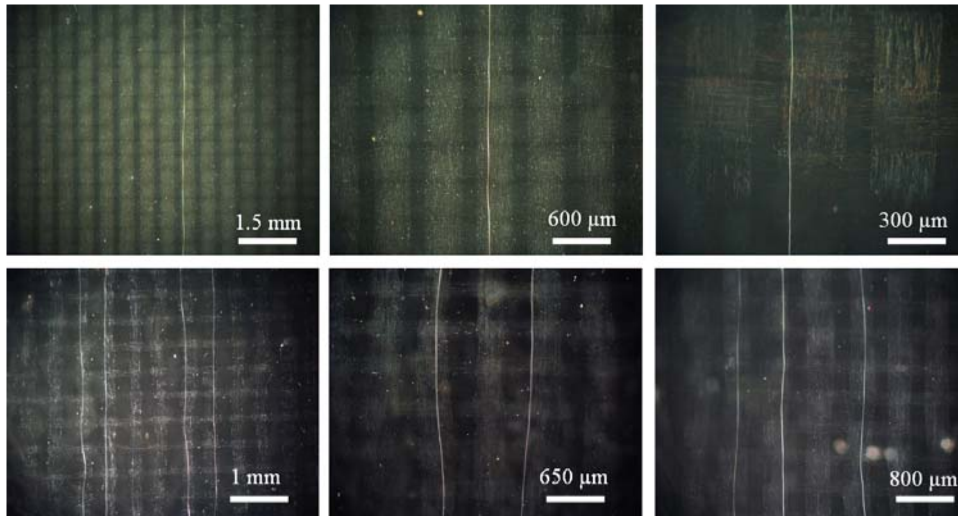

Figure 19. Hollow fibers can be seen as white lines traveling along the fiber bundle weave in these pictures. The refractive index of E-glass is 1.550, while that of the oil used here is 1.553. This difference of 0.003, allows the fabric weave to also be seen.

4.3 Discussion of the Hollow Glass Fiber Problem

Multi-layer organic laminates used in printed wiring boards and laminated multichip modules (MCM-L) can develop a loss of insulation resistance between two biased conductors due to the growth of conductive filaments. The phenomenon, called conductive filament formation (CFF) or electromigration, is an electrochemical process which involves the transport, usually ionically, of a metal through or across a nonmetallic medium under the influence of an applied electric field. The growth of metallic filaments is a function of temperature, humidity, voltage, laminate materials, manufacturing processes, and the geometry and spacing of the conductors.

CFF is most prone to occur between biased conductor such as vias and plated-through holes (PTHs), but can also occur between two traces (usually copper) or between a trace and a via or PTH [Rudra and Pecht 1994]. The formation of a continuous

metallic path through or on the outside of the fiber can result in an electrical short. Hollow fibers are vacuous glass filaments in E-glass laminates which can provide paths for conductive filament formation (CFF). Generally, CFF is a two-step process, dependent upon temperature-cycling and/or humidity-cycling induced debonding between the glass fibers and epoxy resin matrix to provide a path for copper migration. With the appearance of hollow fibers inside the laminates, CFF can happen as a one step process. A photo of a partially copper-filled hollow fiber bridging and electrically shorting two adjacent PTHs in a PWB is shown in Figure 20. CFF is nearly impossible to detect in the field because once it occurs, sufficient heat is generated to "vaporize" the conductive filament and "clear" the failure. Furthermore, observation of a partial filament formation requires destructive analysis. It is nearly impossible to screen a circuit card in order to precipitate CFF, in part because of the ability of the problem to heal itself.

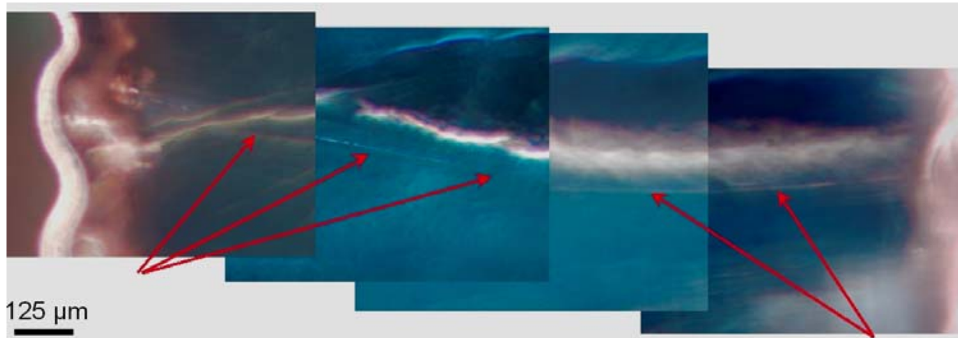

Figure 20. Hollow fibers are vacuous glass filaments in E-glass laminates which can provide paths for conductive filament formation (CFF). Generally CFF is a two-step process, dependent upon temperature-cycling and humidity-cycling induced debonding between the glass fibers and epoxy resin matrix to provide a path for copper migration. With the appearance of hollow fibers inside the laminates, CFF can happen as a one step process.

4.4 Failure Opportunities due to Hollow Fibers

Research has shown that PTH-to-PTH CFF failures represent the most significant population of failure opportunities, especially compared with line-to-line or line-to-PTH metallization failures [9, 10]. Thus, PTH-to-PTH adjacency is a suitable measure of hollow fiber failure opportunity. CFF failure opportunity is proportional to the probability of a hollow fiber connecting two adjacent plated-through-holes (PTHs). This probability is proportional to the density of PTHs in the circuit card, the number of fibers that the PTHs are in intimate contact with (PTH diameter vs. grid spacing, see Figure 21), and the hollow fiber density of the circuit card.

The PTH density depends on the circuit card layout design rules and the allowable exceptions. The number of fibers that each PTH is in intimate contact with depends on PTH diameter, fabric style (number of bundles/square inch, number of individual fibers/bundle), and the thickness of the board (number of laminate layers and individual glass fabric mats). An E-SEM photo of a cross-sectioned area in a woven laminated printed circuit board containing two PTHs is shown in Figure 22.

To make the calculations easier to follow, assume that each PTH runs through the entire thickness of the board (i.e., no blind or buried PTHs are considered) and that each PTH has the same diameter. To accommodate for blind or buried PTHs, or PTHs of differing diameters, changes in the total number of filaments that are in contact with PTHs can be adjusted based on changes in PTH dimensions.

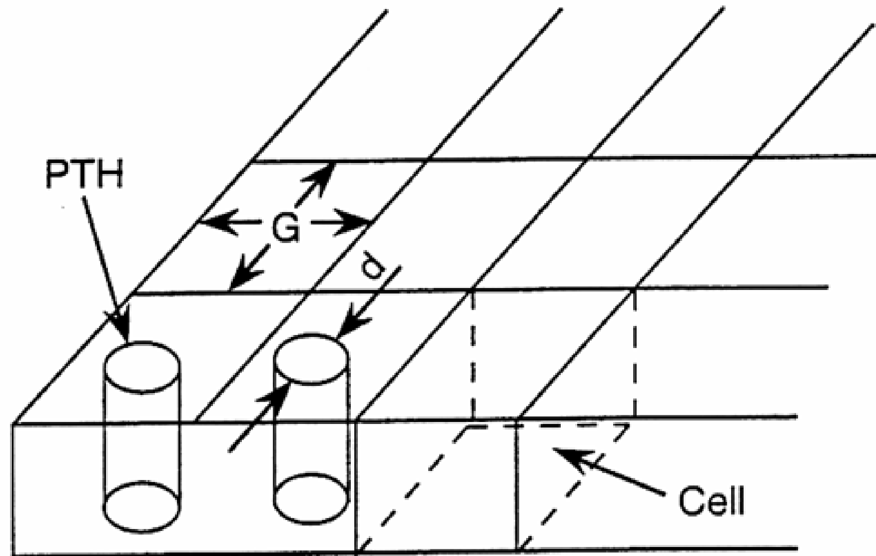

Figure 21. This drawing shows the PTH grid, PTH diameter (d) and the planar surface dimensions of each cell (G x G) in the PTH grid.

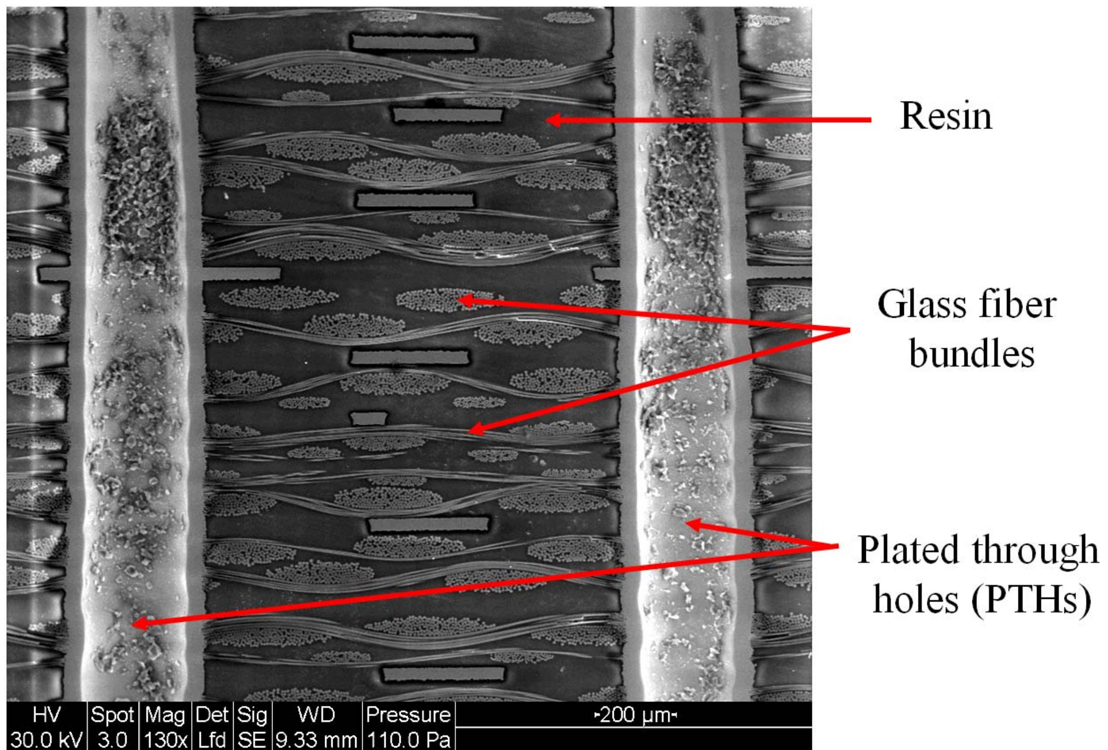

Figure 22. This E-SEM photo shows a cross-section of a printed circuit board containing two PTHs, resin and woven fiber glass.

For a given hollow fiber ratio, the failure opportunity or unreliability, Q_C, can be determined by:

$$Q_c = 1 - \{1 - [hollow\ fiber\ ratio\ (d/G)]\}^p \qquad (14)$$

where d/G is the ratio of the PTH diameter to the grid length and p is the number of possible failure sites.

Given an acceptable Q_C, the maximum allowable hollow fiber ratio can be calculated by rearranging equation 14 to obtain:

$$hollow\ fiber\ ratio = \left[1 - (1 - Q_c)^{\frac{1}{p}}\right] \cdot \frac{G}{d} \qquad (15)$$

To obtain a reliability of 99.9% (Q_C = 0.001) in a typical 6 layer PWB, using a 7628 glass style (plain weave with 44 x 32 bundles/inch), with a PTH in-line grid of 37 rows x 69 columns (p = 5000, see Figure 23), and a PTH diameter/grid length = 40%, if this grid is within a 2.8 in x 5.2 in area, there are approximately 290 fiber bundles per fabric layer [2.8 (44) + 5.2 (32) = 290]. Five laminates with 6 fabric layers each, gives 30 fabric layers or 8,700 fiber bundles. Since each fiber bundle contains 204 individual glass filaments, there are 1,774,800 glass filaments in this PWB section. Using equation 15 yields a hollow fiber ratio of 5E-7. For the 1,774,800 glass filaments, this translates to 0.89 or no more than 1 hollow fiber / 2.8 in x 5.2 in area, as obtained from Equation 16.

$$5E^{-7} = \frac{x}{1774800} \qquad (16)$$

Solving for *x* gives 0.89. Therefore, in a typical board with these specifications, there must be less than 1 hollow fiber per 2.8 in x 5.2 in area in the board, to have a failure opportunity less than 0.001, due to filament formation between adjacent PTHs through a hollow fiber. These calculations assume that conditions are conducive for CFF. For different conductor geometries or PWB thickness, the allowable hollow fiber ratio, based on an acceptable reliability, can be recalculated.

On the Fujitsu M-780 large-scale general purpose computer, there are more than 80,000 PTHs per circuit card. A section of a PWB containing over 6,000 PTHs is shown in Figure 24.

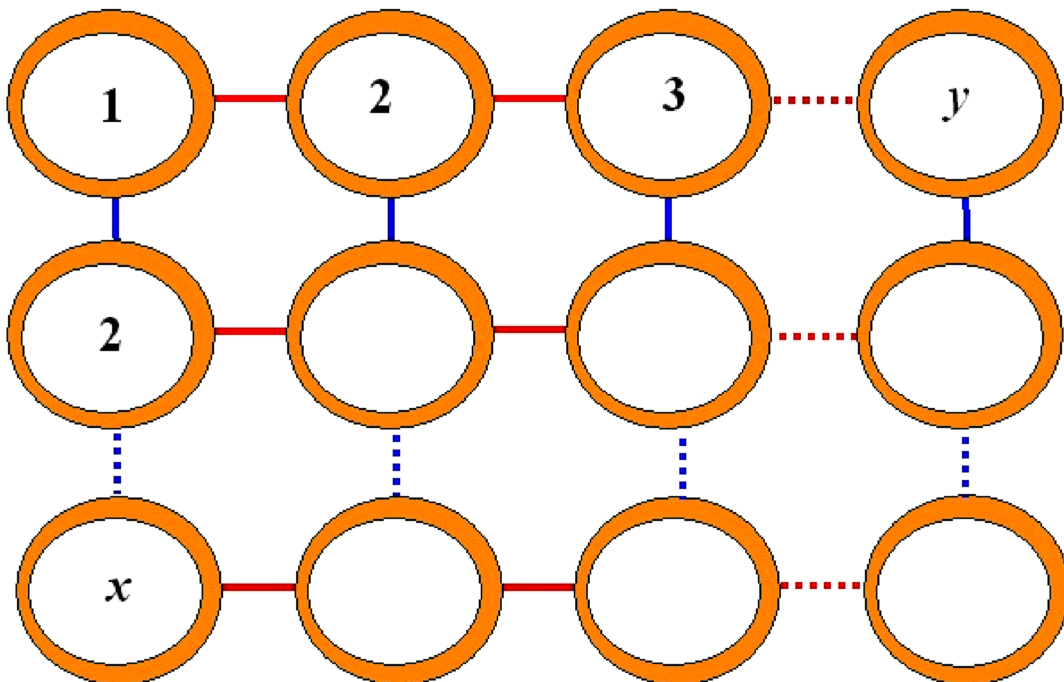

Figure 23. For a 37 x 69 grid of PTHs, where x = 37 PTH rows and y = 69 columns in the grid, the number of possible adjacent PTH failure sites can be calculated by: (37+68)(69+36) = 5,000 possible failure sites. In a square grid, where x = y, this simplifies to $2[x(x-1)]$ or $\sim 2x^2$ for x > 100.

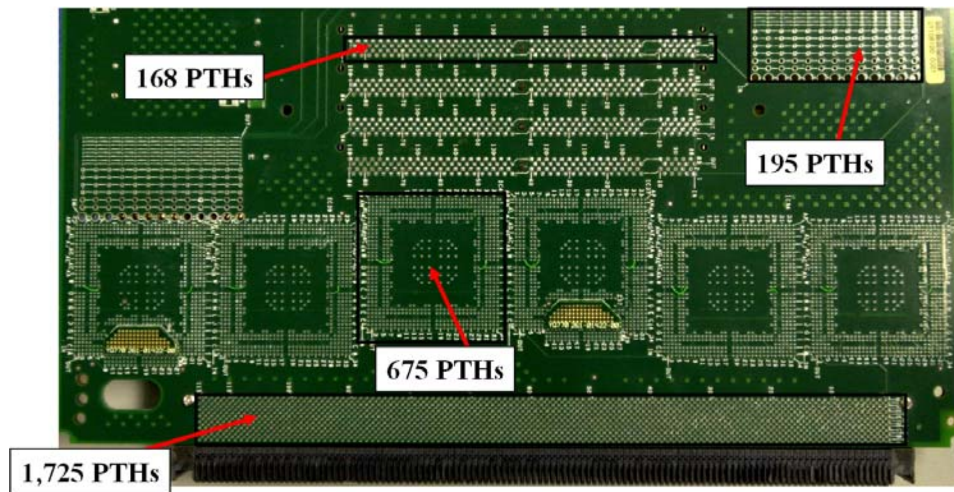

Figure 24. This PWB section (half of board used by AVICI Systems) contains close to 7,000 PTHs. On the Fujitsu M-780 large-scale general purpose computer, there are more than 80,000 PTHs per circuit card.

CHAPTER 5: ANALYZING CAF FAILURES

There are basically three methods for detecting and locating CAF failures; electrical testing, thermal imaging and superconducting quantum interference device (SQUID). Each technique is unique, and in some situations may be the only available choice to verify that a failure exists and locate the failure site. After the failure is verified and the site identified, cross-sectional techniques can be employed to allow microscopic examinations and elemental analysis of the defective area.

5.1 Electrical Testing

In cases where the shorted conductors can be traced via circuit schematics, and no ground or power planes are involved in the shorted site, electrical probing may be a viable technique for locating the defective site via resistance checking (see Figure 25). In this technique, the approximate resistance values between conductors based on the circuit design should be available to verify locations where low resistance values can be attributed to defects and not to design. It is important to isolate the suspected shorted conductors from the rest of the circuit, and verify that no superficial anomaly such as surface contamination or debris is contributing to the low resistance value observed (i.e., the shorted site is internal). For complex circuitry where it is not possible to isolate the suspected conductors, electrical testing may be of lesser value. After verification of the failure, subsequent cross-sectional techniques, while continuously monitoring the resistance of the shorted conductors, may resolve the precise failure site and uncover defects that may have initiated or accelerated the failure, by optical and E-SEM inspections.

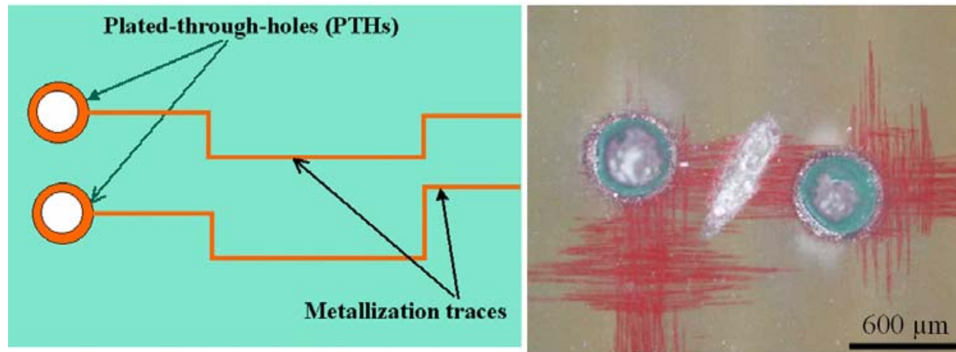

Figure 25. Conductor geometry of shorted adjacent PTHs where electrical testing may be used to verify the existence of an internal short in a PWB, after isolation from the rest of the circuitry (removal of the surface traces) is shown.

5.2 Thermal Imaging

Thermal imaging is technique that has been successfully used to locate shorted locations by monitoring the changes in temperature as a defective board is powered. When power is applied to the defective board, a higher than normal current flows through the shorted conductors, and can cause a localized temperature rise in the affected area. A suitable level of current, which is high enough to cause a rise in temperature at the localized shorted site, while at the same time not destroying or "blowing" the fragile fuse-like filament, must be obtainable. If this suitable level of current can be obtained, and the equipment is sensitive enough to detect minute temperature rises, this technique can overcome disadvantages such as complex circuitry and shorts involving conductor planes, which limit electrical testing. However, due to the nature of the conductive filaments, many of them are fragile, and the current necessary to cause a detectable temperature rise in the shorted site can destroy them. One successful analysis using thermal imaging to verify and locate a short involving a ground plane can be seen in Figure 26 where the hot spot is

identified, and the short between the PTH and ground plane found by subsequent cross-sectional techniques (see Figure 27).

Figure 26. The photo at the top shows the thermal imaging equipment, while the photo at the bottom shows a sequential series of snapshots (clockwise starting at top left) as the power is turned on, identifying the shorted area.

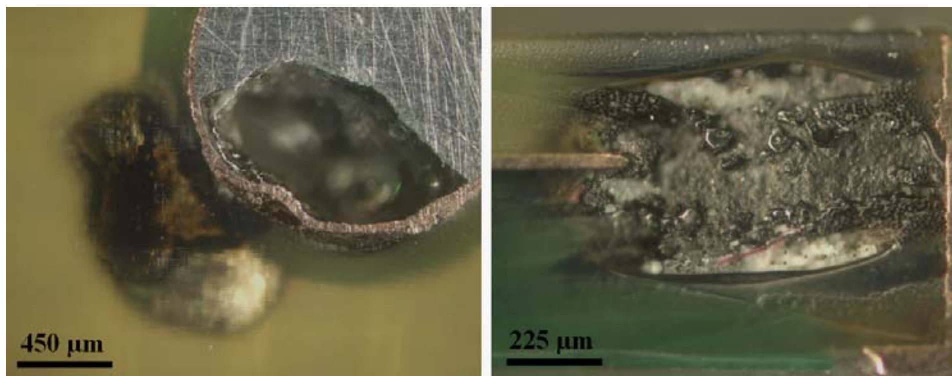

Figure 27. After locating the defective area by thermal imaging, subsequent cross-sectional techniques verified that there was an internal short between a PTH and ground plane.

5.3 Superconducting Quantum Interference Device

Superconducting quantum interferance device (SQUID) microscopy is a new technique that uses detection of magnetic fields to image current paths within electronic devices (see Figure 28). This technique has been successful in non-destructively identifying the location of low leakage currents, even when the failure site was between a power and ground plane (roughly equivalent to finding a needle in a haystack). The use of low voltage and low current can be superior to thermal imaging. Thermal imaging can result in irreplaceable damage to the failure site and masking of the true root cause of failure when a high amount of current is required to generate sufficient heat to be detectable. A photo of the current mapping output from the SQUID is shown in Figure 29. The shorted site, bridging two copper planes, was located after cross-sectioning, based on the SQUID results (see Figure 29 and Figure 30.

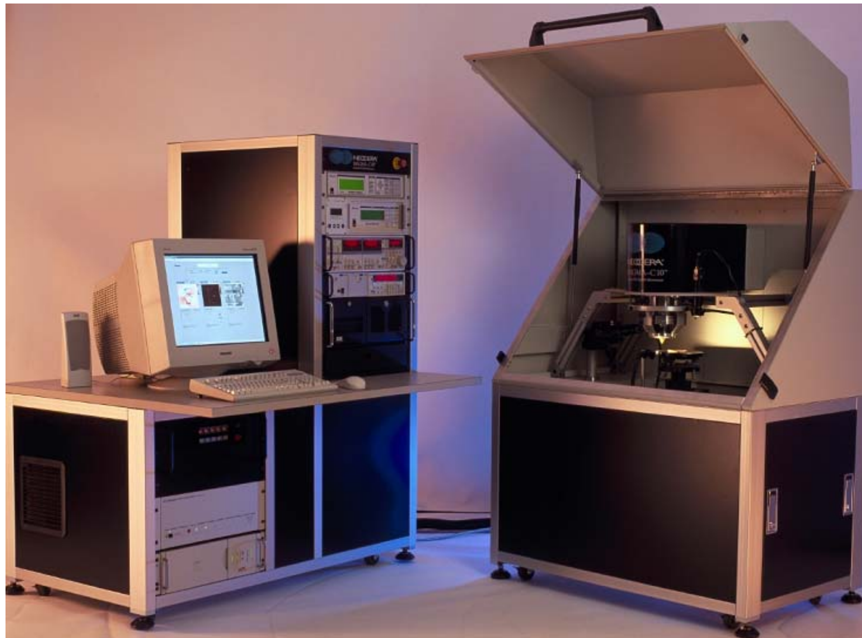

Figure 28. Photo of the superconducting quantum interference device equipment

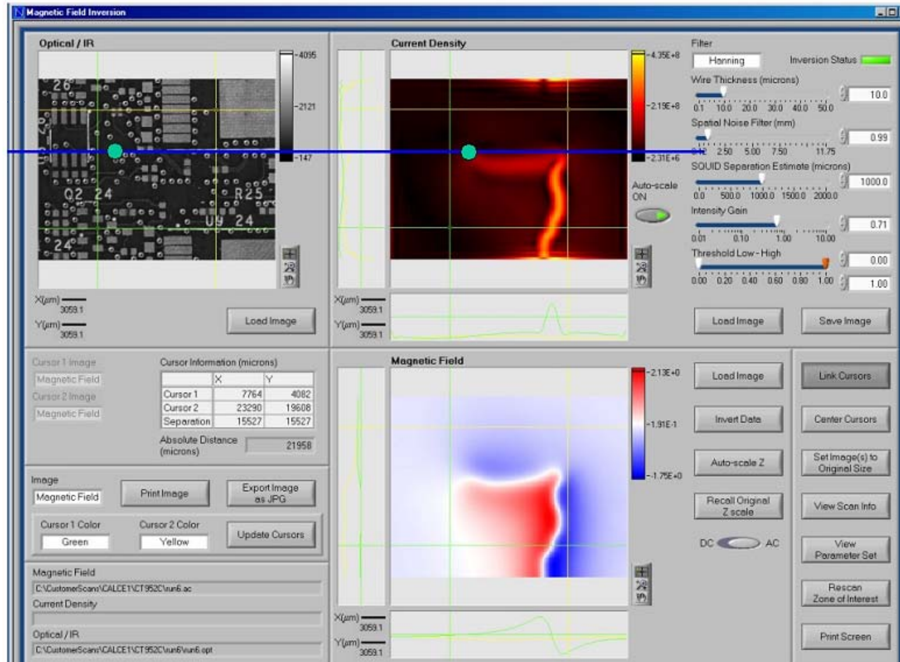

Figure 29. SQUID current mapping technique used to locate short circuit between planes in a PWB

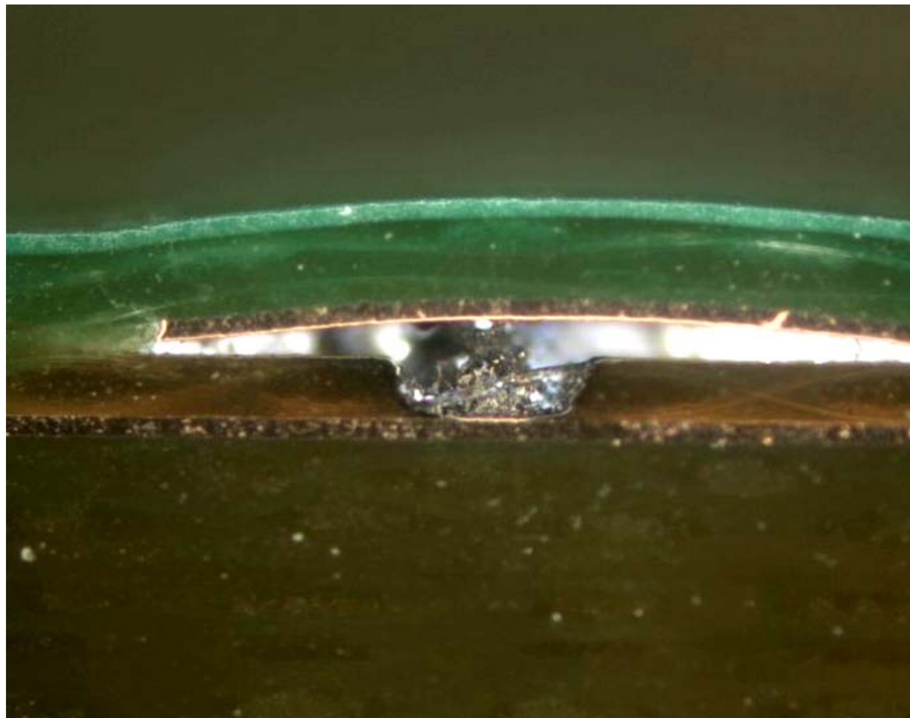

Figure 30. An optical image shows the shorted site located between two planes, after cross-sectioning based on the SQUID results.

Although the SQUID has unique advantages, it also has limitations. In addition to being costly, the SQUID it is limited to ~ 100 μm maximum working distance above the shorted site. Due to this, the SQUID may not be applicable to populated areas on a PWB where the height of components or connectors over the failed location can interfere with the working distance restrictions. For example, the SQUID could not have been used in the previous thermal analysis, due to the height of the connectors on the board.

Since the test boards in this dissertation are unpopulated, and the conductive filaments formed are fragile, the SQUID was used in verifying and locating the shorted sites.

CHAPTER 6: CFF EXPERIMENTS

Accelerated tests to characterize conductive filament formation failure behavior in laminated printed wiring boards subjected to high temperature and high humidity environments were conducted, using four laminate types, three conductor spacings and voltages ranging from 1 volt to 100 volts DC.

6.1 Test Board Design

Based on a literature review of the current test methods (IPC-TM-650 2.6.25, Telcordia GR-78 and Sun Micro Systems) and test board designs, parameters for the test coupons were selected. The design of the test boards used in this study is shown in Figure 31.

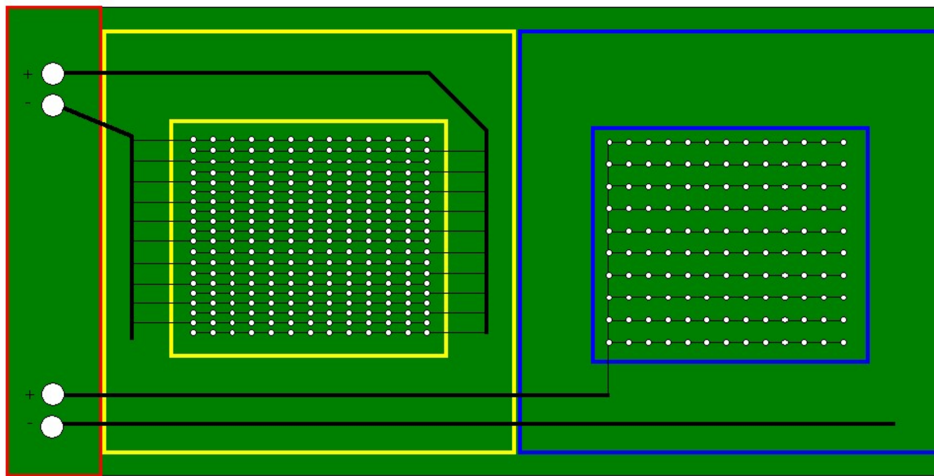

Figure 31. Design of the CFF test board used in this study

The IPC-TM-650 test board has 840 in-line PTH-PTH and 744 staggered PTH-PTH, the previous CFF testing conducted by Rudra et al. [1994] had 412 in-line PTH-PTH in the test board, and a board used by NPL [2004], contained over 6,000 PTHs. The PTH-PTH spacings previously used were, 11-25 mils edge-to-edge (IPC-TM-650), 5-

65 mils (Rudra, 1994) and 12-32 mils edge-to-edge (NPL, 2004), while the PTH-internal plane (aka anti-pad) spacings were 10-24 mils (IPC-TM-650), 10-20 mils (Rudra, 1994) and 16 mils: PTH wall – plane and 6-10 mils PTH pads – plane (NPL, 2004).

For this study, the test board design contains 600 in-line PTH-PTH and 100 PTH-plane conductors, with PTH-PTH spacings and PTH-internal plane spacings based on current technology and manufacturing limitations (see Figure 32). The three different feature sizes in both conductor geometries (PTH-PTH and PTH-plane) were selected to be representative of nominal, advanced and next generation feature sizes in electronics. The nomenclature of the three designs and conductor feature sizes were:

- Nominal (NF): PTH-to-PTH = 6 mil, PTH-plane = 8 ± 1 mil,
- Advanced (AF): PTH-to-PTH = 4 mil, PTH-plane = 6 ± 1 mil, and
- Next generation (XG): PTH-to-PTH = 3 mil, PTH-plane = 3 ± 1 mil

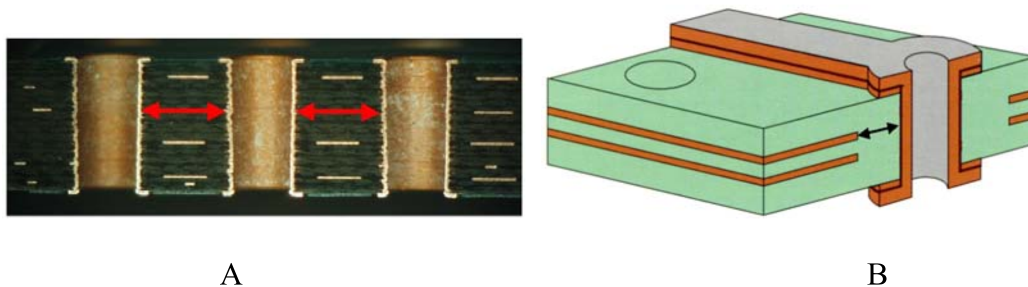

A B

Figure 32. The photos in A and B give examples of the PTH-PTH and PTH-plane conductor geometry features respectively.

Four different laminate types from two laminate suppliers were used for the fabrication of the 71 mil thick, 8-layer board (6 internal planes). Since CFF susceptibility can be affected by fabric weave direction (failures tend to occur earlier across the machine direction), the boards were tested for failure along the machine direction. The four laminate types from the two suppliers were:

- Isola FR-408 (T_g = 180ºC),
- Isola FR-406 (T_g = 170ºC,
- NanYa Plastics High T_g (T_g = 170ºC) and
- NanYa Plastics Halogen Free (T_g = 150ºC)

There were five samples for each spacing design and laminate type. The internal stack-up of the board consisted of three fabric weave styles as shown in the optical photo in Figure 33, while the test board manufactured by Gold Circuit Electronics is shown in Figure 34

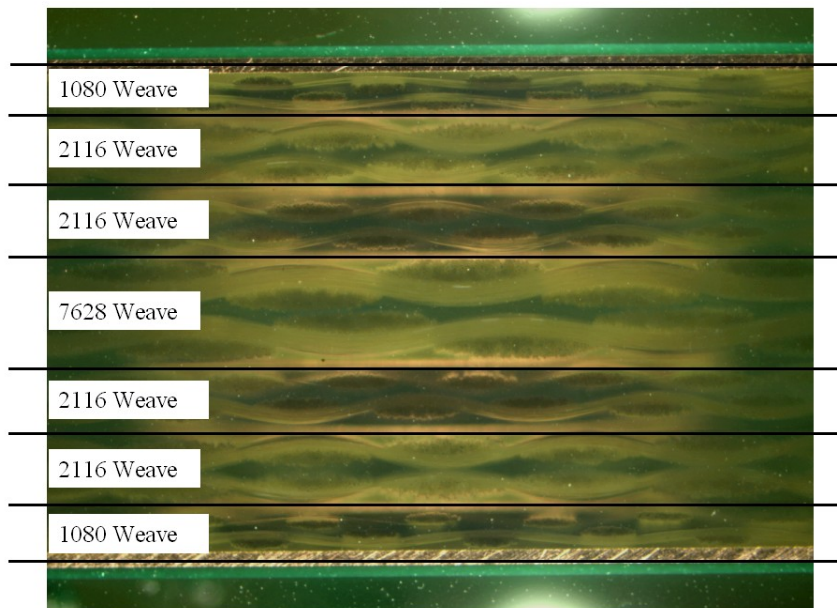

Figure 33. Optical dark field photo showing a cross-section of the test board's internal layer stack up

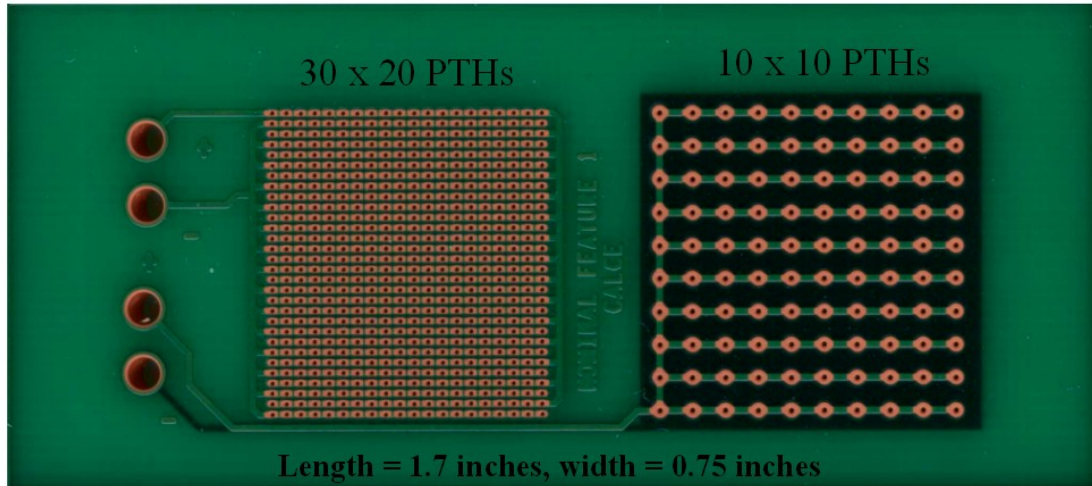

Figure 34. Photo shows the test board with the PTH-PTH grid (left) and the PTH-internal plane (right) test patterns.

6.2 Test Procedure

The boards were tested in accordance with IPC-TM-650 2.6.25, Conductive Anodic Filament (CAF) Resistance Test: X-Y Axis [18]. Each board was uniquely identified with a permanent marker, making marks away from the biased areas of the specimens. The test boards were handled by the edges only, using non-contaminating gloves. Each of the two circuits in each test board was prescreened for short circuits by performing an as-received insulation resistance measurement check. To dry out the samples, the selected boards were baked for six hours at 105°C prior to each test. For the preconditioning, the samples, after baking were allowed to sit in a bias free state for 24 hours at 23°C and 50% RH. The insulation resistances were again measured prior to a 96-hour stabilization period with no applied bias, at 85°C/85% RH. After this stabilization period, the selected bias was applied and insulation resistance measurements were started. All insulation resistance readings prior to the biased test were made with a FLUKE 189 True-rms Digital Multimeter (resistance range of 0 to 500 Mega-ohms). Prior to all tests, the measured insulation resistance of both test

circuits in each board was greater than 500 Mega-ohms. In the chamber, the boards were setup so that the air-flow was parallel to the direction of the test boards. The boards were also spaced approximately 2 inched apart (see Figure 35).

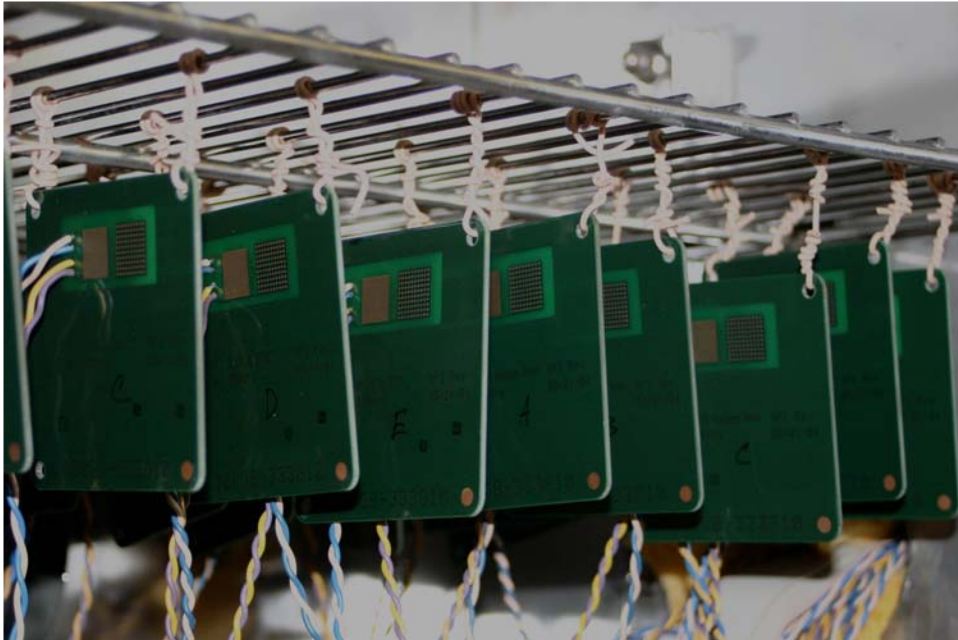

Figure 35. Photo of the boards hanging in the environmental chamber, parallel to the air flow and spaced approximately 2 inches apart.

The temperature and humidity of the chamber were monitored and plotted so that deviations from the set conditions could be observed (see Figure 36).

6.3 Insulation Resistance Monitoring Equipment

To monitor the insulation resistance of the boards as they were subjected to the humidity/temperature/bias testing, an Agilent 4349B High Resistance Meter was used in conjunction with power supplies, an interface box, an Agilent E5250A Multiplexer, a universal serial bus (USB) connected to a general-purpose interface bus (GPIB) and then to a computer. A schematic block diagram of the setup is shown in Figure 37

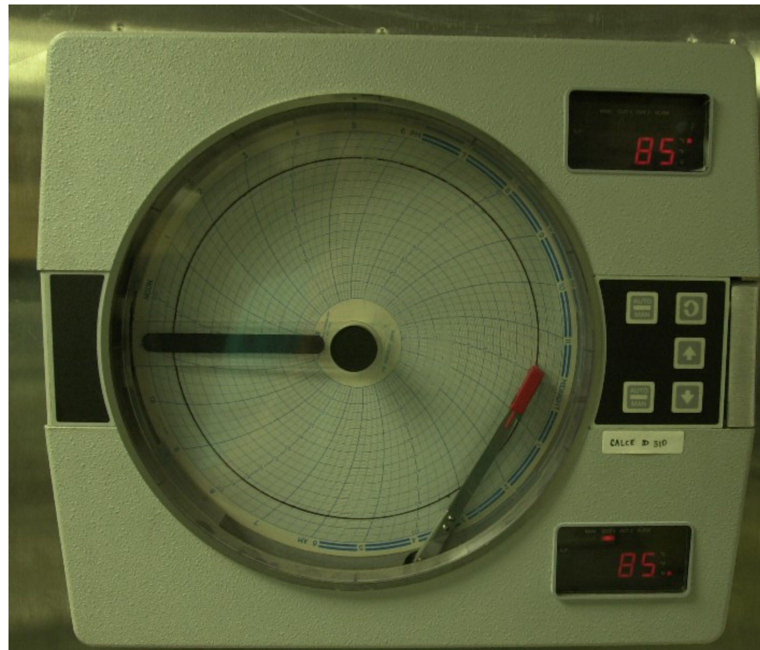

Figure 36. Monitoring and plotting system used to check variations in temperature and humidity settings

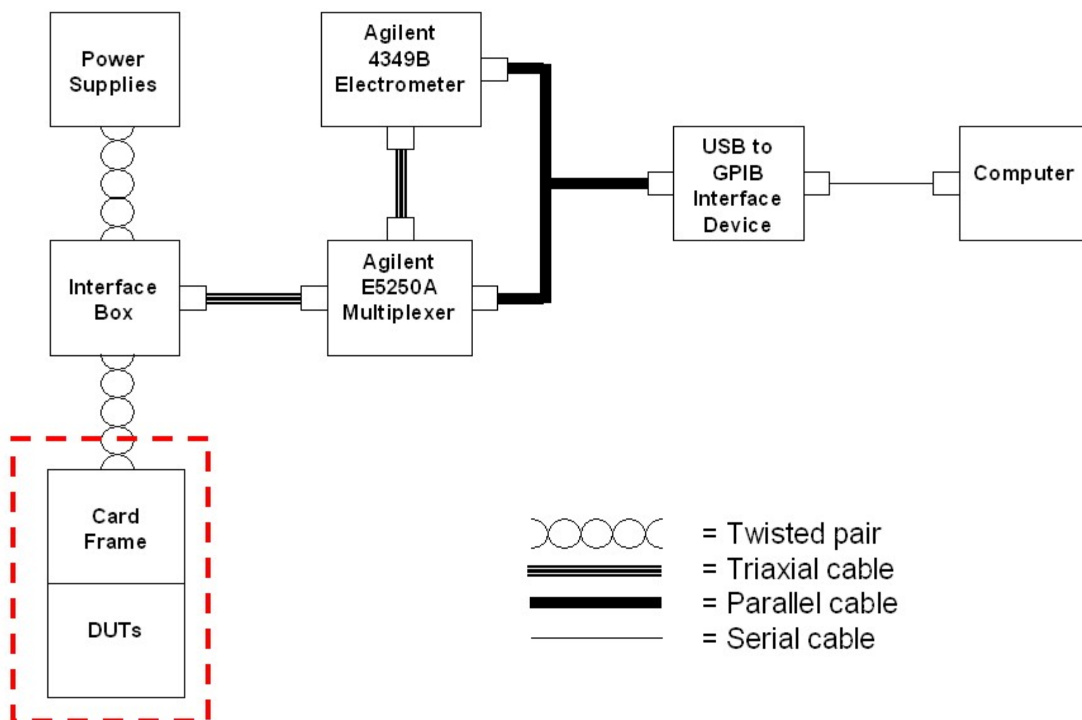

Figure 37. Block diagram of equipment setup to monitor insulation resistance

The different cable types and twisted wire pairs were used to minimize interference and noise. The system can accept 3 different voltage inputs and monitors 48 channels.

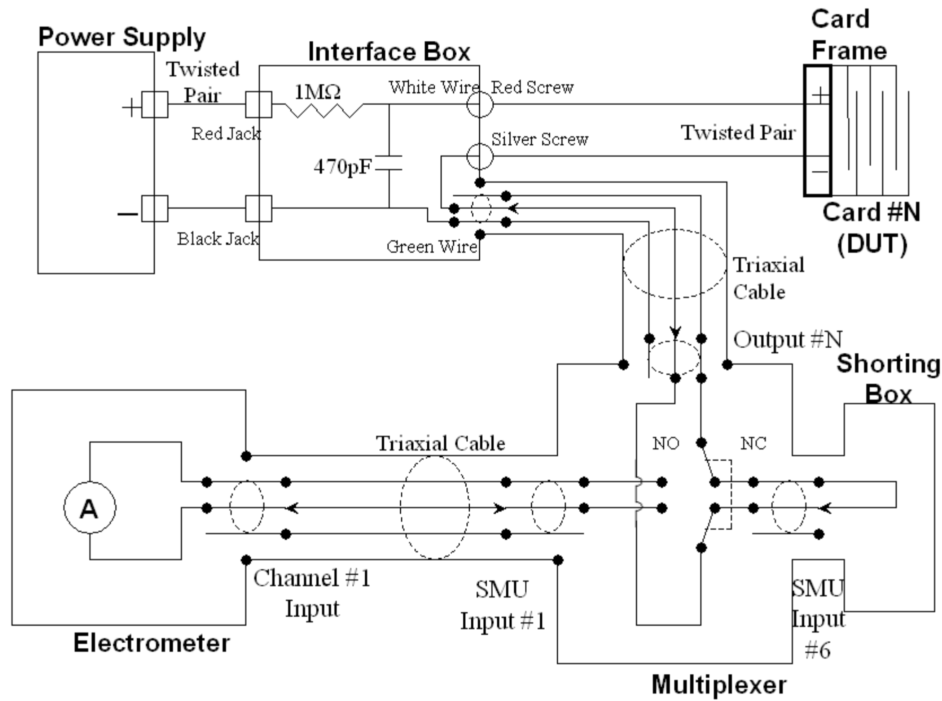

Figure 38. Schematic of the electrical circuitry used for monitoring the insulation resistance

A schematic of the electrical monitoring circuitry is shown in Figure 38 while the normal current path, and the current path during device monitoring are shown in Figure 39 and Figure 40 respectively.

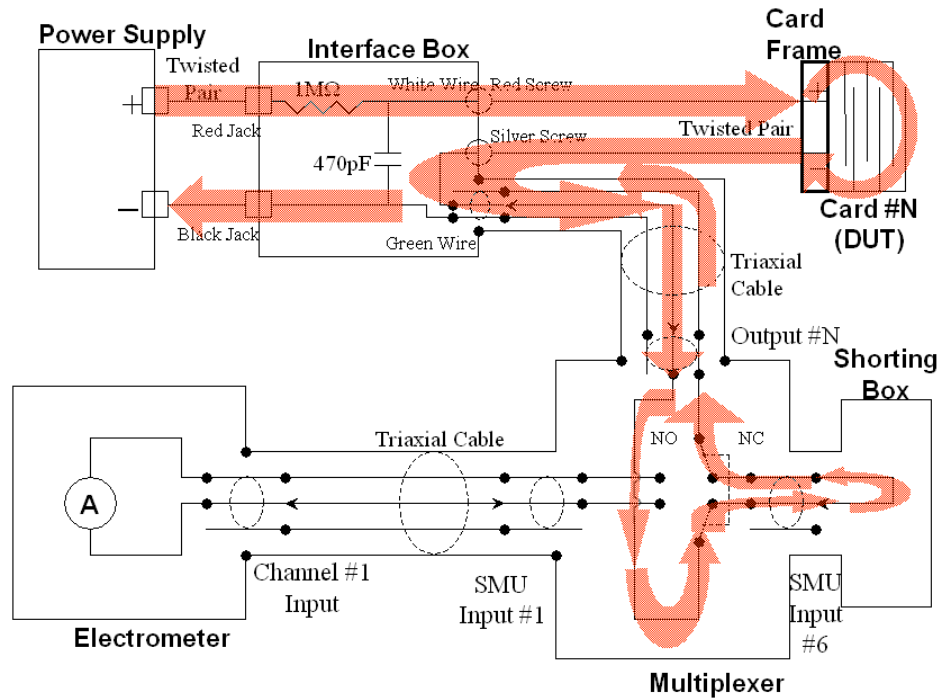

Figure 39. The normal current path is shown in red, going through a shorting box.

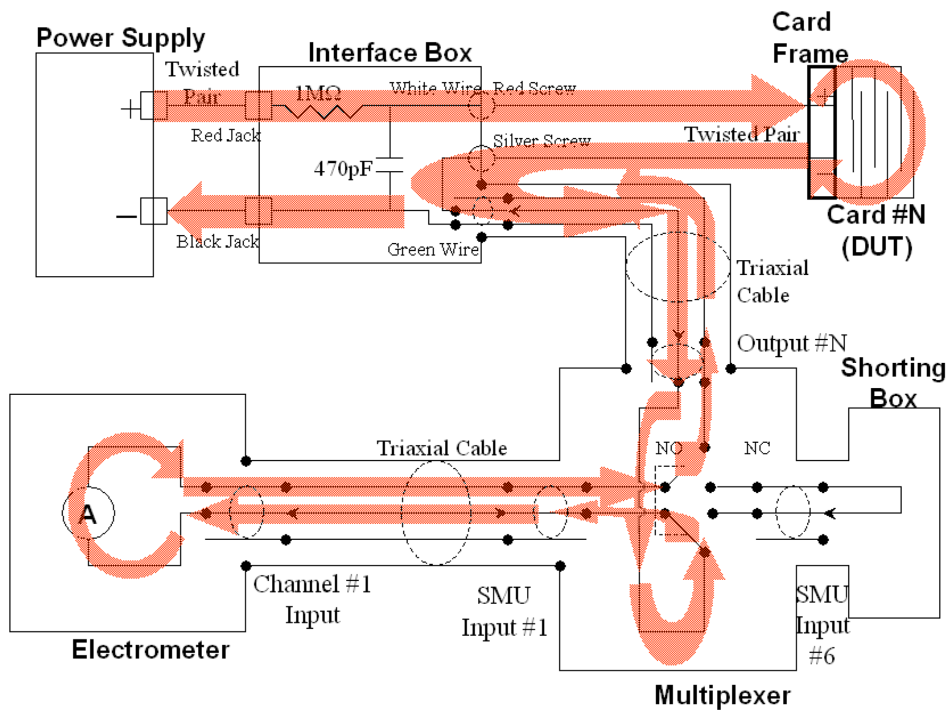

Figure 40. The current path, shown in red, obtained by "opening" the shorting box, and allowing the current to flow through the electrometer,was used when a device was being tested.

The specifications of interest for the Agilent 4349B High Resistance Meter are:

Measurement time (10 –40 ms),

Resistance (103 – 1015) ohms

Delay time (0 – 10 seconds in steps of 0.001 seconds)

Current (1 picoamp – 100 microamps)

As shown in the schematic of the electrical monitoring circuit, a 1-megaohm current limiting resistor was placed in series with the current path to prevent “blow-out” of the fragile filaments when shorting occurs. For the each test, 20 boards (5 of each type) were used since the system could monitor only 48 channels, and each board had two circuits. Each of the boards had to be electrically connected to the interface box, which was then connected to the power supplies and the multiplexer unit (see Figure 41). Each of the electrical connections between the boards and the interface box was uniquely labeled to identify the sample and the monitoring channel for each of the respective samples.

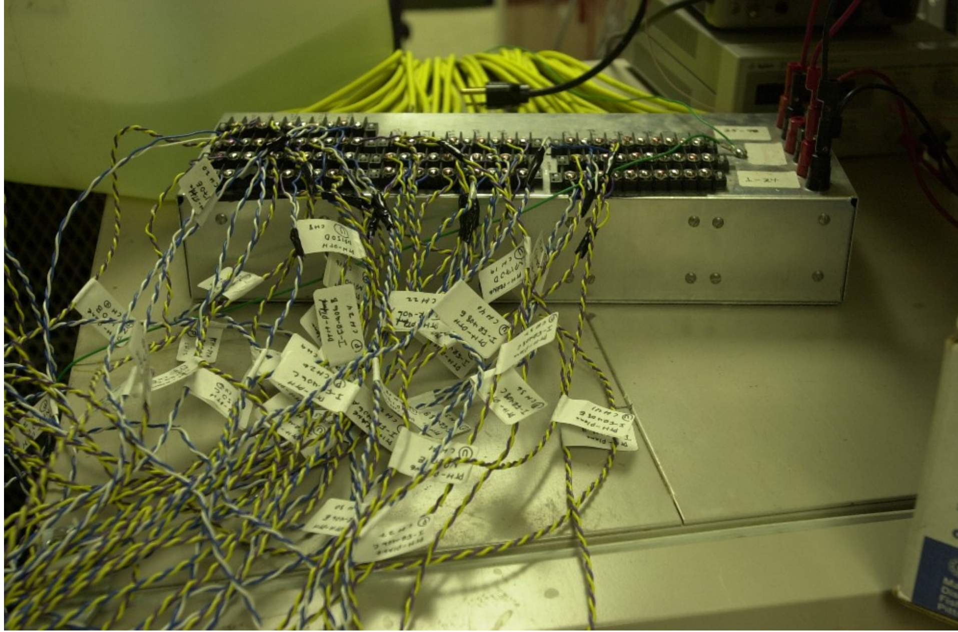

Figure 41. Light colored wires were used for the positive connections (yellow and white) while the darker colored wires (purple and blue) were used for the negative connections. This nomenclature helped to avoid polarity mix-ups.

6.4 Moisture Absorption Characterization

One sample from each of the four laminate types was examined for moisture absorption characteristics. This was accomplished by first drying each of the samples at 105°C until there was a negligible decrease in weight, indicating that virtually all of the moisture had been driven off. The balance used to determine the weight change was a Mettler AE 100, accurate to 0.0001 grams. The weight percent increase due to absorbed moisture in an environment of 85°C/85% RH was calculated by:

$$\%\ Moisture\ Absorption = \left(\frac{W_i - W_o}{W_o}\right)\cdot 100\% \qquad (17)$$

where, W_i is the new weight after exposure at certain intervals, and W_o is the dry weight.

A graph of the weight percent increase with time, up to 700 hours for each of the four sample types, is shown in Figure 42. The graph shows that the boards are still not fully saturated after 700 hours at these conditions.

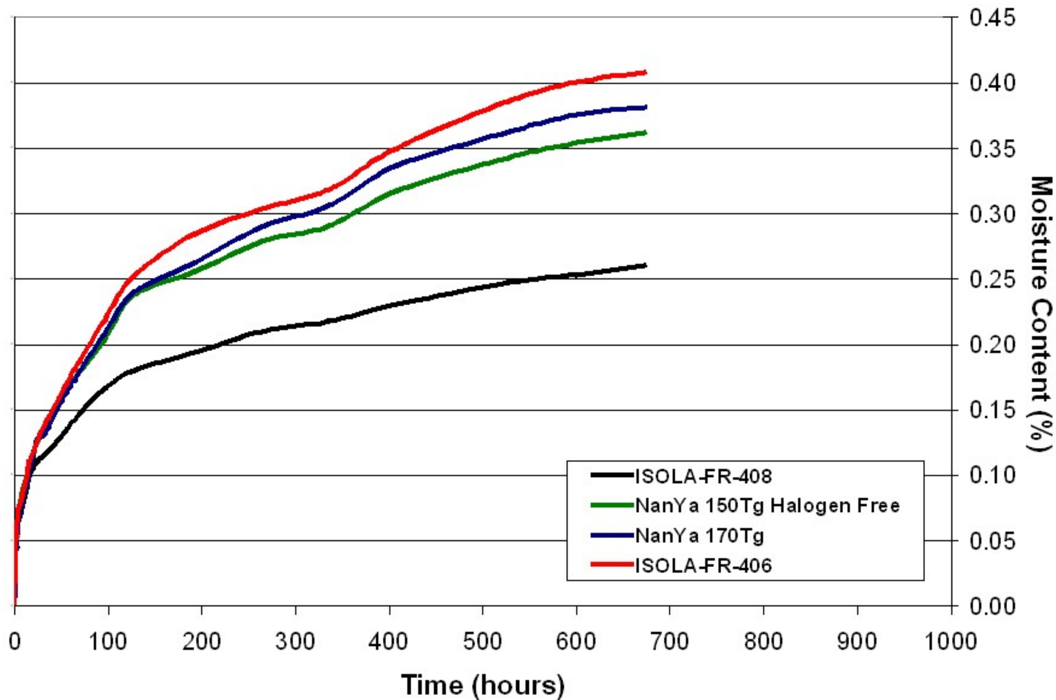

Figure 42. Moisture absorption characteristics for the four board types exposed to 85°C/85% RH for 700 hours are shown.

6.3 Experimental Testing

Two types of tests were conducted. The first type of testing involved monitoring of the insulation resistance of preconditioned samples during the temperature-humidity biased exposure using all three different spacing designs (nominal feature (NF), advanced feature (AF) and next generation (XG). The second type of testing was a dielectric breakdown voltage test to assess the correlation between time to failure observed by the first type of tests (monitoring of the insulation resistance breakdown voltage) and the voltage at which dielectric breakdown occurs.

6.3.1 Insulation Resistance Monitoring

For the first test, 20 boards (5 of each type, designated as A-E) with the largest conductor spacings (nominal feature size: PTH-to-PTH = 6 mil, PTH-plane = 8 mil) were used. The initial voltage, set at 10 volts, was applied to only 3 of 5 samples (A, B and C) in each group (this includes PTH-PTH and PTH-plane) at the start of the test. When a failure was detected in any of the powered samples, power was then applied to the remaining 2 in that group (D and E) to assess the effect of delayed bias on time to failure. As per the IPC specifications, the duration of the test was 500 hours. A graph of the insulation resistance for the PTH-PTH conductor geometry for the 500-hour duration is shown in Figure 43. The missing data, from the beginning of plot up to 34 hours, was lost due to a computer lockup, because the Excel software auto-save was activated, and could not save while data was continuously being sent. Disabling the auto save resolved the problem.

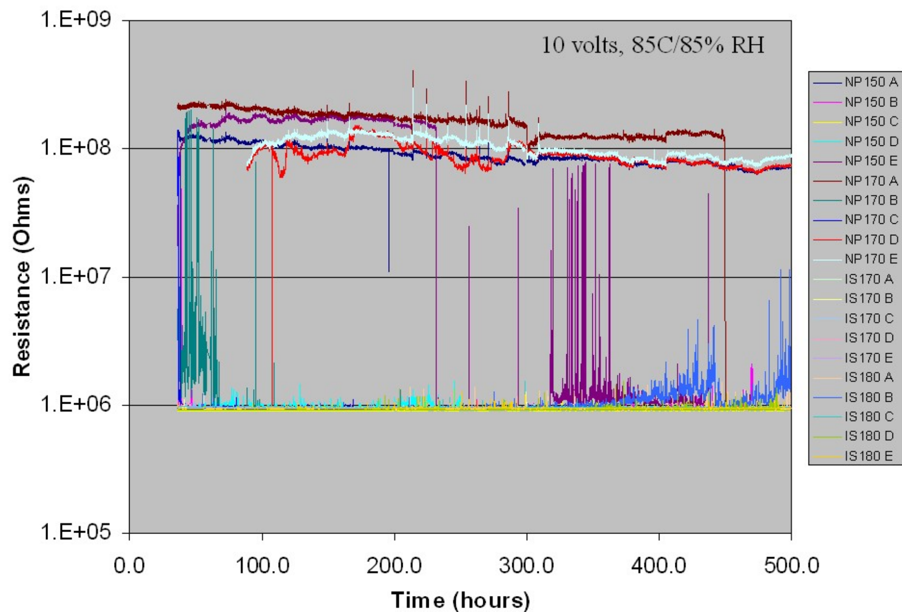

Figure 43. Plot of the PTH-PTH insulation resistance for the 20 samples exposed to 85°C/85% RH at a 10-volt bias

Plots at different time intervals in Figure 44 show the intermittent nature of the PTH-PTH failures during the exposure to 85°C/85% RH at a 10-volt bias.

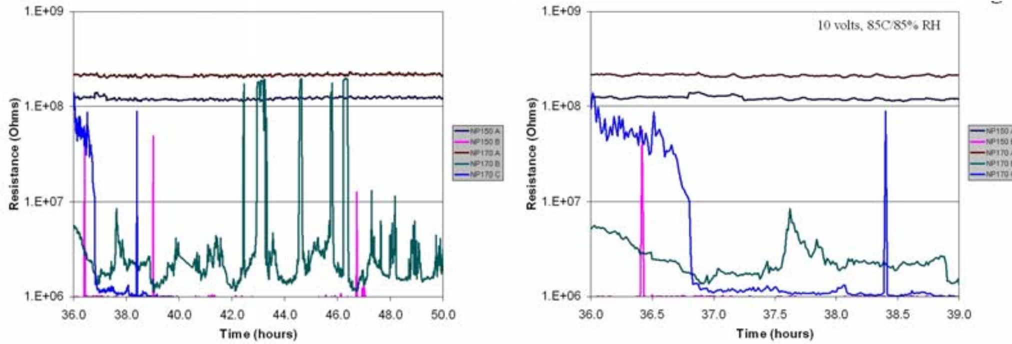

Figure 44. Plot showing PTH-PTH intermittent nature of the failures

Some of the intermittent failures were for short durations of time, even for less than 6 minutes. Monitoring once every 24 – 100 hours according to IPC-TM-650 specifications may miss these types of failures (see Figure 45).

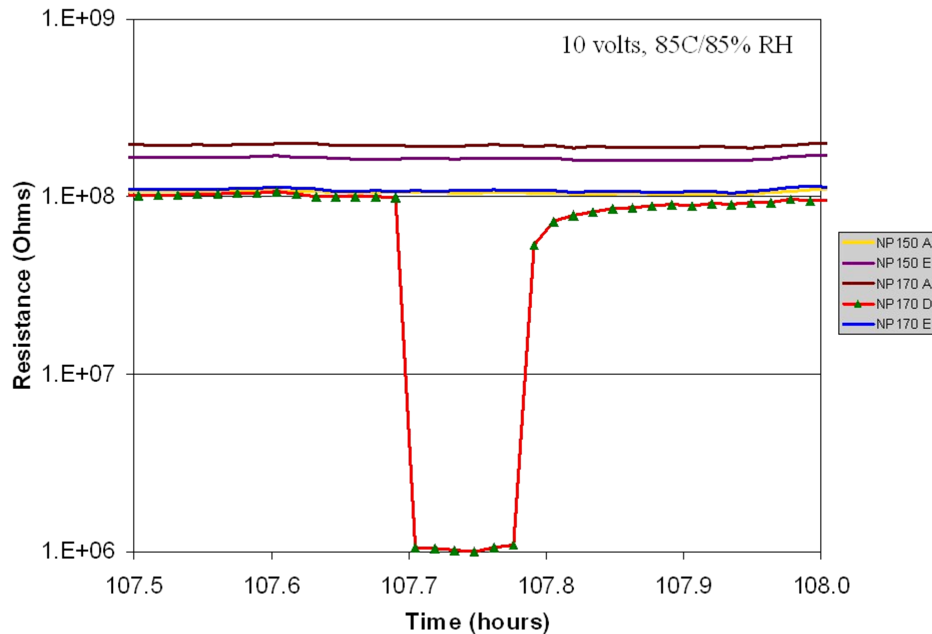

Figure 45. Intermitent failures can last for less than 6 minutes. Monitoring every 24 hours according to IPC-TM-650 specifications may not catch these short duration failures.

Table 2 gives the different times to failure at the PTH-PTH locations for the 20 samples biased 10 volts based on three different criteria:

- Complete short (resistance of the current limiting 1-Megaohm resistor)
- 100 Megaohm resistance or below (IPC/EIA J-STD 001-C, appendix B)
- Decade drop in resistance (IPC-TM-650 2.6.25).

None of the PTH-plane sites failed during the 10 volt, 500 hour test duration. The failure times based on the three failure criteria are shown in Table 2, while a ranking based on resistance to CFF is given in Table 3.

Table 2. Time to failure for the PTH-PTH sites at 10 VDC based on three criteria

Test Coupons		**Time to failure after bias per failure definition (hours)**			
Board Type	**Sample**	**1 Megaohm**	**100 Megaohm**	**Decade drop**	**Minimum**
NanYa Plastics 150 T_g Halogen Free	A	(506)	137	(506)	137
	B	0 - 34	0 - 34	0 - 34	0 - 34
	C	0 - 34	0 - 34	0 - 34	0 - 34
	D	0.3	0.3	0.3	0.3
	E	195	0.3	0.3	0.3
NanYa Plastics 170 T_g	A	450	450	450	450
	B	62	0 - 34	62	0 - 34
	C	39	0 - 34	36.8	0 - 34
	D	(434)	72	72	72
	E	(828)	174	(828)	174
Isola FR-406 170 T_g	A	0 - 34	0 - 34	0 - 34	0 - 34
	B	0 - 34	0 - 34	0 - 34	0 - 34
	C	0 - 34	0 - 34	0 - 34	0 - 34
	D	0.3	0.3	0.3	0.3
	E	0.3	0.3	0.3	0.3
Isola FR-408 180 T_g	A	0 - 34	0 - 34	0 - 34	0 - 34
	B	0 - 34	0 - 34	0 - 34	0 - 34
	C	0 - 34	0 - 34	0 - 34	0 - 34
	D	0.3	0.3	0.3	0.3
	E	0.3	0.3	0.3	0.3

Samples in the highlighted rows (D, E) had a delayed bias. This bias was applied only after one in that group (A, B or C) failed. The samples in brackets did not fail at 10 volts; they failed at 50 volts. The Nanya Plastics laminates appear to perform better.

Table 3. Ranking of samples by greatest time to failure, based on failure definition of resistance drop to 1 megaohm.

CFF resistance ranking per failure definition of 1 megaohm	
Sample	**Time to failure (hrs)**
NanYa Plastics 170 T_g	(828)
NanYa Plastics 150 T_g	(506)
NanYa Plastics 170 T_g	450
NanYa Plastics 170 T_g	(434)
NanYa Plastics 150 T_g	195
NanYa Plastics 170 T_g	62
NanYa Plastics 170 T_g	39
NanYa Plastics 150 T_g	0.3
NanYa Plastics 150 T_g	0.3
NanYa Plastics 150 T_g	0.3
Isola FR-406 170 T_g	0.3
Isola FR-406 170 T_g	0.3
Isola FR-406 170 T_g	0.3
Isola FR-406 170 T_g	0.3
Isola FR-406 170 T_g	0.3
Isola FR-408 180 T_g	0.3
Isola FR-408 180 T_g	0.3
Isola FR-408 180 T_g	0.3
Isola FR-408 180 T_g	0.3
Isola FR-408 180 T_g	0.3

For the PTH-plane circuits, since no failures were observed after 500 hours at 10 volts, and 85°C/85% RH, the voltage was increase to 50 volts in an attempt to induce failure. A plot of the PTH-plane insulation resistance of the samples during the 500 hour, 50 volt exposure is shown in Figure 46.

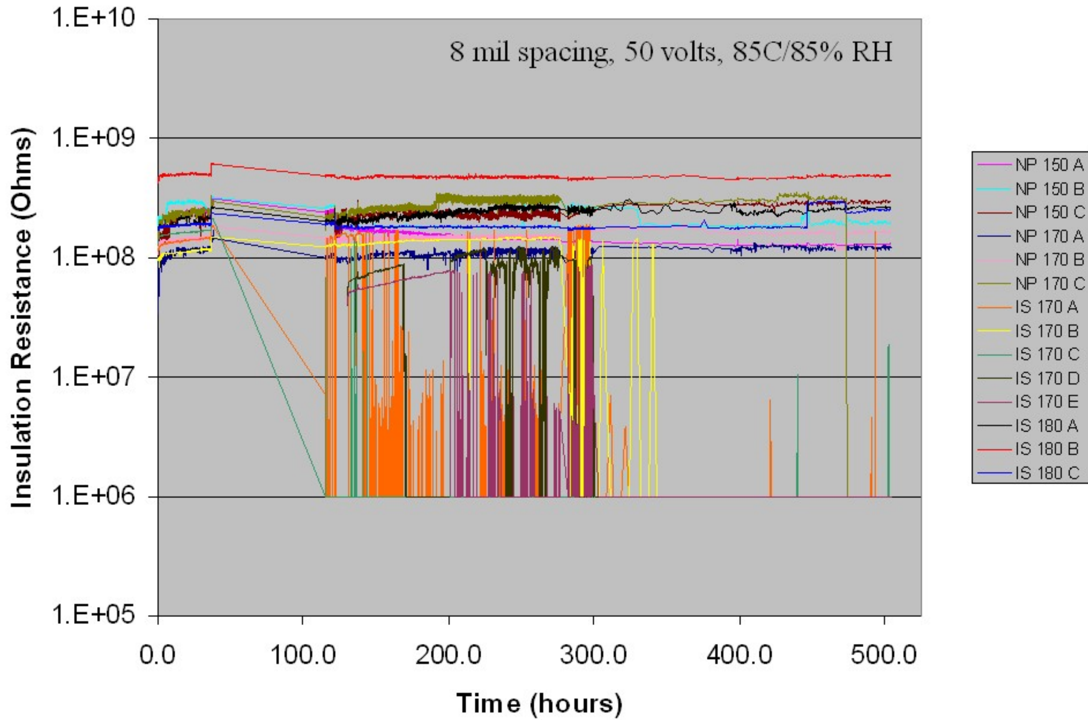

Figure 46. This plot shows the internal resistance of the PTH-planes in the powered samples. Isola samples, IS 70A and IS 70C, failed between 30 and 130 hours. The missing data section, seen as straight lines, was due to a power outage.

Again, CFF's intermittent nature is seen in plots at different intervals in Figure 47.

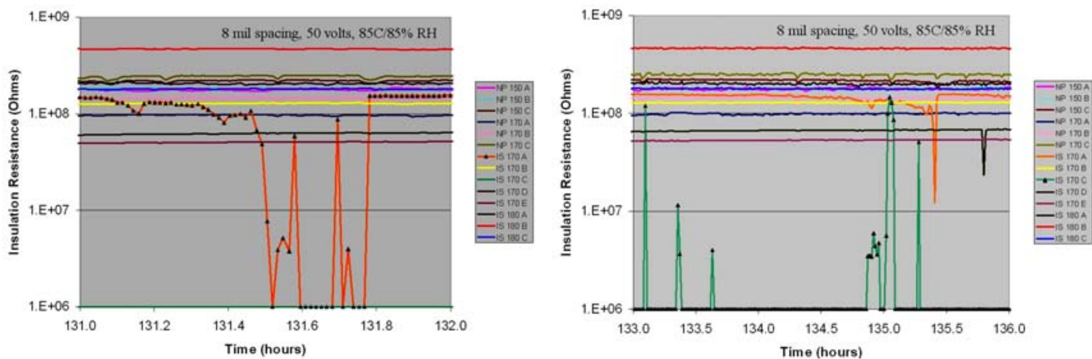

Figure 47. Plots of the resistance in the PTH-planes show intermittent behavior.

Close to the end of the 50-volt testing of the PTH-plane circuitry, the number of surviving samples can be seen by the remaining lines above the 1E8 ohms marker. One sample, NP 170C, is observed to abruptly fail at approximately 474 hours (see Figure 48).

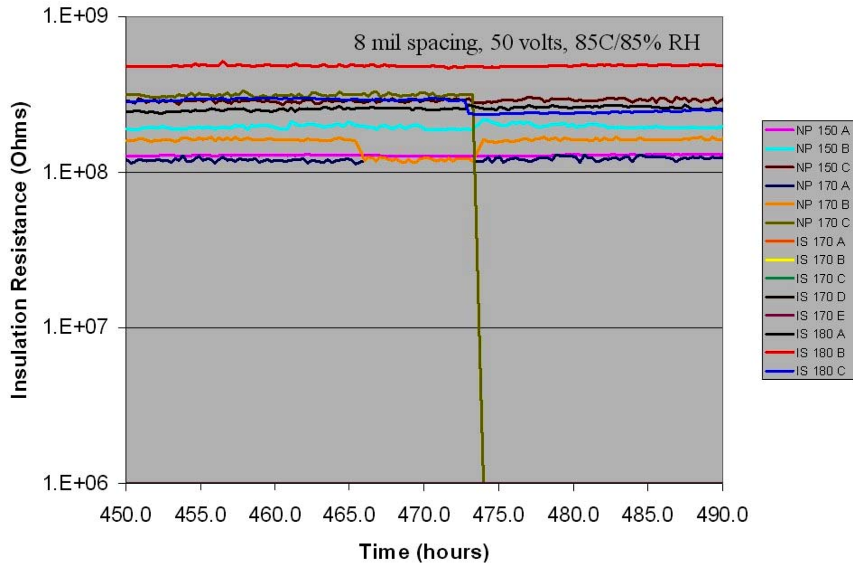

Figure 48. Close to the end of the 50-volt testing of the PTH-plane circuitry, 8 surviving samples can be seen above the lines above 1E8 ohms.

The next increase in voltage for the PTH-plane circuits in these samples was from 50 up to 100 volts. A plot of the insulation resistance for the 500-hour duration at this higher voltage is given in Figure 49. Again the intermittent nature of CFF is observed. This test was then terminated after a combined exposure of 500 hours at 10 volts, plus 500 hours at 50 volts, in addition to the 500 hours at 100 volts.

A set of 20 AF samples with the intermediate spacings of 4 mil PTH-PTH edge and 6 mil PTH-plane, were tested after soaking for 96 hours at 85°C/85% RH. Upon application of the voltage (12 samples biased at 4.5 volts, the remaining 8 samples biased at 2 volts) and monitoring, the insulation resistance, it was observed that 18 of

the samples had failed at time 0; the other two failed within 5 minutes. The voltages selected to represent V/d^n, where n is 2 and 4 (literature reports that time to failure is dependent on V/d^n, where n = 2, 3 or 4) compared to the first set of tests where:

V/d^2 = 10 volts/(6 mils)^2 = 0.278 and V/d^4 = 10 volts/(6 mils)^4 = 7.72 E-3

Using these values and the new spacing of 4 mils, solving for the voltages gives:

$V/4^2$ = 0.278, therefore V ~ 4.5 volts for n = 2 and

$V/4^4$ = 7.72 E-3, yielding a V ~ 2.0 for n = 4

Since this is uncharacteristic of CFF failures (time necessary for path formation and subsequent filament growth), these failures were not assumed to be due to CFF. After removal from the chamber, the samples were taken to Neocera the next day for analysis. However, upon arrival at Neocera and testing the samples, it was observed that the insulation resistance of each sample had returned to normal; over 500 megaohms as measured prior to testing.

Due to the problem of the immediate failures seen in the AF set of samples, it was decided not to presoak the XG samples for 96 hours at 85°C/85% RH prior to insulation resistance monitoring. The XG samples had the smallest feature size; 3 mils between the PTH-PTH edges and 3 mils between the PTH and ground planes. For this test, two voltages were used; 3 samples from each of the 4 groups were biased at 2 volts (samples A, B and C), while the remaining 2 samples from each group (D and E) were biased at 1 volt. Again, all of the XG samples failed within a relatively short period of time, some in less than 1 minute, not characteristic of CFF failures. The plot of their insulation resistance up to the time of failure is shown in

Figure 50. After removal from the chamber and immediately taking to Neocera for current mapping, it was observed that there was a current leakage in the samples, but unlike a CFF failure where there is usually one distinct failure site. More information on this is given in section 6.6 entitled “Failure Analysis”. It is likely that this is the same failure mechanism experienced by the early failing set of AF samples.

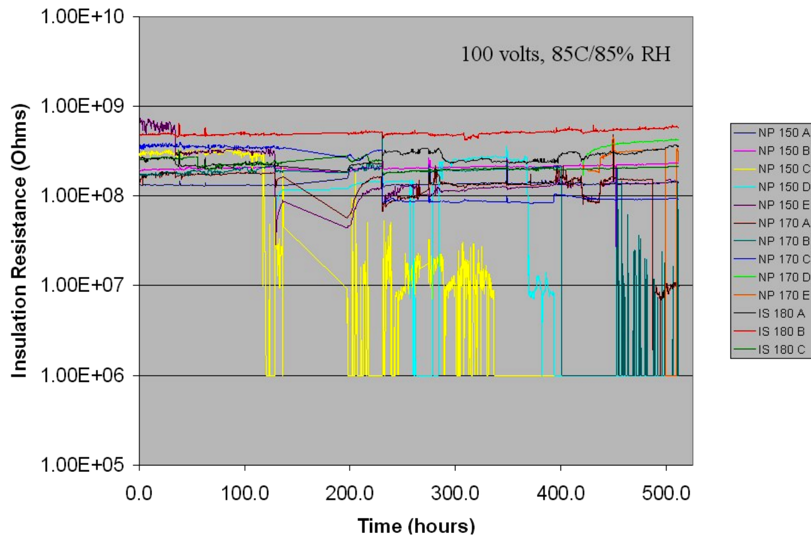

Figure 49. This plot shows the insulation resistance monitored at 100 volts for the duration of 500 hours. Some of the samples did not fail.

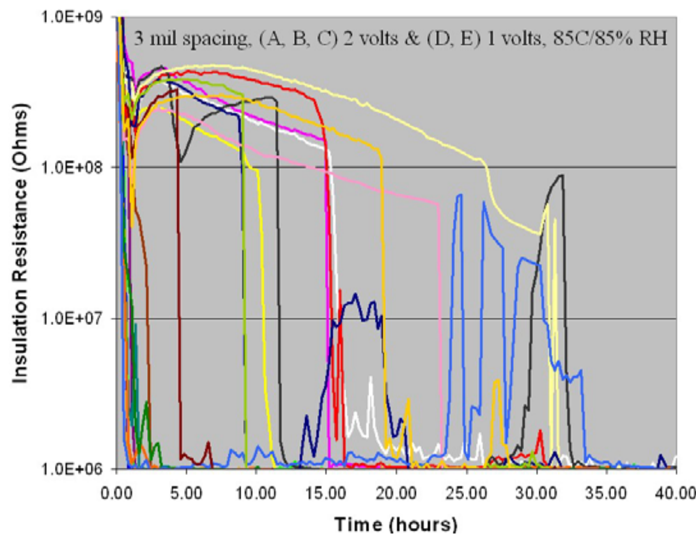

Figure 50. This plot shows the insulation resistance for the PTH-PTH XG samples up to 40 hours, at which time all had failed.

Tables 4 and 5 show the failure times and ranking for the PTH-PTH conductor geometry in the NF samples respectively.

Table 4. NF PTH-PTH

Test Coupons		Time to Failure (hours)	
Board Type	**Sample**	**1 Megaohm**	**100 Megaohm**
NanYa Plastics 150 T_g Halogen Free	A	(505)	(505)
	B	(505)	(505)
	C	123	118
	D	133	133
	E	(505)	80
NanYa Plastics 170 T_g	A	487	200
	B	403	403
	C	474	474
	D	(90)	(90)
	E	76	76
Isola FR-406 170 T_g	A	37-117	37-117
	B	283	283
	C	37-117	37-117
	D	38	0
	E	72	0
Isola FR-408 180 T_g	A	(505)	(505)
	B	(505)	(505)
	C	(505)	(505)
	D	(Not biased)	(Not biased)
	E	(Not biased)	(Not biased)

Table 5. NF PTH-PTH

CFF resistance ranking per failure definition of 1 megaohm	
Sample	**Time to failure (hrs)**
Isola FR-408 180 T_g	(505)
Isola FR-408 180 T_g	(505)
Isola FR-408 180 T_g	(505)
Isola FR-408 180 T_g	(Not biased)
Isola FR-408 180 T_g	(Not biased)
NanYa Plastics 150 T_g	(505)
NanYa Plastics 150 T_g	(505)
NanYa Plastics 150 T_g	(505)
NanYa Plastics 170 T_g	487
NanYa Plastics 170 T_g	403
NanYa Plastics 150 T_g	133
NanYa Plastics 150 T_g	123
NanYa Plastics 170 T_g	(90)
NanYa Plastics 170 T_g	76
NanYa Plastics 170 T_g	474
Isola FR-406 170 T_g	283
Isola FR-406 170 T_g	72
Isola FR-406 170 T_g	38
Isola FR-406 170 T_g	37
Isola FR-406 170 T_g	37

Table 6. XG PTH-PTH

Test Coupons		Time to Failure (hours)	
Board Type	**Sample**	**1 Megaohm**	**100 Megaohm**
NanYa Plastics 150 T_g Halogen Free	A	1.3	0.5
	B	0.8	0.5
	C	1.1	0.5
	D	1.1	0.3
	E	6.0	4.6
NanYa Plastics 170 T_g	A	16.5	15.0
	B	13.3	11.7
	C	31.3	26.5
	D	9.3	9.3
	E	21.1	19.2
Isola FR-406 170 T_g	A	26.2	15.5
	B	15.2	15.2
	C	11.2	9.8
	D	9.0	9.0
	E	23.3	13.8
Isola FR-408 180 T_g	A	2.4	1.0
	B	1.3	1.0
	C	2.2	0.5
	D	2.4	0.5
	E	3.2	0.5

Table 7. XG PTH-PTH

CFF resistance ranking per failure definition of 1 megaohm	
Sample	**Time to failure (hrs)**
NanYa Plastics 170 T_g	31.3
Isola FR-406 170 T_g	26.2
Isola FR-406 170 T_g	23.3
NanYa Plastics 170 T_g	21.1
NanYa Plastics 150 T_g	16.5
Isola FR-406 170 T_g	15.2
NanYa Plastics 170 T_g	13.3
Isola FR-406 170 T_g	11.2
NanYa Plastics 170 T_g	9.3
Isola FR-406 170 T_g	9.0
NanYa Plastics 150 T_g	6.0
Isola FR-408 180 T_g	3.2
Isola FR-408 180 T_g	2.4
Isola FR-408 180 T_g	2.4
Isola FR-408 180 T_g	2.2
Isola FR-408 180 T_g	1.3
NanYa Plastics 150 T_g	1.3
NanYa Plastics 150 T_g	1.1
NanYa Plastics 150 T_g	1.1
NanYa Plastics 150 T_g	0.8

Tables 6 and 7 show the failure times and ranking for the PTH-PTH in the XG samples, smallest conductor spacing, where samples labeled A, B and C were biased at 2 volts and D and E were biased at 1 volt. The failure times appear to be random, most likely due to the random defects playing more of role in the time to failure at smaller spacings as opposed to the path formation in larger spacings.

6.4 Failure Analysis

After failure of the samples in the first set (NF) due to resistances drop to 1 megaohm (the resistance of the in-series protection resistor), selected samples were sent to Neocera to conduct SQUID to determine if there were indeed failures, and if so, where were the locations. One of the samples that failed early in the test, an Isola FR-406, was analyzed using the SQUID to confirm and locate the short due to conductive filament formation. Figure 51 shows the SQUID output, locating the shorted sites in the board, in both the PTH-PTH and PTH-power plane conductor geometries.

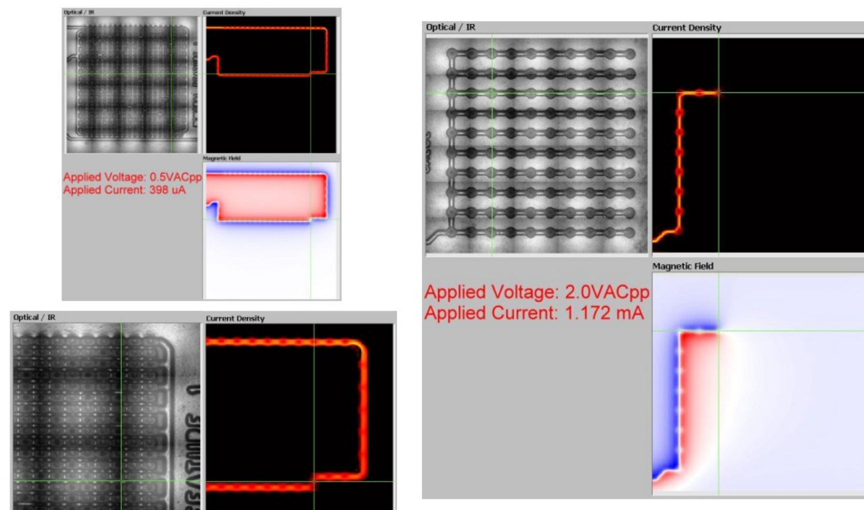

Figure 51. The SQUID output shows the current mapping images, verifying that there were short circuits and determining their locations respective to the board conductors.

After the short circuits were identified, cross-sectional techniques were employed to locate the defects responsible for the shorts and allow examination of the defective areas using optical and E-SEM microscopy.

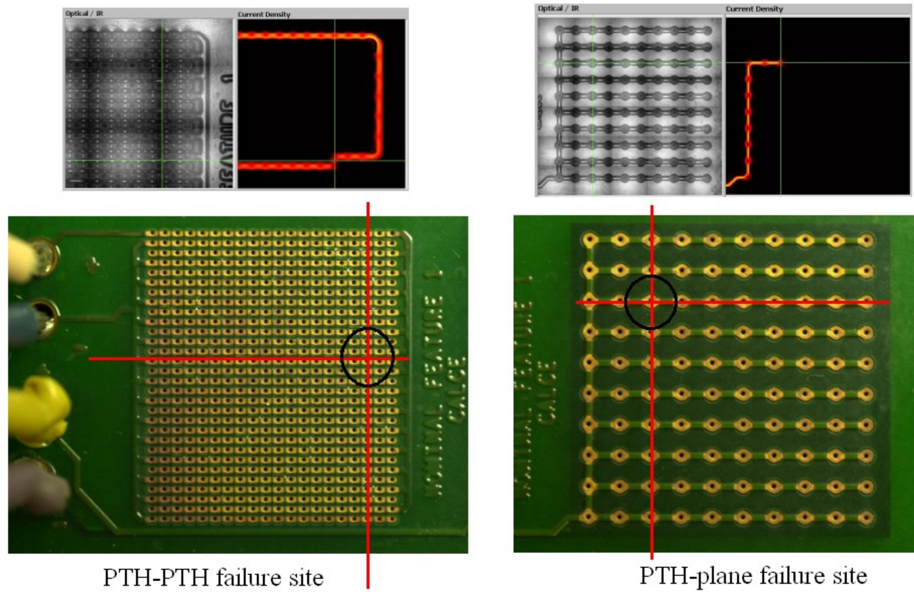

Figure 52. SQUID mapping and respective conductor locations identified for cross-sectioning.

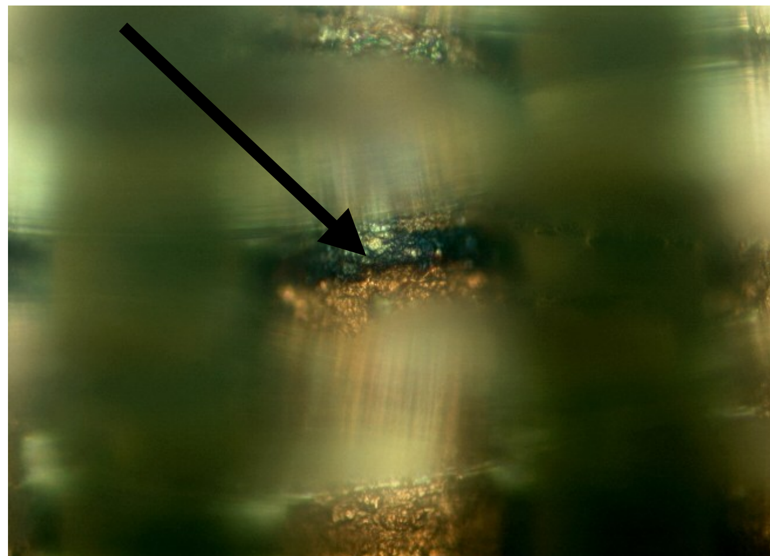

Figure 53. Prior to reaching the failure site, circular blue/black areas, possibly $Cu(OH)_2$ due to the copper reaction with water, were observed.

The identified sites for cross-sectioning are shown in Figure 52. During the cross-sectioning, blackish blue areas were seen on most of the PTHs. This may be $Cu(OH)_2$ due to the copper reacting with the ingressed water (see Figure 53). Upon reaching the location indicated by the current mapping techniques of the SQUID, a copper colored filament was observed to bridge the two PTHs, almost in the middle of the board thickness (see Figure 54 and Figure 55.). In the PTH-plane shorted site, cross-sectional techniques again located a copper filament connecting the PTH and a ground plane (see Figure 57).

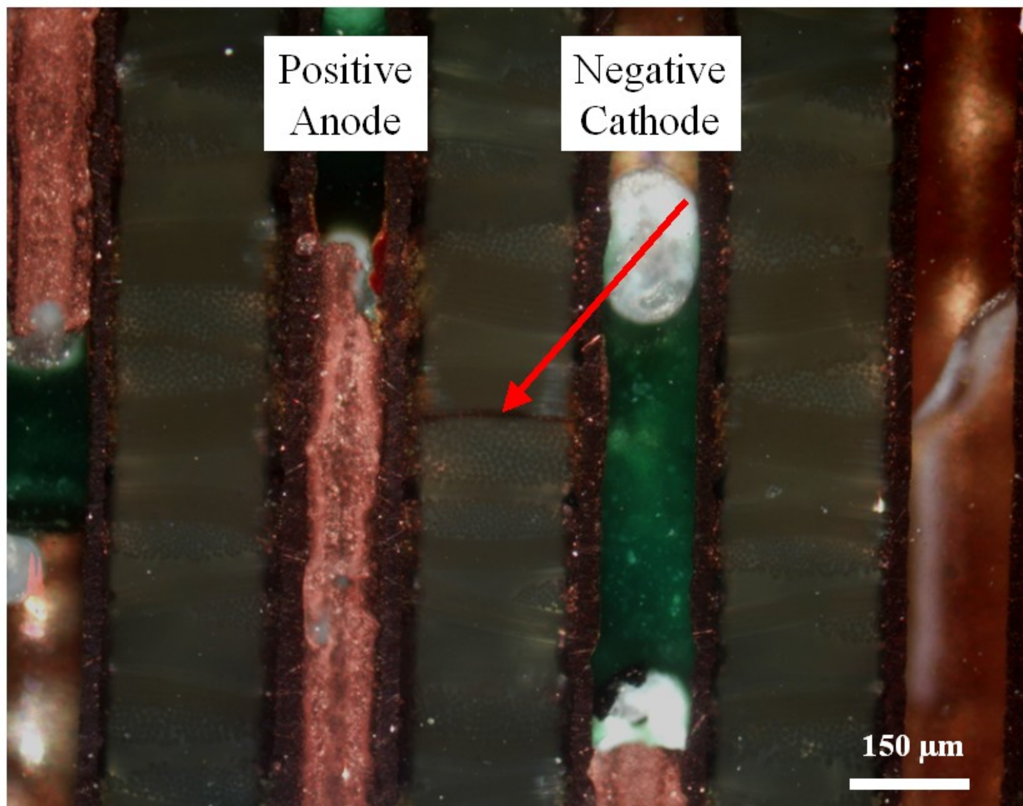

Figure 54. A filament was observed bridging two PTHs, at the same location predicted by the SQUID (see red arrow).

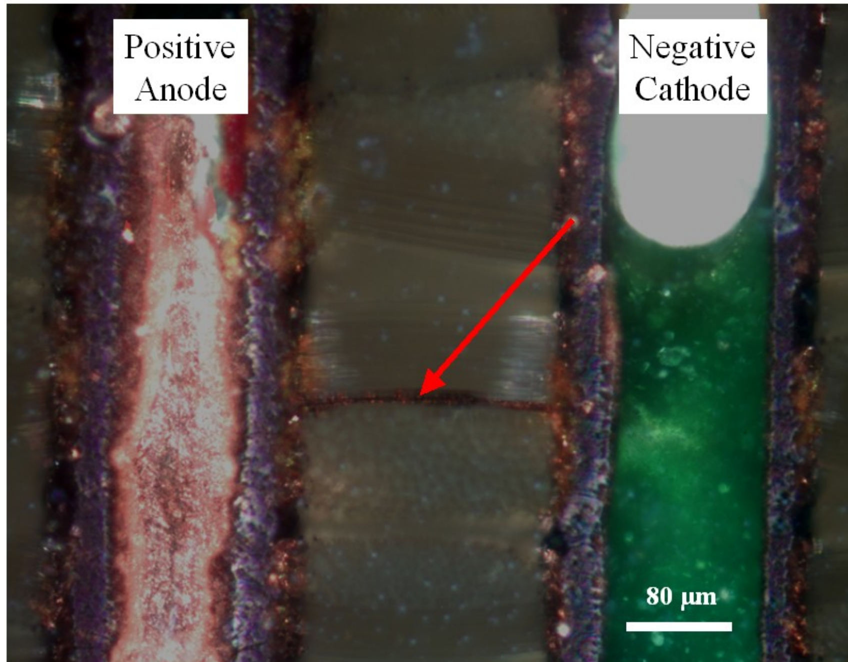

Figure 55. This optical micrograph shows an enlargement of the shorted site.

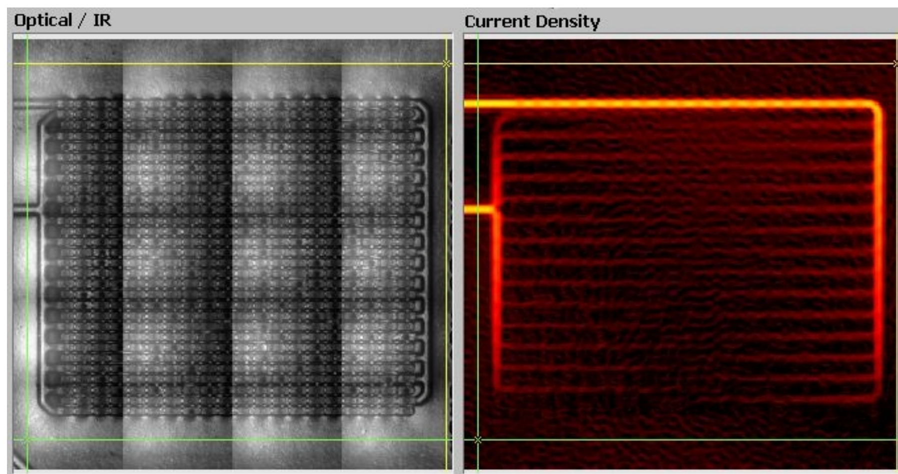

Figure 56. Current mapping of one of the failed XG samples at the PTH-PTH grid shows that the current follows the grid pattern, and contains many leakage paths; not only one leakage path as in the CFF validated failures. It is possible that this was the same failure mechanism observed in the early failing AF samples as well.

E-SEM examination of the localized failure site revealed delamination at the fiber-epoxy interfaces in areas immediately surrounding the failure site (see Figure 59).

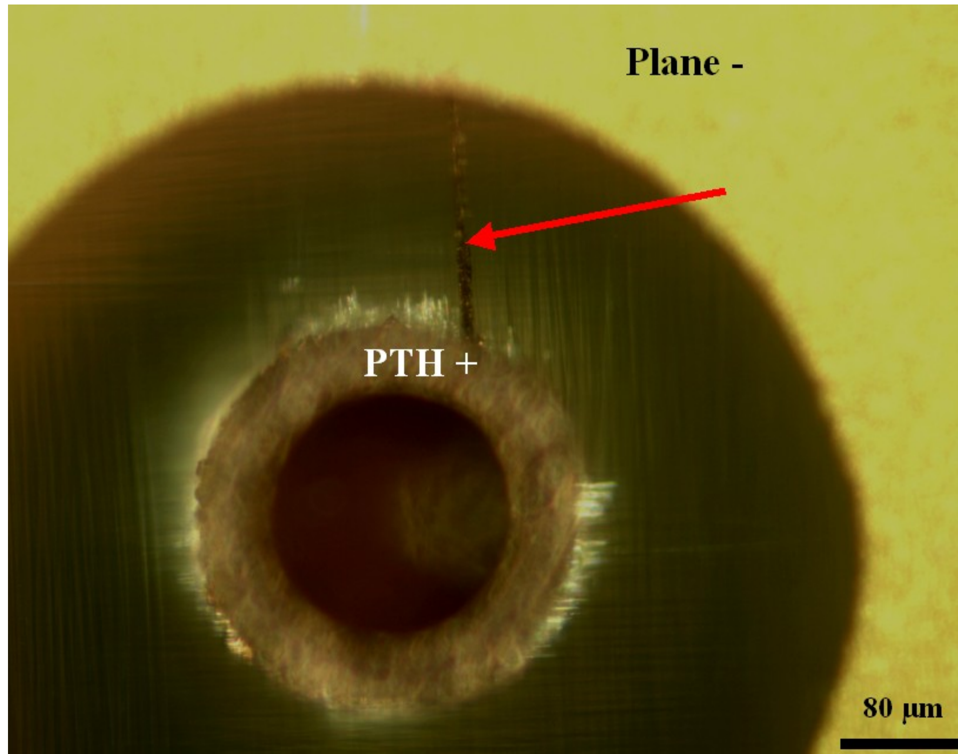

Figure 57. This optical photo shows a copper filament bridging a PTH and ground plane at the precise location predicted by the SQUID.

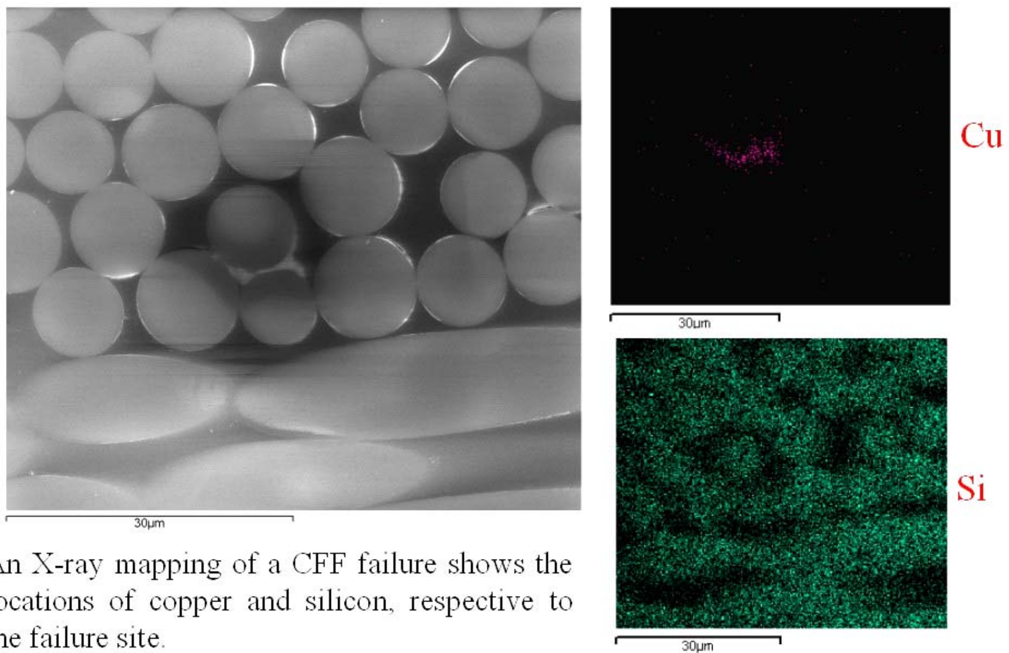

Figure 58. EDS analysis of a cross-sectioned site perpendicular to the filament showed copper in the shorted location.

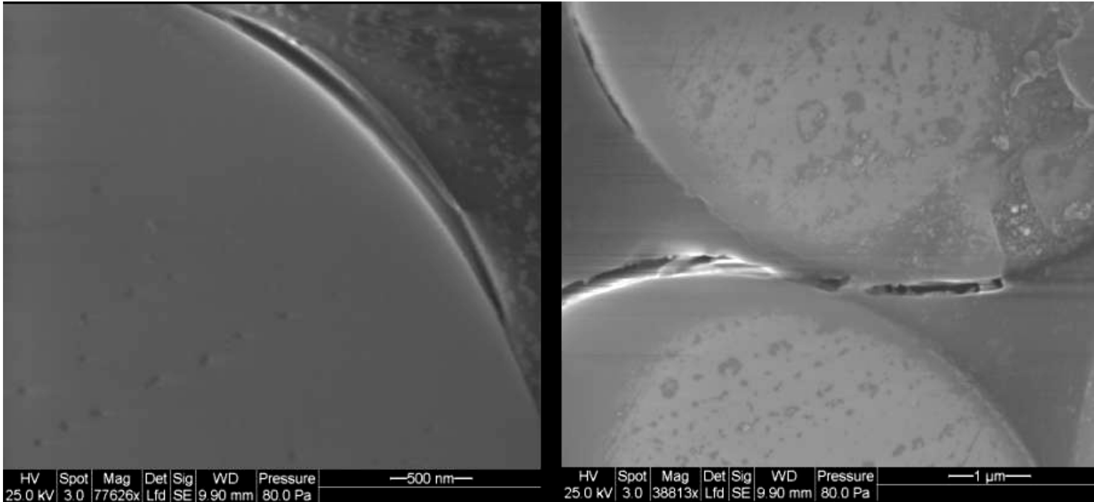

Figure 59. E-SEM examination revealed delamination at the fiber-epoxy interfaces in areas immediately surrounding the failure site.

6.5 Dielectric Breakdown

To assess whether or not a relationship between time to failure due to CFF and dielectric breakdown voltage may exist, 3 samples of each laminate type at the largest spacings (PTH-PTH edge to edge of 6 mils, PTH-plane of 8 mils), were preconditioned at 85°C, 85% RH for 96 hours in accordance with the IPC-TM-650-2.6.25 CAF testing method. This preconditioning was done to precipitate moisture ingress and initiate chemical breakdown of the silane/glass interfacial bond, along the same path typically formed during CFF failures. After the required preconditioning, an increasing voltage (up to 1,000 volts DC, at a rate of 100 volts/min) was applied between the positive and negative inputs for the PTH-PTH grid. The power supply was current limited to 100 milli amps. A volt meter was put in parallel with the circuit to measure the voltage as it was slowly ramped up. The ramp rate was approximately constant, at 100 volts/minute. At breakdown, the dielectric breakdown voltage for the respective sample was recorded. The dielectric strength for air is 3 kV/mm [31].

Based on the PTH-PTH spacing of 6 mils (0.1524 mm), it would take 450 volts to cause an arc across this gap. The PTHs were solder-mask defined, (solder mask covering the air gap between the PTHs) and breakdown voltages varied from 670 to over 999 volts, discrediting that the dielectric breakdown was due arcing across the air. If the breakdown were due to arcing across air, all values would center around 450 volts, not varying from 670 up to over 999 volts.

The specification governing solder mask dielectric strength is a minimum breakdown voltage of 500 VDC/mil [32]. For 6 mils, the solder mask should be able to withstand at least 3,000 volts, far above of what was applied. Therefore, dielectric breakdown was most likely due to an internal breakdown of the dielectric epoxy glass matrix, weakened by moisture ingress. Table 8 shows the dielectric breakdown voltage for each of the samples tested. The values suggest that in a best to worst ranking, the order is:

Nanya Plastics 170 > Nanya Plastics 150 > Isola FR406 > Isola FR408

This ranking follows the same trend as the PTH-PTH 10 volt test bias failure data, implying that dielectric breakdown voltage may be a possible indicator of a PWB's resistance to CFF. The arrangement of photos in Figure 60 shows the internal damage to one of the boards occurring as a result of the dielectric breakdown voltage testing.

Table 8. Dielectric breakdown

Sample NF PTH-PTH – 6 mils	**IS-FR406**			**IS-FR408**			**NY-150**			**NY-170**		
	A	B	C	A	B	C	A	B	C	A	B	C
Breakdown voltage (volts)	850	810	680	670	740	710	910	990	920	940	>999	980

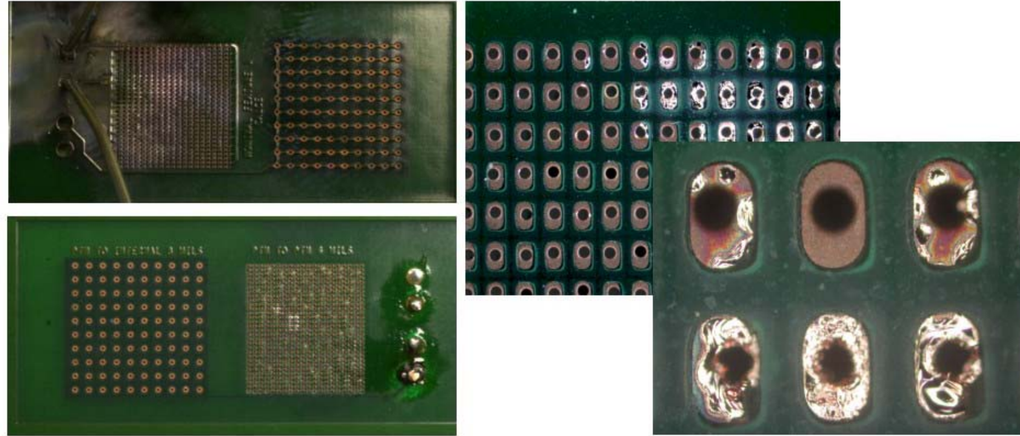

Figure 60. Photos show the damage to the PTH as a result of the dielectric voltage breakdown testing.

A t-test was used to examine the statistical differences among the 4 sets of values obtained from the dielectric breakdown voltage tests. The equation used is:

$$t = \frac{\bar{x} - \bar{y}}{s_p \sqrt{\frac{1}{m} + \frac{1}{n}}} \tag{18}$$

where $\bar{x}$ and $\bar{y}$ are respective sample averages, s_p is the pooled estimator and m and n are respective sample sizes. S_p^2 is calculated by:

$$S_p^{\,2} = \frac{(m-1)\cdot S_1^{\,2} + (n-1)\cdot S_2^{\,2}}{m+n-2} \tag{19}$$

Using equations 18 and 19, along with the values from Table 8, the t values obtained for the paired comparisons, along with the confidence level, show that there is a distinguishable difference between the respective pairs, as shown in Table 9. It can be concluded with 90% confidence that there is a difference between the samples in the last four rows. In other words, the values obtained from the dielectric breakdown tests, may reveal the relative susceptibility of a PWB type to CFF.

Table 9. Paired t-test values

Board Types Compared		T value	Reject or accept at 90 %
Isola FR-406	Isola FR-408	1.33	Less than 90% confidence in difference
NanYa Plastics 150	NanYa Plastics 170	1.09	Less than 90% confidence in difference
Isola FR-406	NanYa Plastics 150	2.80	More than 90% confidence in difference
Isola FR-406	NanYa Plastics 170	3.56	More than 90% confidence in difference
Isola FR-408	NanYa Plastics 150	7.22	More than 90% confidence in difference
Isola FR-408	NanYa Plastics 170	9.97	More than 90% confidence in difference

CHAPTER 7: PATH FORMATION

Prior to formation of the filament, consistent with the published literature, a pathway connecting the oppositely biased conductors must be formed. Some of the more common pathways are show in Figure 61 Other path configurations include formation between PTHs and power/ground planes, between internal traces, between an internal trace and a PTH, and between internal and surface traces.

It is hypothesized that path formation, which is proposed to be voltage independent, is the rate-limiting step in conductive filament formation. In other words, it takes a much longer time for the pathway to be formed than for the metal migration and formation of the conductive filament bridging and shorting the two conductors. This chapter discusses the different ways in which this path may be formed.

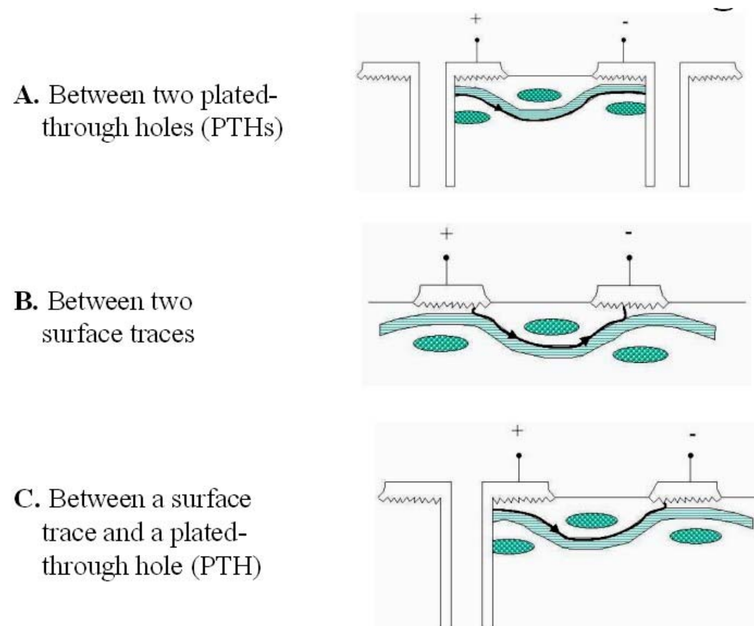

Figure 61. Three common CFF pathway configurations

7.1 Modes of Path Formation

7.1.1 Mechanical Degradation

One mode of path formation is mechanical degradation or physical delamination at the interfaces of the glass fibers and epoxy resin matrix. Mechanical stress can arise due to the coefficient of thermal expansion (CTE) mismatches in the properties of the epoxy resin and the glass fibers. Epoxy resin has a CTE of approximately 60 ppm/^{o}C, while that of the glass fibers is around 5 ppm/^{o}C. This mismatch can lead to high interfacial stresses and debonding at the fiber-resin interface during thermal cycling [15]. The interfacial debonding observed by Li et al. was more severe at the outer fibers in the bundles. Manufacturing defects, as discussed in Chapter 3, can accelerate and help to initiate the formation of this pathway.

The difference in the moisture absorption of glass fibers and epoxy resin can also lead to interfacial stresses. During thermal-humidity cycling, the swelling and shrinking of the epoxy has been shown to induce physical debonding at the fiber glass/epoxy resin interface, in addition to micro-cracking in the resin. The absorption of moisture can also reduce the T_g of the laminate, allowing excess thermal stress to cause more damage. Path formation, where there is a physical, mechanical separation at the fiber glass/epoxy resin interface or micro-cracking due to thermal cycling and thermal-humidity cycling, is not reversible.

7.1.2 Chemical Degradation

A pathway between conductors may also be formed by chemical hydrolysis of the silane glass finish or coupling agent. Studies indicate that the glass epoxy interface absorbs 5 to 7 times more moisture than the bulk epoxy [16]. The most common cross-linking agent used in FR-4 and many other epoxy-based laminated systems is dicyandiamide (aka dicy). Dicy is hydrophilic and to some extent, so is the glass surface. This combination of a hydrophilic surface and a hydrophilic cross-linking agent appears to be one of the factors responsible for the mechanism where by chemical degradation of glass fiber/epoxy resin interface due to hydrolysis occurs. Varnell et al. has shown that PWBs manufactured with non-dicy cross-linked epoxy resins exhibit much more resistance to CAF failures compared to PWBs manufactured with dicy cross-linked epoxy resins [17]. Research by Lando et al. demonstrated that this type of chemical degradation might be reversible.

7.1.3 Hollow Fibers

During the manufacture of glass fibers, a homogeneous melt composition with negligible impurities is necessary to prevent the decomposition of raw materials. The sublimation of these organics can lead to trapped gases. Depending on the viscosity of the glass mixture and various manufacturing processes, these gases can get trapped as bubbles, called seeds. Seeds are a naturally occurring part of the process and thus methods to remove them are necessary. If the molten glass contains a sufficient level of impurities, air bubbles may become trapped inside the fibers while being drawn through the bushing. These air bubbles, unless very large, do not cause fiber breakage but end up as capillaries in the glass fibers, otherwise known as hollow fibers. These

hollow glass fibers increase the opportunity for failure between close conductors because the capillary provides a convenient path for the formation of conductive filaments. As discussed earlier in Chapter 4, hollow fibers pose a serious reliability threat in that they can remove the rate limiting step, T_1, from the proposed two step sequential process, T_1 consisting of path formation, followed by T_2 the electrochemical reaction, where $T_1 >> T_2$ [5], [6].

7.1.4 Vertical Filament Formation

In a set of PWBs failing by shorted internal planes, verification of the hypothesized root-cause required actual physical identification of a hydrolyzed Cab-o-sil particle at a failure site. Unfortunately, this was made difficult by large area covered by the power and ground planes, which made identification of the failure site using functional or parametric testing literally impossible. Visual inspection was also difficult due to the absence of a controlled burn area. The high glass transition temperature (T_g) of the dielectric material, 180°C, makes it relatively resistant to high temperatures. Therefore, an internal temperature rise to 200°C can result in solder reflow in the PTH's, but will not visibly damage the dielectric material. The temperatures necessary to ignite Megtron material may be so high as to result in thermal runaway. The effect is binary: failed boards will either have no visible charring or will have large areas of the board severely burned, with any evidence of root-cause destroyed. Either case will tend to hide the physical object causing the electrical short.

This behavior also prevented the use of thermal imaging, since the energy required to dissipate sufficient heat also tended to result in damage to the failure site. The solution was to modify a procedure used at CALCE to identify very small voids that bridge ceramic capacitors and cause current leakage. The resistance between a power and ground pin were monitored as the board was sectioned. Using a binary approach, the potential failure site was narrowed to a very small area. This area was very slowly ground and polished until a change in resistance was observed.

During several attempts to observe a non-damaged failure site, a large angular particle was identified at a failure site. The images are displayed in Figure 62, Figure 63 and Figure 64. One additional non-damaged failure site was identified. This board contained a 4-mil core between power and ground, as opposed to the 2-mil core material that was experiencing field failures. The images seem to show a particle of similar coloring as that seen in the board with the 2-mil core.

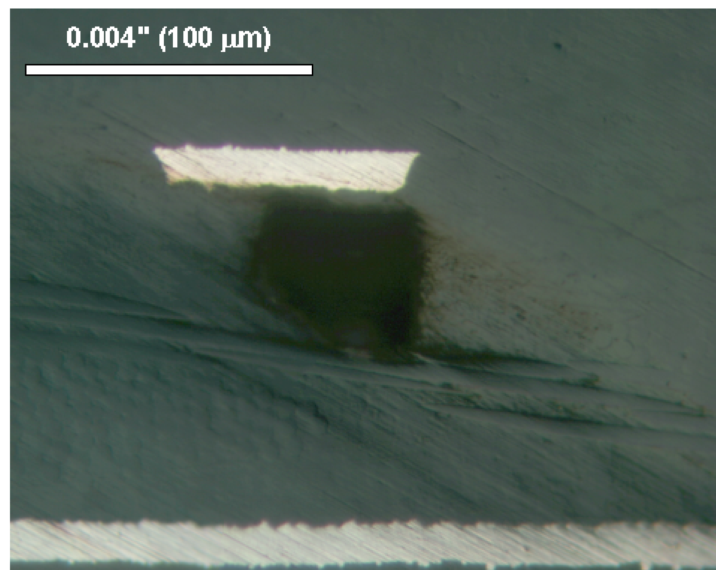

Figure 62. Optical micrograph, under brightfield lighting, of a void observed during cross sectioning of a board.

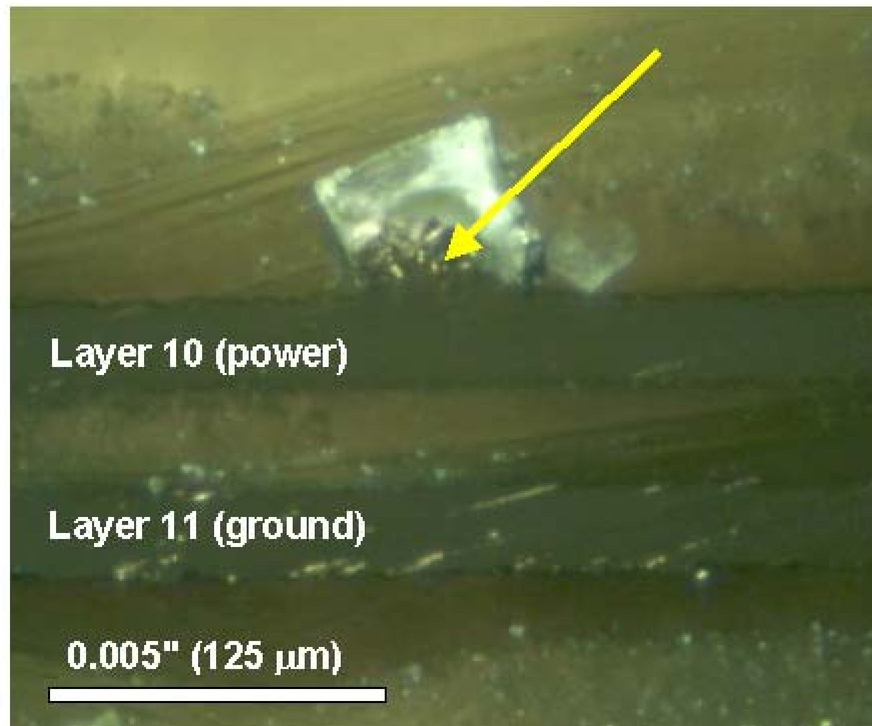

Figure 63. Optical micrograph, using differential interference contrast, of a vertical cross-section of the board. The filler agglomerate has maximum dimension of 3.5 mil (87 microns). A yellow arrow marks what appear to be nodules of copper emanating from layer 10 (power).

Since the spacing between the power and ground plane is only 2 mils (~50.8 microns), particles exceeding this size would bridge layers 10 and 11. However, bridging alone does not explain the electrical failure seen in the printed wiring boards. This is because silica-based particles are electrically insulative. An additional mechanism, known as electrochemical migration (ECM) is required.

A Scanning SQUID Microscope is a sensitive near-field magnetic imaging system. This microscope can image buried current-carrying wires by measuring the magnetic fields produced by the currents, or it can be used to image fields produced by magnetic materials. By mapping the current in an integrated circuit or a package,

short circuits can be localized and designs can be verified to ensure that charge is flowing where expected. MAGMA-C10 uses a high temperature SQUID with a sensitivity of 20 picotesla or two million times smaller than the Earth's magnetic field. The microscope has been designed to keep a high temperature SQUID cooled below 80K and in vacuum while the device under test (DUT) is at room temperature in air. The unique design of MAGMA-C10 also enables the SQUID to be positioned as close as 50 mm from the DUT. Even though the SQUID is not in a magnetically shielded environment, the sensitivity is high enough to image currents as small as 600 nA at a 100 mm working distance with 30 ms averaging.

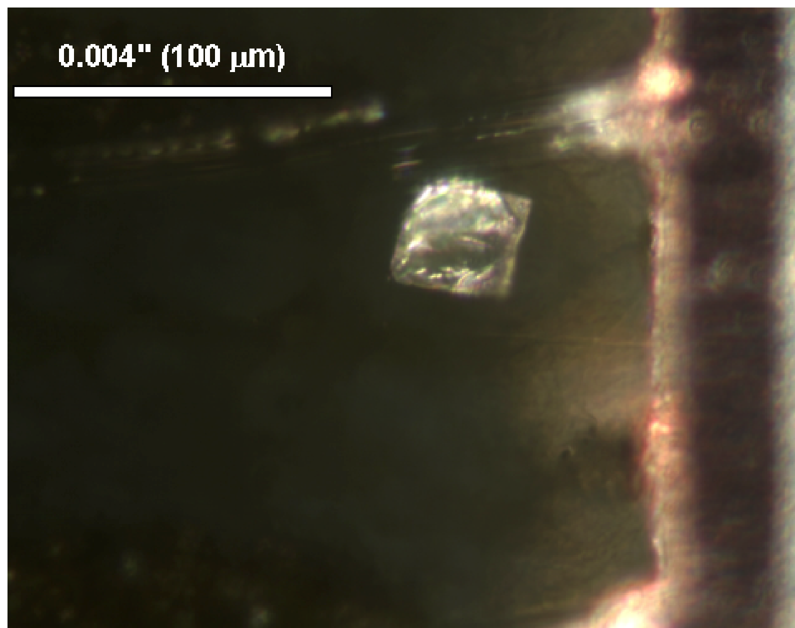

Figure 64. Optical micrograph of a vertical cross-section showing what appears to be a nodule in the PWB.

The magnetic field produced by a sample can be imaged by rastering the sample in close proximity to the SQUID. If the sample contains a permanent magnetic field, as

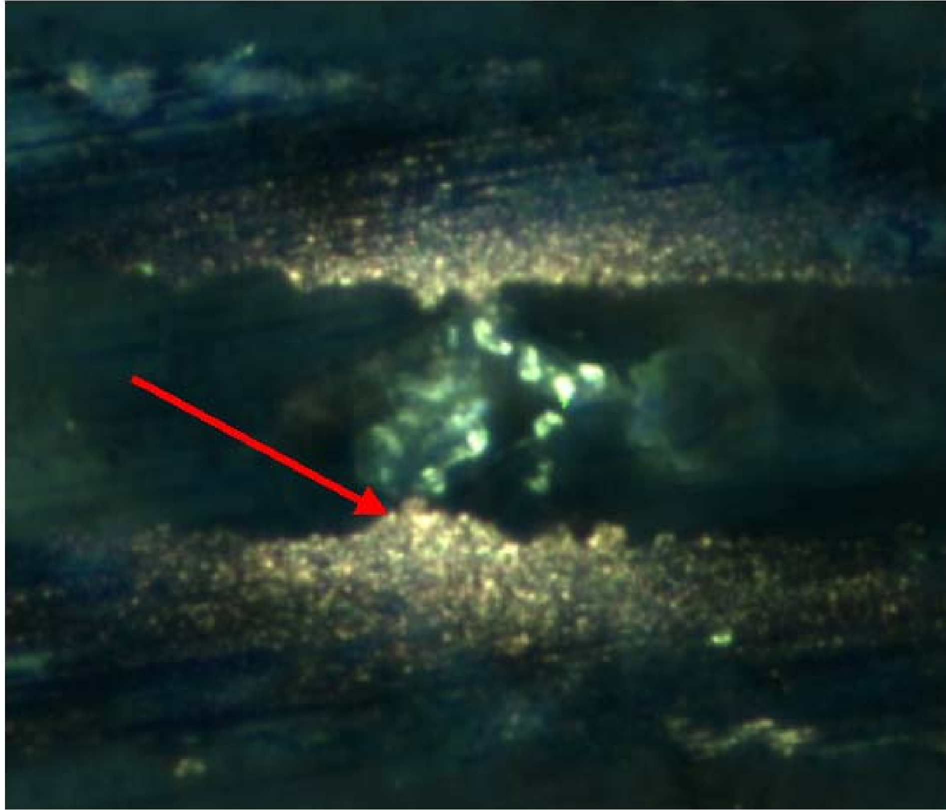

Figure 65. Particle observed in the center of a “mound”

in many land grid arrays and lead frames, the microscope will map out this constant or “DC” magnetic field. In addition, electric currents in the device produce magnetic fields. The presence of a short circuit in an electrical part typically appears as a very strong concentration of magnetic field strength, with the field in opposite directions to either side of the short.

During non-contact imaging of room temperature samples in air, the system achieves a raw, unprocessed spatial resolution equal to the distance separating the sensor from the current, or the effective size of the sensor (~30 microns for a standard SQUID tip), whichever is larger. To best locate a short in a buried layer, however, a Fast Fourier Transform (FFT) back-evolution technique can be used to transform the

magnetic field image into an equivalent map of the current in an integrated circuit or printed wiring board. The resulting current map can then be compared to the circuit diagram to determine the fault location. With this post-processing of a magnetic image and the low noise present in SQUID images, it is possible to enhance the spatial resolution by factors of 5 or more over the near-field limited magnetic image. This enhanced resolution describes how well a scanning SQUID microscope can resolve current paths in a sample. The system's output is displayed as a false-color image of magnetic field strength or current density (after processing) versus position on the sample.

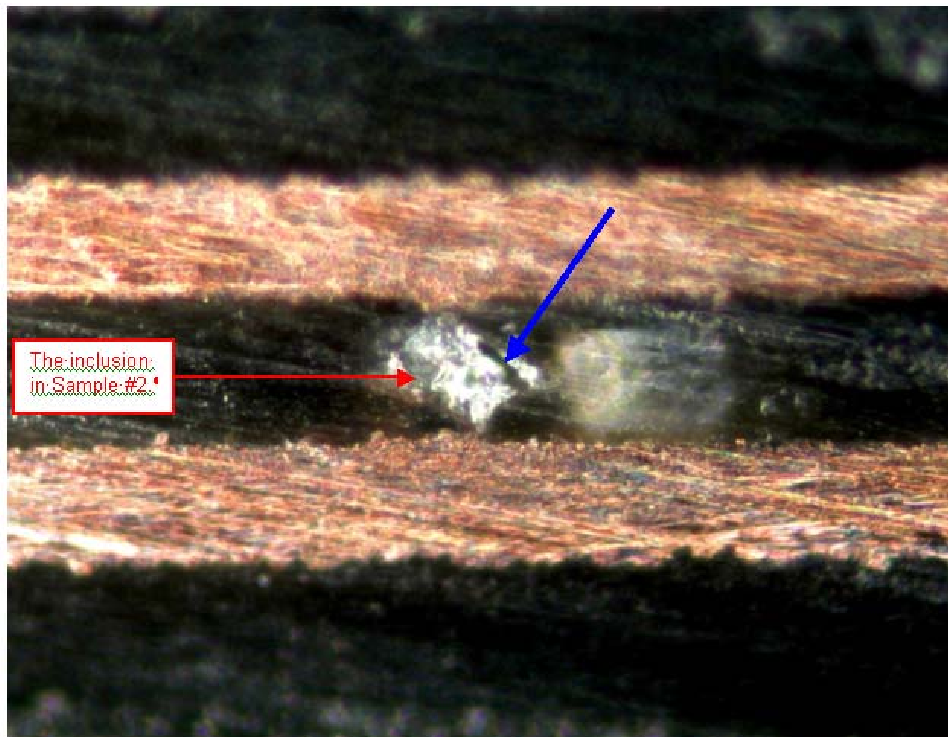

Figure 66. An area containing a particle bridging two copper planes is shown.

7.2 Use of SQUID Microscopy in Detecting VFF

SQUID microscopy was performed on failure sites identified in Figure 65. The results for the 2-mil core are shown in Figure 66. The results demonstrate that current is flowing through the particle, verifying that the identified particle is the location of the short circuit. The results for the 4-mil core are shown in Figure 67. These results demonstrate that the horizontal and vertical location of the short strongly corresponds to the location of the hydrolyzed Cabosil particle.

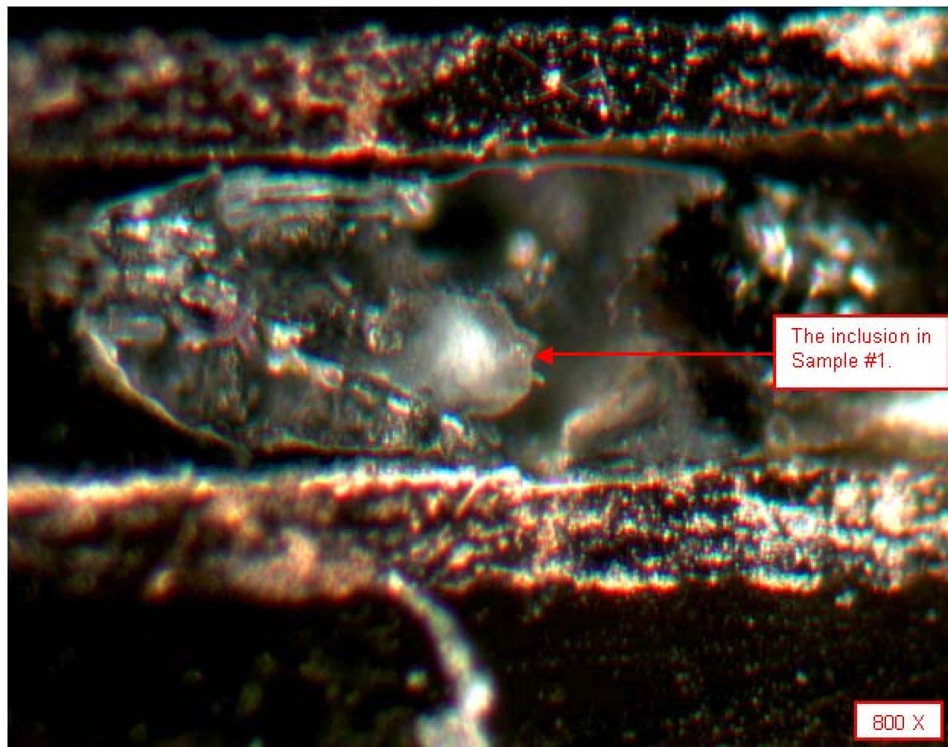

Figure 67. Particle seen in material, bridging two copper planes.

CHAPTER 8: GLASS-SILANE-EPOXY BONDING AND DEBONDING

8.1 Voltage Dependency of Glass-Epoxy Interfacial Adhesion

The previous chapters detailed the results of the experimental investigation on conductive filament formation behavior as a function of applied voltage, conductor geometry, and conductor spacing. Of particular interest from the experimental results was the broad range of failure times among similar coupons tested under the same environmental conditions. Specifically, within one material set at an applied potential of 10 VDC, one coupon failed after approximately 18 minutes while a second coupon experienced no failure after 500 hours of exposure to the same conditions. The large discrepancy initially suggested that within the first coupon was a pre-existing path, potentially due to manufacturing defects, while the second coupon was relatively resistant to path formation. The second coupon did experience relatively rapid failure, within two hours, after the application of 50 VDC. Nominally, this type of extreme change in failure behavior would not be expected, as most of the time-to-failure models within the literature indicate a linear dependence on voltage. Therefore, an increase in the voltage by a factor of 5 should result in the equivalent drop in time to failure. A much more abrupt change in behavior, by approximately two orders of magnitude, seems to suggest that the presence of an electric field may accelerate the process of path formation. The purpose of this section is to provide an analytical discussion of the potential mechanisms by which electric energy would initiate or

accelerate path formation, within the framework of the degradation of the fiber/matrix interfacial bond.

Numerous discussions in prior work on conductive filament formation have repeatedly emphasized that the time required to induce path formation between the glass fiber reinforcement and the epoxy matrix is the rate limiting step in regards to time to product failure [5]. As mentioned in the previous chapters, variants have been identified that allow for the immediate migration of conductive filaments within the laminate structure. These variants included manufacturing defects, such as micro-cracking along the fiber/matrix interface, hollow fibers, and the presence of vertical paths. While the characterization of these path variants is critical to the furthering the knowledge base on conductive filament formation, the primary focus in industrial and scientific investigations has been on the degradation of the fiber glass to epoxy resin bonding, which allows for the creation of a physical path after some latency period.

It has been theorized that this degradation mechanism is the hydrolysis of the organosilanes used as an adhesion promoter on the surface of the glass fiber. While there are numerous definitions of silanes, and more specifically organosilanes, for the purposes of this dissertation they will defined as a bi-functional molecule with the chemical formulae $Y\text{-}(CH_2)_n\text{-}Si(OX)_3$, where Y is an organo-functional group and OX is a silicon-functional group [19]. During glass fiber manufacture, the organosilanes are applied as a component of a surface solution called a size. In the presence of water, the silicon function group hydrolyzes, forming a silanol group,

$Si(OH)_3$, that chemically reacts with the hydroxyl groups on the surface of the glass to form a network of siloxane bonds (Si-O-Si) [20]. A schematic of this process is provided in Figure 68. The organo-functional group then reacts with the epoxy matrix during the curing process, creating a physio-chemical bond.

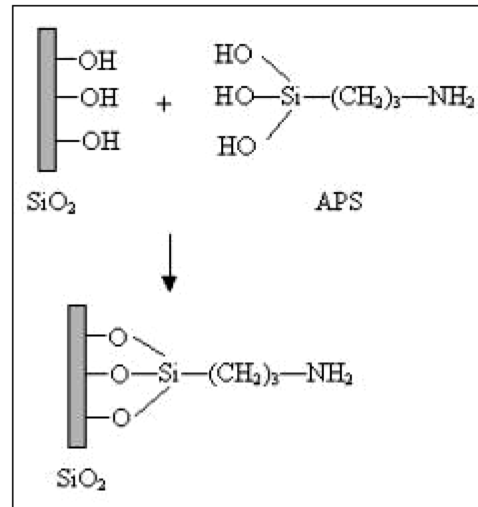

Figure 68. Schematic of reaction between organosilane and glass surface

The degradation reaction of concern, hydrolysis of silane bonds after long-term exposure to elevated temperature/humidity conditions, is simply a reversal of siloxane reaction, as per

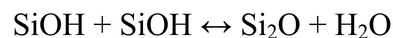

$$SiOH + SiOH \leftrightarrow Si_2O + H_2O$$

The use of this reaction to describe path formation in conductive filament formation is an expected result. Hydro-thermal degradation of silane bonds in glass/epoxy composites is well known [21-25] and provides a basis for the latency period often observed during experimental measurements. As a result, the previous investigations

into conductive filament formation have claimed that path formation due to hydrolysis is the rate-limiting step in product failure.

A number of investigators have also attempted to provide a life model to describe time to failure behavior [7, 9, 10, 14]. These models, detailed in Chapter 2, are primarily empirically-based, and contain a number of environmental parameters, including voltage, distance, temperature and moisture. An interesting contradiction is the presence of voltage within the life models. Within the process of corrosion at the anode, the presence of a voltage is justifiable as the rate of oxidation is directly proportional to electromotive force (EMF). Within the process of metal migration, the presence of an electric field term, voltage normalized by anode-to-cathode separation, can be rationalized by the electric field applying the force that induces the metallic ions to move towards the cathode. However, if, as previously mentioned, path formation is the rate-limiting step, the influence of voltage has not been clearly explained in regards to mechanisms occurring at the molecular-level.

8.2 Chemistry of Glass-Silane-Epoxy Interfacial Bonding

Epoxy/silane/glass bonding occurs in three steps – hydrolysis of the silane, condensation of the hydrolyzed silane on the glass, and coupling of the epoxy to the hydrolyzed silane. The silane is usually of the form $XSiY_3$, where X is an organofunctional group and Y is a hydrolysable functional group. Glycidoxypropyltrimethoxysilane and aminopropyltriethoxysilane are common examples. Both have n = 1 and all four hydrogens replaced by functional groups.

Glycidoxypropyltrimethoxysilane:

```
  CH3 – O
         \
CH3 – O – Si – CH2 – CH2 – CH2 – O – CH2 – CH – CH2
         /                                \    /
  CH3 – O                                   O
```

Aminopropyltriethoxysilane:

```
  CH3 – CH2 – O
               \
CH3 – CH2– O – Si – CH2 – CH2 – CH2 – NH2
               /
  CH3 – CH2 – O
```

Hydrolysis of the silane takes place as follows:

```
  CH3 – O
         \
CH3 – O – Si – CH2 – CH2 – CH2 – O – CH2 – CH – CH2  + 3 HOH
         /                                \    /
  CH3 – O                                   O          water

                         ↓↑

  HO
    \
HO – Si – CH2 – CH2 – CH2 – O – CH2 – CH – CH2  + 3 H3OH
    /                                \    /
  HO                                   O          methanol
```

OR

```
  CH3 – CH2 – O
               \
CH3 – CH2– O – Si – CH2 – CH2 – CH2 – NH2  + 3 HOH
               /
  CH3 – CH2 – O                             water

                         ↓↑

  HO
    \
HO – Si – CH2 – CH2 – CH2 – NH2  + 3 CH3 – CH2 –OH
    /
  HO                                  ethanol
```

To understand the condensation of the hydrolyzed silane on the glass, it must be understood that in silica, each silicon atom is covalently bonded to four oxygen atoms, each of which is covalently bonded to another silicon atom. Thus, each oxygen atom is shared between two silicon atoms, contributing ½ of an oxygen atom to each silicon atom. Four ½ atoms of oxygen per silicon are the same as two atoms of oxygen per silicon, giving silica the formula SiO_2. At the surface, however, there is one oxygen per silicon atom that is not bonded to any other atom – a dangling bond, as shown below in Figure 69.

.

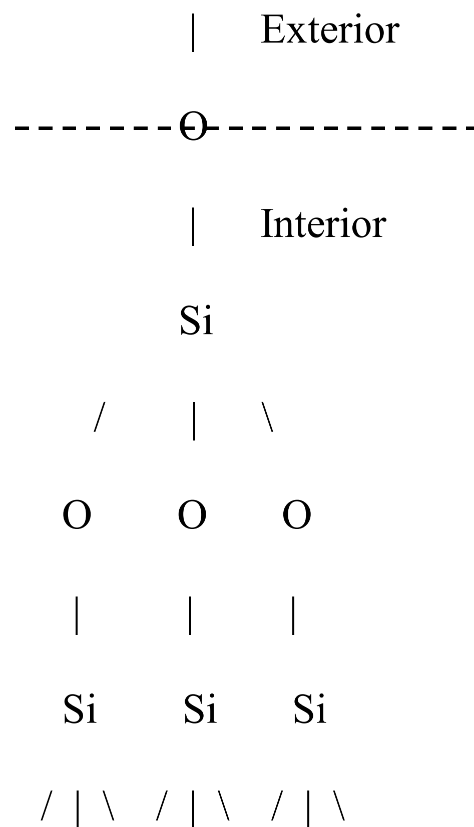

Figure 69. Schematic showing each dangling bond attached to a hydrogen atom.

A similar phenomenon occurs for the other constituents of the glass at the surface, resulting in a surface consisting of hydroxyl groups. The condensation of the hydrolyzed silane on the glass occurs as follows:

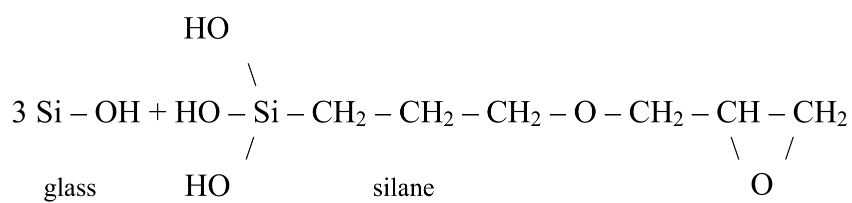

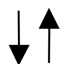

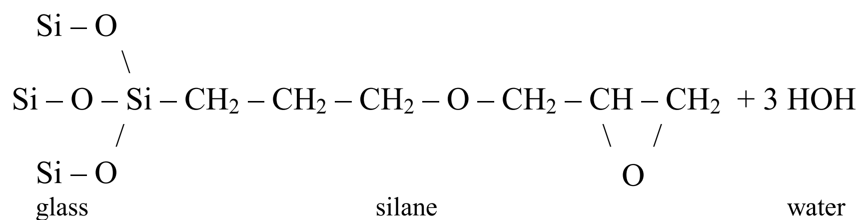

OR

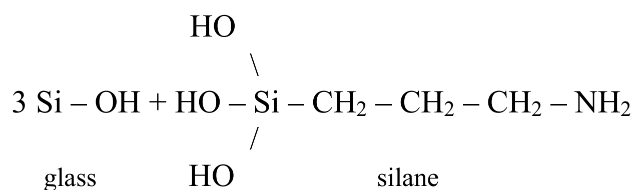

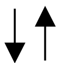

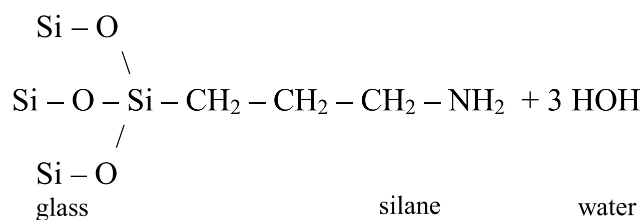

Note that the silicon atom in the silane is now bonded to the silicon atoms in the glass through oxygen atoms – as the silicon atoms in the glass are bonded to each other. If the water produced in the forward reaction is continuously removed, by evaporation for instance, the bonding of silane to glass will continue until either there is no more silane or no more attachment sites on the glass surface. Conversely, if water is added

to silane bonded to glass, the reverse reaction can be driven, debonding the silane from the glass. Assuming that the coupling of the epoxy to the hydrolyzed silane takes place at the same site as curing and that it involves the epoxide and hydroxyl groups, the reaction should proceed as follows:

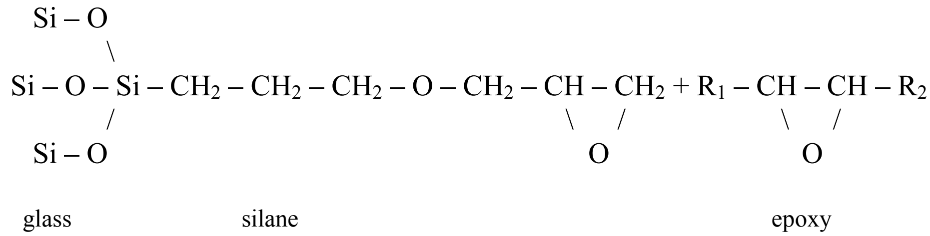

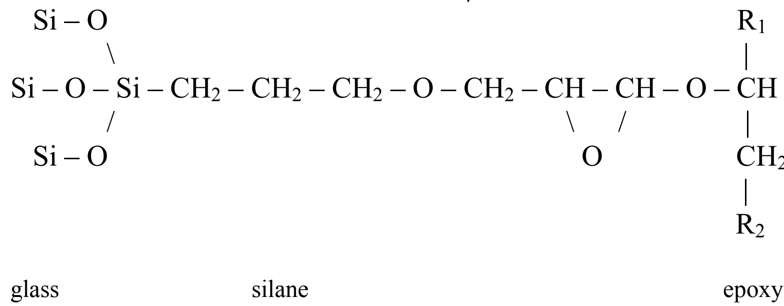

OR

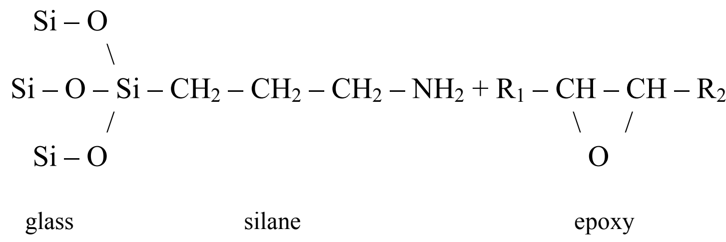

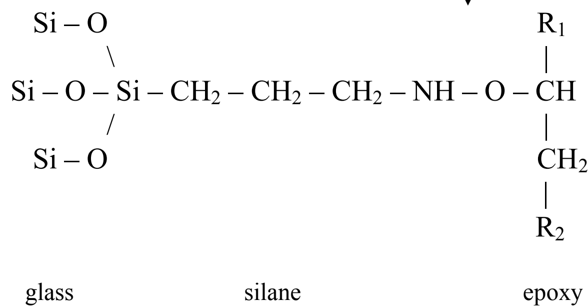

There is a single reaction product – no water is produced – so the water that drives the debonding of the silane from the glass would not reverse this reaction, debonding the silane from the epoxy. For the rate of debonding of the silane from the glass, let

K = the reaction rate constant
k = Boltzmann's constant
h = Planck's constant
C_B = the interfacial bond concentration
C_W = the attacking chemical (water) concentration
f_B = the interfacial bond activity coefficient
f_W = the attacking chemical activity coefficient
P = the pressure of the reaction environment (1 atmosphere)
T = the absolute temperature of the reaction environment
ΔV = the change in volume between reactants and products
ΔG^*_0 = the change in Gibbs free energy between reactants and products

Then, per Leung, S.Y.Y., Lam, D.C.C., and Wong, C.P.[29],

$$K = (kT/h)\,(C_W f_W) \exp - [(\Delta G^*_0 - P\,\Delta V) / kT] \qquad (20)$$

and $$d\,C_B / d\,t = - K\,C_W f_W C_B f_B \qquad (21)$$

Let C_{B0} = the initial interfacial bond concentration

Then, integrating equation 21 to obtain the interfacial bond concentration as a function of time:

$$\int_{C_{B0}}^{C_B} d\,C_B / C_B = - \int_0^t K\,C_W f_W C_B f_B\,d\,t = - K\,C_W f_W C_B f_B \int_0^t d\,t$$

$$\ln C_B - \ln C_{B0} = - K\,C_W f_W C_B f_B\,(t - 0)$$

$$\ln (C_B / C_{B0}) = - K\,C_W f_W C_B f_B\,t$$

$$C_B / C_{B0} = \exp [- K\,C_W f_W C_B f_B\,t]$$

$$C_B / C_{B0} = \exp - (kT/h)\,(C_W f_W)^2\,(C_B f_B)\,t\,\{\exp - [(\Delta G^*_0 - P\,\Delta V) / kT]\} \qquad (22)$$

Thus the interfacial bond concentration as a function of time is an exponential function of the change in Gibbs free energy between reactants and products. Hence, the Gibbs free energy is a function of the electrochemical potential, which is made up

of the chemical potential and the electrical energy (i.e. the electromotive force, also known as "voltage") and is a measure of the potential for matter flux.

Also, the higher the applied voltage, the greater will be the separation of H^+ and OH^- ions coming from the adsorbed water.

- The negative ions will be attracted to the positive anode
- The positive ions will be repelled into the pre-existing crack/flaw, decreasing the local pH, or acidity

Prior studies have shown that the rate of hydrolytic degradation is accelerated in acidic environments. Hence, it appears that increasing the applied voltage increases the chemical reaction rate of the debonding at the fiber to resin interface, allowing a path for subsequent filament growth.

CHAPTER 9: OBSERVATIONS AND CONTRIBUTIONS

9.1 Observations

When the DC voltage bias is removed shortly after a failure is detected, the short can disappear, even if the samples are kept in the high temperature/high humidity environment (85 C, 85% RH), especially for the PTH-plane failures. This suggests that the copper ions may be still mobile in the initial stages of failure and still need voltage bias as a driving force to maintain the location of the copper ions.

For PWB conductor spacings 4 mils or less, the IPC TM-650 CAF test may not be suitable, as there were instantaneous failures in the samples with conductor spacings 4 mils and less. These failures were not due to CFF as shown by the SQUID.

Extensive optical and E-SEM microscopic examinations of cross-sectioned areas, in close proximity to and far away from the failure sites, revealed that there was degradation only in the vicinity of the failure.

Comparison of the time to failure for the different spacings shows that boards, which survive the longest at the larger spacings, may not necessarily survive the longest for closer spacings. At closer spacings, defects such as wicking and damage due to drilling have a greater impact, whereas for the larger spacings, interfacial-bonding strength may be the controlling parameter.
Examination of the PTH-PTH dielectric breakdown voltage values after exposure of the test boards to 85 C, 85% RH for 96 hours shows that the trend follows the time to

failure observed for the PTH-PTH failure data, NY 170>NY 150> IS FR408 and IS FR406. This suggests that dielectric breakdown voltage could be an indicator of CFF susceptibility.

Board types that show the longest time to failure due to CFF in PTH-PTH configuration, may not necessarily offer the best protection for PTH-plane geometry. PTH-PTH CFF resistance experimentally found was NY 170>NY 150> IS FR408 and IS FR406, but PTH-plane CFF resistance was IS FR408> NY 170 and NY 150> IS FR408.

Industry uses one of three failure criteria to determine a failure definition:

- Hard short (1 x 10^6 ohms, permanent)
- Decade drop in resistance (TM-650, 2.6.25)
- Less than 100 Megaohms (IPC/EIA J-STD-001C)

As seen in the time to failure data for the samples tested, the failure criteria selected can have a significant impact on the time to failure, as per the definition.

The IPC-TM-650 test specification of monitoring every 24 – 100 hours may allow intermittent failures to go undetected, as seen in the cases where intermittent drops in insulation resistance may last only 5 – 6 minutes and then fully recover.

9.2 Contributions

1. Identified a failure involving a hollow fiber, filled with copper colored material bridging and shorting two PTHs, verifying that hollow fibers can lead to CFF failures

2. Applied a hollow fiber detection technique used in detecting leaks in pressure vessels and modified it to allows the detection of hollow fibers within printed wiring boards

3. Developed a failure probability equation based on hollow fiber concentration, which allows the calculation of a critical hollow fiber concentration for an acceptable reliability, based on board and conductor parameters

4. Developed a hollow fiber assessment standard screen, allowing board fabrications and contract assemblers to qualify suppliers and discard lots with hollow fiber concentrations above acceptable specifications
5. Discovered a new type of "vertical" filament formation, migrating in different, vertical path through cabosil, rather than along the traditional horizontal fiber-epoxy delaminated interface
6. Demonstrated the use of the scanning superconducting quantum interference device (SQUID) in detecting and locating short circuit paths due to CFF by analyzing the failures in the test boards in this study.
7. Experimentally demonstrated that the specification on monitoring insulation resistance (24 – 100 hours) used in the current industry standard IPC-TM-650- is insufficient for capturing intermittent failure occurrences, as seen in some of the intermittent failures lasting for durations of less than 6 minutes

8. Showed that the IPC industry standard for CFF testing of PTH-PTH conductor spacings of 4 mils or less, at 85°C/85% RH can introduce a failure mechanism other than CFF

CHAPTER 10: SUMMARY

The electronics industry has recognized that failure due to conductive filament formation in printed circuit boards is a problem. To address this issue, organizations such as the National Physical Laboratory spend up to 3 million dollars annually to characterize these failures. IPC has also developed testing standards to evaluate a printed wiring board's susceptibility to conductive filament formation failures. Board fabricators, in an attempt to mitigate the risks of printed wiring failures due to this phenomenon have fabricated "CFF resistant laminates".

Previous researchers (discussed in Chapter 2) have developed time to failure models, which are empirically derived, rather than based on physics of failure. There is also a voltage term in each of these equations. The time to failure due to conductive filament formation, is divided in two sequential steps:

t_1 – the time for path formation, and

t_2 – the time for the electrochemical reaction or filament growth, where $t_1 >> t_2$

Since the rate-limiting step (t_1) the time for the path formation is much longer than t_2, the time for the conductive filament growth ($t_1 >> t_2$), t_2 may be negligible. Lando in 1979 postulated that the formation of the path (t_1) was independent of voltage. However, the time to failure models, all contain a voltage parameter, and basically predict the time for the rate-limiting step (reported by Lando to be voltage

independent). There is a contradiction since this rate-limiting step is voltage independent.

In this dissertation, it was shown that voltage, but more so the electric field (a combination of voltage and conductor spacing), plays a role in the rate at which the path is formed due to a relationship to the Gibbs free energy, and the polar nature of the water molecule.

To give more insight into the overall understanding of this failure mechanism, specifically in how the rate-limiting step - the formation of a path – is created, different variations of path formation were investigated.

Optical and electron microscopic examinations of failure sites due to conductive filament formation show that the formed path is typically along debonded or delaminated fiber glass/epoxy resin interfaces, due to breaking of the silane bonds. The silane bonds can be chemically degraded by hydrolysis (adsorption of water at the fiber glass/epoxy resin interface) or by repeated thermal cycling, which induces stresses at the interface due to a CTE ration mismatch of 1 to 12 (5 ppm/^{o}C – E fiber glass, 60 ppm/^{o}C – FR-4 epoxy resin). The formation of these types of paths take some finite amount of time, since the moisture absorption or thermal cycling is necessary for the eventual breaking/degradation of the bonds at the interface, allowing a path between conductors. However, two new variants of path formation were discovered and examined. These new variations are:

1. Formation through hollow fibers (discussed in Chapter 4) and,
2. Vertical formation through cracked silica particles (Chapter 7)

With these two new variants, t_1 – the time for path formation and rate limiting step, is zero, as the path is already present prior to operation or testing of the printed wiring assembly. Hence, the time to failure is only t_2 – the time for the electrochemical reaction or filament growth, where $t_1 >> t_2$, and can be orders of magnitude shorter since there is a pre-existing path. For products which may be used in harsh environments (high temperature and humidity) such as avionics, automotive, military and medical, where reliability is critical, there should be screens/acceptance criteria in place to ensure that these manufacturing related defects which can significantly shorten the time to failure due to CFF and put lives in jeopardy. A methodology to detect and screen hollow fibers was developed and an example of how it can be implemented based on an acceptable level of reliability is given in Chapter 4.

The accelerated tests in this study were conducted using boards designed with the smallest conductor spacings ever tested (as small as 2 mils distances between oppositely biased conductors). Subjecting the boards to tests as prescribed by the IPC standard for CFF testing showed that other failure mechanisms can be introduced as well as failures due to CFF being missed by the monitoring frequency specification of every 24 to 100 hours. Due to the intermittent nature of CFF failures, (some in this study lasted for only 5 minutes), unless there is continuous monitoring of the resistance between conductors of interest, some failures may fall through the cracks,

especially those of short durations. Hence, another test method to address the continuously shrinking feature sizes that will eventually reach 2 mils, and correctly assess a laminate's robustness to CFF failures needs to be developed.

These tests also showed that for the FR-4 type of laminates and feature sizes used, there could be failures in less than 40 hours in conditions as harsh as 85 ^{o}C/85% RH as seen by the insulation resistance monitoring of the 4 and 3 mil spacings. Other materials or designs will have to be incorporated as feature sizes shrink while the use in and exposure to harsh environments (such as lead free reflow profiles) increase.

An observation from a set of tests shows that dielectric voltage breakdown values may be an indicator of the resistance of a laminate to CFF failure. This has the potential to save time and money due to the expensive equipment needed for the monitoring setup and the length of time (500 hours or ~ 3 weeks) required for the testing.

CHAPTER 11: FUTURE WORK

It has been shown that increasing the voltage can increase the rate of path formation. Subsequent CFF investigations, which focus on the characterization of hydrolytic degradation of silanes under a range of applied voltages and electric fields, should be completed. The results of these tests can give information on the relationship between voltage and path formation.

Tests show that there may be a relationship between dielectric breakdown and time to failure due to CFF. A follow up study consisting of a broad range of testing should be performed to assess how predictable is the relationship between dielectric breakdown and susceptibility to CFF. A design of experiments should also be carried out to determine and optimize the duration of time and humidity/temperature parameter settings necessary to initiate path degradation so that dielectric breakdown can occur along the "weakened" path, simulating CFF.

Tests using the same boards should be run at other temperature and relative humidity environments to determine and validate the acceleration factors and determine which accelerated test environments may be applicable for feature spacings less than 4 mils to induce CFF failures.

Some tests have indicated that time to failure is dependent on the direction of the fabric weave along which the path is formed. Accelerated tests should be run along different orientations of the fiber weave to evaluate the increase or decrease in time to

failure that can be expected for conductors which are parallel, perpendicular, and at 45 degree angles to the machine weave of the fabric.

REFERENCES

1. Boddy, P.J., Delany, R.H., Lahti, J.N., Landry, E.F. and Restrick, R.C. "Accelerated Life Testing of Flexible Printed Circuits," *14th International Reliability Physics Symposium*, 1976, pp. 108-116.
2. *Electrochemical Migration: Electrically Induced Failures in Printed Wiring Assemblies,* IPC-TR-476A, The Institute for Interconnecting and Packaging Electronic Circuits, Northbrook, IL, IPC 1997.
3. Kohman, G.T., Hermance, H.W. and Downes, G.H. "Silver Migration in Electrical Insulation," *The Bell Technical Journal*, Nov. 1955, p. 1115.
4. Lathi, J.N., Delaney, R.H. and Hines, J.N. "The Characteristic Wear-out Process in Epoxy Glass Printed Circuits for High Density Electronic Packaging," *Reliability Physics, 17th Annual Proceeding*, 1979, pp. 39–43.
5. Lando, D.J., Mitchell, J.P. and Welsher, T.L. "Conductive Anodic Filaments in Reinforced Polymeric Dielectrics: Formation and Prevention," *Reliability Physics, 17th Annual Proceeding*, 1979, pp 51–63.
6. Welsher, T.L., Mitchell, J.P. and Lando, D.J. "CAF in Composite Printed-Circuit Substrates: Characterization, Modeling, and a Resistant Material," *Reliability Physics, 18th Annual Proceeding*, 1980, pp 235–237.
7. Mitchell, J.P. and Welsher, T.L. "Conductive Anodic Filament Growth in Printed Circuit Materials," *Proceedings of the Printed Circuit World Convention II,* 1981, pp. 80-93.

8. Augis, J.A., DeNure, D.G., LuValle, M.J., Mitchell, J.P., Pinnel, M.R. and Welsher, T.L. "A Humidity Threshold for Conductive Anodic Filaments in Epoxy Glass Printed Wiring Boards", *3rd International SAMPE Electronics Conference*, 1989, pp. 1023-1030.
9. Rudra, B.S. and Pecht, M.G. "Assessing Time-to-Failure Due to Conductive Filament Formation in Multi-Layer Organic Laminates," *Packaging and Manufacturing Techniques,* Part B, Vol. 17, No. 3, 1994, pp. 269-276.
10. Sauter, K. "Electrochemical Migration Testing Results: Evaluating PWB Design, Manufacturing Process, and Laminate Material Impacts on CAF Resistance, *CircuiTree*, July, 2002.
11. Ready, W.J., Turbini, L.J., Stock, S.R. and Smith, B.A. "Conductive Anodic Filament Enhancement in the Presence of a Polyglycol-Containing Flux," *1996 IEEE International Reliability Physics Proceedings,* 1996, pp. 267-273.
12. Turbini, L.J., Bent, W.R., and Ready, W.J. "Impact of Higher Melting Lead-Free Solders on the Reliability of Printed Wiring Assemblies," *Journal of Surface Mount Technology*, October 2000, pp. 10-14.
13. Brewin, A., Zou, L. and Hunt, C. "Susceptibility of Glass-Reinforced Epoxy Laminates to Conductive Anodic Filamentation," Materials Centre, National Physical Laboratory, Teddington, Middlesex, January 2004.
14. Li, M.J., Pecht, M.G. and Wang, L. "The Physics of Conductive Filament Formation in MCM-L Substrates," *Proceedings of the INTERpack'95, Lahaina, Maui, HI,* March 26-30, 1995, pp. 517-527.

15. Li, M., Gohari, K. and Pecht, M. “Effect of Temperature and Humidity Cycling on FR-4, Bismaleide Triazine and Cyanate Ester Printed Wiring Boards,” *7th International SAMPE Electronics Conference - Critical Materials Processing in a Changing World*, June 20-23, 1994, pp. 446-457.
16. Domeier, L., Davignon, J. and Newton, T. “A Survey of Moisture Absorption and Defects in PWB Materials,” Proceedings of the 1993 Fall IPC Meeting (1993), pp. 3-5.
17. William, V., et al. “Conductive Anodic Filament Resistant Resins,” *Proceedings of the IPC Printed Circuits Expo*, March 2002.
18. “Conductive Anodic Filament (CAF) Resistant Test: X-Y Axis” IPC-TM-650 2.6.25, The Institute for Interconnecting and Packaging Electronic Circuits, Northbrook, IL, IPC, 2003.
19. Mack, H. “Choosing the Right Silane Adhesion Promoters for SMP Sealants,” Adhesive and Sealant Council Meeting, Orlando, Fl, Spring 2001.
20. Kim, J.K. and Hodzic, A. “Nanoscale Characterisation of Thickness and Properties of Interphase in Polymer Matrix Composites,” *Journal of Adhesion*, Vol. 79, pp. 383-414, 2003
21. Ishida, H. and Koenig, J.L. “Effect of Hydrolysis and Drying on the Siloxane Bonds of a Silane Coupling Agent Deposited on E-glass Fibers,” *Journal of Polymer Science*, Polymer Physics Edition, vol.18, no.2, Feb. 1980. p. 233-7
22. Ishida, H. and Koenig, J.L. “A Fourier-transform Infrared Spectroscopic Study of the Hydrolytic Stability of Silane Coupling Agents on E-glass Fibres,” *Journal of Polymer Science*, Polymer Physics Edition, vol.18, no.9, Sept. 1980. p. 1931-3

23. Salmon, F. T., Paysb, M. F. and Verdu, J. "Hydrolytic Degradation of Model Networks Simulation the Interfacial Layers in Silane Coupled Epoxy/Glass Composites," Composites Science and Technology, vol. 57, pp. 1119-1127, 1997
24. Gurumurthy, C. K., Kramer, E.J. and Hui, C.Y. "Hydro-Thermal Fatigue of Polymer Interfaces," Acta Mater, vol. 49, pp. 3309-3320, 2001
25. Ritter, J. E. and Huseinovic, A. "Adhesion and Reliability of Epoxy/Glass Interfaces," *Journal of Electronic Packaging*, vol 123, pp. 401-403, December 2001
26. Corning Museum of Glass, "A Resource for Glass," www.cmog.org/usr/media/aroglass.pdf, compilation date not provided, retrieval date October 9, 2004.
27. Callen, H.B.; Thermodynamics, An Introduction to the Physical Theories of Equilibrium Thermostatics and Irreversible Thermodynamics; John Wiley & Sons; New York, NY; 1960; pp. 32, 45-46.
28. Harper, C.A., & Sampson, R.N. (eds); Electronic Materials and Processes Handbook, Second Edition; McGraw-Hill, Inc.; New York; NY; 1994; p. 1.38.
29. Leung, S.Y.Y., Lam, D.C.C. and Wong, C.P. "Experimental Investigation of Time Dependent Degradation of Coupling Agent Bonded Interfaces:' *IEEE Electronic Components and Technology Conference*; 2001.
30. Caso, G.B., Schwabel, M.G. and Frechette, V.D. "Effects of Electrical Fields on Slow Crack Growth in Glass," *Journal of the American Ceramics Society*, Vol. 73, No. 1, 1990, pp.43-48.

31. Walker, J.S. Physics, Prentice Hall, Upper Saddle River, New Jersey, 2002, p. 666, Table 20-2.

32. "Qualification and Performance of Permanent Solder Mask" IPC-SM-840C, The Institute for Interconnecting and Packaging Electronic Circuits, Northbrook, IL, IPC, January 1996.

33. Shukla, A., Pecht M., Jordan J., Rogers K. and Jennings D., "Hollow Fibers in PCB, MCM-L and PBGA Laminates May Induce Reliability Degradation", Circuit World, Vol. 23, No. 2, pp. 5-6, 1997.

34. Pecht M., Rogers K. and Fowler A. "Characterization of a Non-woven Randomly Dispersed Short Fiber Laminate", Circuit World, 24/3, pp. 34-37, 1998.

35. Rogers K., Driessche P. V. D., Hillman C. and Pecht M. "Do You Know That Your Laminates May Contain Hollow Fibers", Printed Circuit Fabrication, Vol. 22. No. 4, April 1999.

36. Rogers, K., Hillman C., Pecht, M. and Nachbor, S. "Conductive Filament Formation Failure in a Printed Circuit Board", Circuit World, Vol. 25, No. 3, 1999.

37. Pecht, M., Hillman, C., Rogers, K. and Jennings, D. "Conductive Filament Formation: A Potential Reliability Issue in Laminated Printed Circuit Cards with Hollow Fibers", *IEEE/CPMT*, Vol. 22. No. 1, pp. 60-67, January 1999.

38. Pecht, M., Rogers, K. and Hillman, C. "Hollow Fibers can Accelerate Conductive Filament Formation", ASM International Practical Failure Analysis, pp. 57-60, Volume1, Issue 4, August 2001.

39. Hillman C. and Rogers K. “A Novel Approach to Identifying and Validating Electrical Leakage in Printed Circuit Boards through Magnetic Current Imaging", 30th International Symposium for Testing and Failure Analysis, November 16-17, 2004 Worcester, MA

40. Katayanagi, H., Tanaka, H., Aoki, Y. and Yamamoto, S. “The Effects of Adsorbed Water on Printed Circuit Boards and the Process of Ionic Migration”, ESPEC Technology Report No. 9

41. Meeker, W. and LuValle, M. “An Accelerated Life Test Model Based on Reliability Kinetics”, Technometrics, Vol. 37, No. 2, May 1995, pp 133-146.

42. Steppan, J., Roth, J., Hall, L., Jeanotte, D. and Carbone, S. “A Review of Corrosion Failure Mechanisms during Accelerated Testing”, *Journal of Electrochemistry, Society of Solid State Science and Technology*, Vol. 134, No. 1, January 1987, pp175-190.

43. Bergum, E. “CAF Resistance of Non-dicy FR-4”, PC FAB, September 2002, pp 26-30.

44. Ready, W.J. and Turbini, L.J. “The Effect of Flux Chemistry, Applied Voltage, Conductor Spacing and Temperature on Conductive Anodic Filament Formation”, Journal of Electronic Materials, Vol. 31, No. 11, 2003, pp 1208-24.

45. Turbini, L.J., Jachim, J.A., Freeman, G.B. and Lane, J.F. “Characterizing Water Soluble Fluxes: Surface Insulation Resistance vs Electrochemical Migration”, *IEEE/CHMT International Electronics Manufacturing Technology Symposium*, 1992, pp 80-84.

46. Watt, W. and Perov, B. Strong Fibers, North Holland-Amsterdam, New York Oxford, 1985.

47. Amla, T. "Conductive Anodic Filament Growth Failure", PC FAB, July, 2002, pp. 40-43.

48. Tullmin, M. and Roberge, P. "Tutorial: Corrosion of Metallic Materials", *IEEE Transactions on Reliability*, Vol. 44, No. 2, June 1995, pp. 271-78.

49. Wu, B., Pecht, M. and Jennings, D. "Conductive Filament Formation in Printed Wiring Boards", *IEEE/CHMT International Electronics Manufacturing Technology Symposium* 1992, pp 74-79.

50. Detoma, R. "Analysis and Resolution of Copper Migration", PC FAB, December 1984, pp.70-77.

51. Rudra, B., Li, M., Pecht, M. and Jennings, D. "Electrochemical Migration in Multichip Modules", Circuit World, Vol. 22, No. 1, 1995. pp. 67-70.

52. Harsanyi, G. "Electrochemical Processes Resulting in Migrated Short Failures in Microcircuits", *IEEE Transactions on Components, Packaging and Manufacturing Technology*, Part A, Vol. 18, No. 3, September, 1995, pp. 602-10.

53. Hines J.N. "Measurement of Land to Plated Through Hole Interface Resistance in Multilayer Boards," *14th International Reliability Physics Symposium*, 1976, pp. 132-34.

54. Rudra, B. and Jennings, D. "Tutorial: Failure-Mechanism Models for Conductive Filament Formation", IEEE Transactions on Reliability, Vol. 43, No. 3, September, 1994, pp. 354-360.

55. Ready, W.J., Stock, S.R., Freeman, G.B., Dollar, L.L. and Turbini, L.J. "Microstructure of Conductive Anodic Filaments Formed during Accelerated Testing of Printed Wiring Boards", Circuit World, Vol. 21, No. 4, 1995, pp. 5-9.

56. Pecht, M., Haleh, A., Shukla, A., Hagge, J. and Jennings, D. "Moisture Ingress into Organic Laminates", *IEEE Transactions on Components and Packaging Technology*, Vol. 22, No. 1, March 1999, pp. 104-10.

57. Ehrler, S. "A Review of Epoxy Materials and Reinforcements, Part 1", PC FAB, April 2002, pp. 32-38.

58. Kent, M.S. et al., "A Study of Adhesion at the E-Glass/FR-4 Interface", *27th International SAMPE Technical Conference*, October 9th -12th, 1995, pp. 84-89.

59. Ritter, J. and Huseinovic, A. "Adhesion and Reliability of Epoxy/Glass Interfaces", Journal of Electronic Packaging Transactions of the ASME, Vol. 123, December 2001, pp. 401-404.

60. Ritter, J. et al. "Fatigue and Durability of Silane Bonded Epoxy/Glass Interfaces", Mater. Res. Soc. Symp. Proc. 563, pp. 291-295.